Variable Speed and Torque Control of a Wind Turbine System with Assisted Reluctance Synchronous Generator Technology

by

Christoffel Daniel Botha

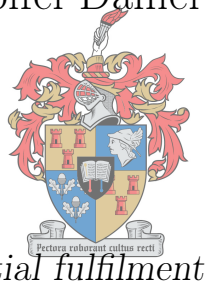

Thesis presented in partial fulfilment of the requirements for the degree of Master of Engineering (Electrical and Electronic) in the Faculty of Engineering at Stellenbosch University

Supervisor: Prof. Maarten J. Kamper

March 2018

Declaration

By submitting this thesis electronically, I declare that the entirety of the work contained therein is my own, original work, that I am the sole author thereof (save to the extent explicitly otherwise stated), that reproduction and publication thereof by Stellenbosch University will not infringe any third party rights and that I have not previously in its entirety or in part submitted it for obtaining any qualification.

Date: March 2018

Abstract

Small-scale wind turbines provide a viable alternative energy source for small farms, business and rural areas. The goal of such small-scale turbines is to provide electricity at the lowest cost possible. It is thus imperative that turbines capture the maximum volume of energy at the lowest cost and highest possible efficiency, while having a high reliability. Assuming a suitable turbine location and good blade design, two of the biggest factors in ensuring this goal include the choice of generators as well as the control of the turbine system. While the permanent magnet synchronous generator (PMSG) is a popular choice for small-scale wind turbines, its use of permanent magnet material increases the cost of the system. One of the alternatives to the PMSG that has received renewed interest during the last few years is the reluctance synchronous generator. This thesis focuses on the development and control of an assisted reluctance synchronous generator (ARSG) wind turbine system. The ARSG is an effort to help solve, at least partially, some of the disadvantages of the standard reluctance synchronous generator (RSG), e.g. the low power factor. A simple rotor design is proposed, with a cursory comparison given between different rotor slot shapes. The mathematical model of the ARSG is derived, which serves as the basis of the development and implementation of a non-linear current controller. A maximum torque per ampere (MTPA) strategy based on the finite element (FE) analysis of the machine is developed and implemented practically. To ensure that the turbine is operated at optimal efficiency, a standard tip speed ratio (TSR) controller is designed and implemented. This controller can operate at under and above rated wind speeds. The results of the practical tests show the feasibility of the use of the DC-bus link connection as well as the performance of the control systems.

Opsomming

Kleinskaalse windturbines bied 'n lewensvatbare alternatiewe energiebron vir plase, besighede en landelike gebiede. Die doel van sulke turbines is om elektrisiteit teen so goedkoop as moontlik te voorsien. Dit is dus noodsaaklik dat die turbine 'n maksimum hoeveelheid energie omskakel teen die laagste koste en die hoogste doeltreffendheid moontlik, en met 'n hoë betroubaarheid. Veronderstel 'n geskikte plek is gekies en die turbine het 'n goeie lem ontwerp, is twee van die grootste faktore die keuse van generator sowel as die beheer van die turbine sisteem. Terwyl die permanente magneet sinchroon generator (PMSG) 'n gewilde keuse vir kleinskaalse windturbines is, verhoog hul gebruik van permanente magneet materiaal die koste van die stelsel. Een van die alternatiewe vir die PMSG wat die afgelope paar jaar hernieude belangstelling ontvang het, is die reluktansie sinchroonmasjien. Hierdie tesis fokus op die ontwikkeling en beheer van 'n windturbine sisteem wat gebruik maak van ondersteunde reluktansie sinchroonmasjien tegnologie (ARSG). Die ARSG is 'n poging om, ten minste gedeeltelik, sommige van die nadele van die standaard reluktansie masjien op te los, bv. die lae arbeidsfaktor. 'n Eenvoudige rotorontwerp word voorgestel, met 'n vlugtige vergelyking wat tussen verskillende rotor-gleufvorme gegee word. Die wiskundige model van die ARSG is afgelei, wat as die basis van die ontwikkeling en implementering van 'n nie-lineêre stroombeheerder dien. 'n Maksimum draaimoment per ampere (MTPA) strategie gebaseer op die eindige element (FE) analise van die masjien word prakties ontwikkel en geïmplementeer. Om te verseker dat die turbine teen optimale doeltreffendheid bedryf word, word 'n standaard spoedverhouding (TSR) beheerder ontwerp en geïmplementeer. Hierdie beheerders kan werk gedurende onder en bo nominale windsnelhede.

Acknowledgements

I would like to express my sincere gratitude to the following people and organisations:

- Professor Maarten Kamper, for his guidance and support throughout the last two years.
- Mr Petro Petzer, André Swart, Murray Jumat and the rest of the workshop for the invaluable help in assembling my test bench and machine.
- Joshua Mitchell for his help and guidance regarding the Pentium system and developing of the control systems.
- My parents, for all their support and encouragement.
- My friends, especially my two housemates Wimpie and Marielle, without whom the last couple of years would have been a lot less fun and manageable.
- The NRF for providing the funding necessary to complete this degree.

Contents

List of Figures

List of Tables

Nomenclature

Variables

u	Voltage	[V]
i	Current	[A]
ψ	Flux Linkage	[Wb − turns]
R	Resistance	[Ω]
L	Inductance	[H]
J	Current Density	[A/mm^2]
p	Pole Pairs	[ ]
θ	Rotor Angle	[rad]
ω	Angular Velocity	[rad/s]
T	Torque	[Nm]
P	Power	[W]
B	Friction Coefficient	[Nm.s/rad]
J (alternatively)	Moment of Inertia	[kg.m^2]
v_w	Wind Speed	[m/s^2]
C_p	Coefficient of Performanc	[ ]
λ	Tip Speed Ratio	[ ]

Abbreviations

ARSG	Assited Reluctance Synchronous Generator
AC	Alternating Current
ARSM	Assisted Reluctance Synchronous Machine
BTB	Back-To-Back
CPSR	Constant Power Speed Range
CRSM	Compensated Reluctance Synchronous Machine
DAC	Digital to Analog Converter
DC	Direct Current
DFIG	Doubly-fed Induction Generator
FE	Finite Element
FOC	Field Oriented Control
FOPDT	First Order Plus Dead Time
HAWT	Horizontal Axis Wind Turbine
HCS	Hill Climb and Search
IG	Induction Generator
IPM	Internal Permanent Magnet
LUT	Lookup Table
MO	Modulus Optimum
MPPT	Maximum Power Point Tracking
MPFPA	Maximum Power Factor Per Ampere
MTPA	Maximum Torque Per Ampere
PF	Power Factor
PMA-RSM	Permanent Magnet Assisted Reluctance Synchronous Machine
PMSG	Permanent Magnet Synchronous Generator
PSC	Position Sensorless Control

PSF	Power Signal Feedback
RPM	Revolutions Per Minute
RSM	Reluctance Synchronous Machine
RTAI	Real-time Applications Interface
SSWT	Small Scale Wind Turbine
TSR	Tip Speed Ratio
VAWT	Vertical Axis Wind Turbine
VSC	Voltage Source Converter
WRSG	Wound Rotor Synchronous Generator

Subscripts

a, b, c	Stator phase axis
d, q	Direct and quadrature axis
s	Stator quantities
e	Electrical
m	Mechanical
f	Field (rotor) quantity

Chapter 1

Introduction

The rapidly increasing need for renewable energy generation systems has led to an increase in the research and development of such systems. One such renewable source is wind power, where electricity is generated by converting the kinetic energy present in the wind into electrical power. While there is some doubt on the environmental impact of large scale wind farms [1], small-scale wind turbines (SSWTs) provide an attractive energy source for owners of small-holdings or farms, small business and remote communities where the connection to the grid is difficult to provide [2]. Some major barriers to entry for the use of SSWTs are the high initial installation cost and intermittent energy supply due to the inherent variability of the wind source.

Forecasts show that the small-scale wind turbine market will have a steady growth in the upcoming years, reaching a cumulative installed capacity of 2 GW by 2020 [3], while there are currently more than 200 SSWT companies worldwide [4]. There is no fixed definition of a power range that qualifies a turbine as small-scale; for this project a range of 1 kW up to 100 kW, with a generated voltage of less than 1000 V_{ac} is assumed [3, 4].

1.1 Small-scale wind turbines

Turbines can be classified as either horizontal axis wind turbines (HAWTs) or vertical axis wind turbines (VAWTs), depending on the position of the rotor axis. Most of the turbines in operation today are two- or three-bladed HAWTs [5, 6]. Traditional HAWTs consist of a tower that supports a nacelle with rotating blades, as shown in Figure 1.1. The nacelle

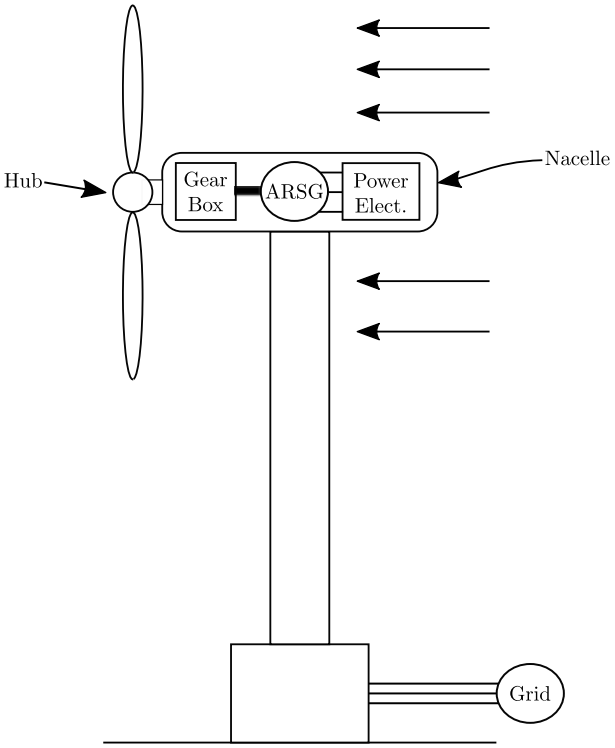

Figure 1.1: A downwind, fixed-pitch, variable speed wind turbine.

hosts the gearbox and generator. Though the power electronics for SSWTs are generally hosted on the ground, they can also be installed in the nacelle and, in the case of a back-to-back (BTB) converter system, they can be split at their common DC-bus link [4]. The specific system topology investigated in this project requires access to the DC-bus link of the converters, thus at least one of the converters need to be installed in the nacelle. Larger turbines usually have an active yaw system and some form of pitch control, while SSWTs are more likely to be fixed-pitched with a passive yaw system.

Wind turbines can operate at either fixed or variable speeds, though variable speed operation is preferable [7–9]. Fixed speed systems can only operate in a narrow band of wind speed, at which it delivers optimum power. The advantage of a fixed speed system is that it does not require additional power electronics, as it can be connected directly to the grid. Variable speed turbines make it possible to capture more energy from a wider range of wind speeds, with reduced mechanical stress on the drive train [10]. The power quality is also improved, as variable speed operation requires the use of power electronics. With the plethora of wind generation topologies, it is difficult to exactly determine the

increase in energy yield by variable speed operation. Nonetheless, a study conducted on a direct drive permanent magnet synchronous generator (PMSG) [8] shows that variable speed operation can increase energy yield up to 16 percent. The following subsections provide a brief overview of some of the components of a SSWT.

1.1.1 Available power in a wind resource

The kinetic energy available in a packet of air can be given as

$$E_k = \frac{1}{2}\rho v_w^2, \tag{1.1}$$

where E_k is the kinetic energy in Joules, ρ is the air density in $\frac{kg}{m^3}$ and v_w is the wind speed [5]. For a wind stream passing through an area A, the flow rate can be given as Av_w. Therefore, the power available in the wind stream can be stated as

$$P_w = \frac{1}{2}\rho A v_w^3. \tag{1.2}$$

Eq. (1.2) presents the total power available in the turbine sweep area A. Practically, the amount of power that can be extracted by a turbine is limited. This limitation is known as the Betz' law and states that the maximum theoretical efficiency of a turbine rotor is 59.3 percent [5, 6]. Modern turbine blades usually achieve an efficiency of between 45 and 50 percent [6]. This efficiency is designated as the turbine's performance coefficient, C_p. The C_p of a fixed-pitch turbine is usually given as a function of the tip speed ratio (λ), which is defined as

$$\lambda = \frac{\omega_w r_b}{v_w}, \tag{1.3}$$

where ω_w is the rotational velocity of the turbine hub and r_b is the rotor radius. This allows a single curve of C_p versus λ to be formulated, as shown in Figure 1.2. Since the optimum value for C_p and λ remain fixed, the maximum power point for all wind speeds can be calculated as shown in Figure 1.3. The updated power equation is given by Eq. (1.4),

$$P_w = \frac{1}{2}\rho C_p(\lambda) A v_w^3. \tag{1.4}$$

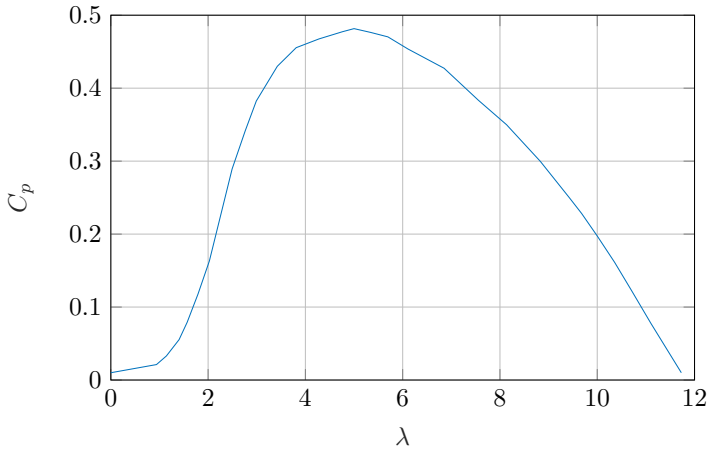

Figure 1.2: An example of a C_p vs λ curve.

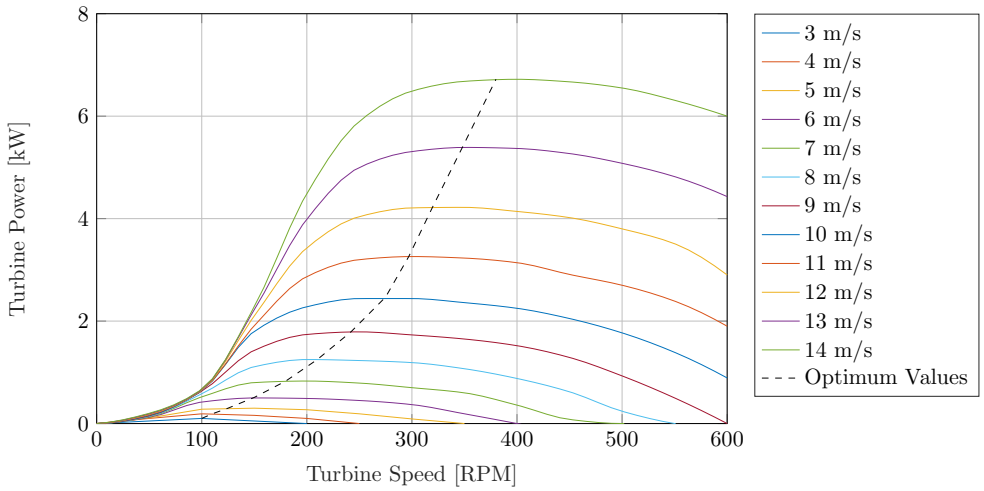

Figure 1.3: Turbine power vs turbine speed for different wind speeds and maximum power point curve.

1.1.2 Drive train

The drive train of a turbine consists of the rotating parts connected to the turbine hub. These generally include the low-speed shaft on the hub side, the gearbox and a high-speed shaft on the generator side. Some of the other components that can be included when modelling the drive train include: the support bearings, any form of coupling, machine brakes and the rotor of the generator. The actual modelling of the drive can be split into different categories i.e., one-, two- or five-mass systems, depending on the amount of drive train components that will be included in the model [7, 11–13]. As this research project deals with a SSWT, a two-mass system is deemed sufficient for modelling and simulation purposes. Under a two-mass system, shown in Figure 1.4, only the effects of the turbine blades and generator are considered, with the stiffness of the shaft being neglected. Both components have an inertia J, damping factor B, and rotational speed ω. The mechanical model of the drive train is then given by

$$\dot{\omega_m} = \frac{(\frac{T_t}{n_g} - T_g) - (B_g + \frac{B_t}{n_g^2})\omega_m}{(J_g + \frac{J_t}{n_g^2})}, \tag{1.5}$$

where the subscripts t and g indicate turbine and generator values, respectively and n_g is the gear ratio. A further simplification can be made by defining J_{tot} and B_{tot} as $J_g + \frac{J_t}{n_g^2}$ and $B_g + \frac{B_t}{n_g^2}$, respectively. The addition of a gearbox in the drive train reduces the efficiency of the system; however, it does lower the required torque rating of the generator. Most SSWT are either direct-drive or use a single stage gearbox.

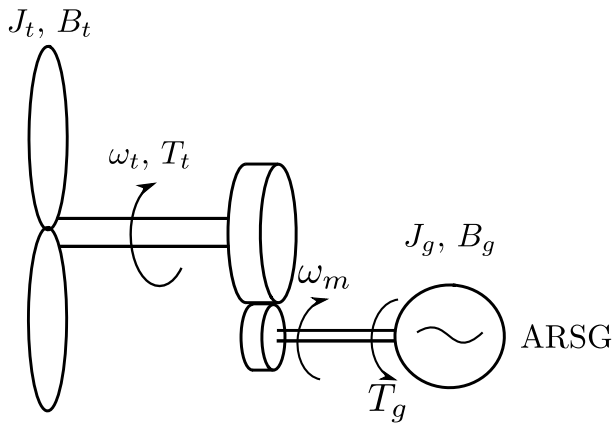

Figure 1.4: Two-mass simplification of a turbine's drive train.

1.1.3 Power electronics

A defining feature of variable speed turbines is their use of power electronics, in the form of voltage source converters, to regulate the power being generated by the turbine. Voltage source converters (VSCs) are devices that convert a DC voltage source into an AC voltage source. There are numerous types of converters in use today, e.g., diode rectifier based converters, BTB converters and matrix converters [14, 15].

The diode rectifier converter is normally used in wound rotor synchronous generator (WRSG) and PMSG systems. It can only transfer power in one direction, i.e. from the generator to the grid. A PMSG system will also have a step-up chopper to adapt the output voltage of the rectifier to match that of the DC link voltage of the grid side inverter. This VSC set up is low cost and simple to implement, but leads to higher harmonic losses [14].

Another popular converter set up is the BTB converters. In this set up, there are two VSCs connected at their common DC link. This allows for bidirectional power flow, and each VSC can be controlled separately. Full control of both VSCs allows for the improvement of the power quality by reducing the total harmonic distortion, though the switching losses might be higher as there are two inverters. The DC-bus link voltage of a BTB converter set up is always at rated, which is generally between 380 and 690 V [14].

1.1.4 Wind generators

Two main competing generator technologies for small-scale variable speed wind turbines are the power conditioned induction generators (IGs) and power conditioned PMSGs [16, 17]. These conventional variable speed wind generator topologies are depicted in Figure 1.5.

While there are IGs that can be operated by direct-grid connection, such as the squirrel-cage IG, this limits the operating speed range of the system, allowing for minimal variable speed operation. In utility-scale wind turbines, the doubly-fed induction generator (DFIG) is commonly adopted due to the economic gain from using only partially rated converters [16]. However, for SSWTs, the PMSG is the preferred generator [7]. The PMSG have a high efficiency, low maintenance costs due to the absence of slip rings and brushes, and does not require an additional power supply for the field excitation.

There has been little research done on the use of a reluctance synchronous machine (RSM) as a generator for wind turbines. The RSM, discussed in more detail in Chapter 2, has some notable advantages over the IG and PMSG. The RSM has a higher efficiency than

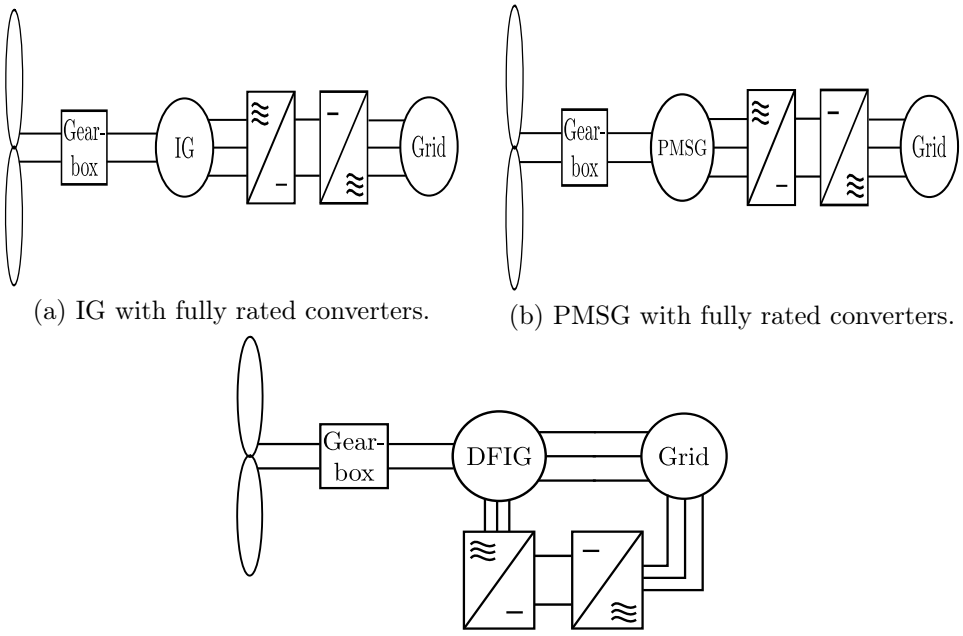

(a) IG with fully rated converters.

(b) PMSG with fully rated converters.

(c) DFIG with partially rated converters.

Figure 1.5: Three commonly used variable speed wind generators.

the IG and is simpler to manufacture [7]. While the PMSG has a higher torque density, the RSM does not require permanent magnets.

1.2 Problem statement

A SSWT needs be cost effective. To achieve this, all the separate subsystems need to be effective. The main drawback to the use of the RSM as generator for a wind turbine is the power factor and complex control, both of which increase the cost of the generator drive system. The main focus of this thesis is to develop a small-scale wind turbine control system that utilises a generator drive system that improves the power factor of the RSM. The assisted reluctance synchronous generator (ARSG) rotor is designed, built and tested. The control system needs to ensure that the generator has good dynamic performance while also operating the turbine at optimum efficiency. Different techniques for variable-speed control of a wind turbine and ARSG are review, with the most suitable controllers chosen, simulated and practically tested. In-house finite element (FE) software is used for the design of the ARSG, while Matlab Simulink is used to simulate the control system

response. The practical tests are carried out with the use of SEW inverters and an in-house built, Linux-based real-time application interface (RTAI) computer.

1.3 Thesis layout

The chapter and content analysis applicable to this research thesis are as follows:

1. **Chapter 2**: In this chapter, a more in-depth look is provided regarding the theory of the RSM and assisted reluctance machine (ARSM), as well as the design of the rotor.

2. **Chapter 3**: This chapter provides a review of the literature on RSM and turbine control and the design of the control systems.

3. **Chapter 4**: This chapter reflects the results of the machine design as well as the control systems.

4. **Chapter 5**: In this concluding chapter, conclusions about the designed systems and suggestions for improvement and future work are provided.

5. **Appendices A**: Contains some of the background mathematical equations.

Chapter 2

Reluctance Synchronous Machine Theory and Design

This chapter contains the theory and design for the RSG. The first section investigates the RSM and presents the concept behind the ARSM and the use of the DC-bus link as the field exciter. The second section supplies useful performance equations that are used in the design and evaluation of the ARSM. The last section contains the design of the ARSM. Note that the terms "machine" and "generator" are used interchangeably, with "machine" being used to reference both motoring and generating modes. The circuits are derived using motoring mode sign convention, in keeping with the notation used in the control system literature for RSMs.

2.1 Reluctance synchronous machine

The RSM is an old concept, first developed by Kostko [18], with further developments as the synchronous reluctance machine or SynRM [19–21] . The RSM, however, shows substandard performance under open-loop voltage and frequency control [7], resulting in slow initial adoption. With the decrease in the cost of VSCs and the advances in rotor design and vector control strategies, the performance of the RSM is now comparable, and in some cases exceeds that of the IM [22–25].

Under closed-loop vector control, the RSM displays some notable advantages over other machines. The RSM has a higher torque density and efficiency than the induction machine

(IM) [26–28]. If designed properly, the RSM also has negligible rotor losses and has no rotor windings, which means no brushes, giving the RSM the same robustness as the IM. While the PMSG still displays a higher efficiency and power factor [11], the RSM does not require rare-earth metals. These characteristics make the RSM more cost effective to design and manufacture.

The RSM does have some major drawbacks. The RSM requires closed-loop control to achieve improved performance, which necessitates the use of a VSC and accurate rotor position tracking. It has a low power factor, especially in generator mode [7, 11], which leads to a higher kVA-rated VSC. This adds to the overall costs and complexity of the system. The RSM also has a very limited constant power speed range (CPSR) [29], though a good CPSR is not necessary in a wind turbine generator drive.

Much research has been done to address these disadvantages. With proper design, the power factor can be improved immensely [30, 31]. To partly solve the need for extra control hardware, work has been done on position sensorless control (PSC) [32–35]. To help increase the constant power speed range, permanent magnets can be placed inside the RSM's flux barriers [36–38]. These machines are referred to as interior permanent magnet (IPM) or permanent magnet assisted reluctance synchronous machines (PMA-RSMs). Other solutions include the compensated and assisted reluctance machines [29]. These will be discussed later in this chapter.

2.1.1 Operation and design

The RSM relies on the principle of magnetic reluctance for its operation. The rotors are designed to be magnetically asymmetrical, creating two different reluctance paths. Figure 2.1 shows a simple rotor design which illustrates this concept. Should the rotor be placed in a rotating magnetic field, the rotor will rotate synchronously with the magnetic field in an attempt to create a path of least reluctance. This low reluctance is referred to as the d-axis, while the high reluctance path is referred to as the q-axis and consists of as much air as possible.

In practice, current is applied to the stator windings to create magnetic poles, which induce opposite poles on the rotor. Varying the current sinusoidally will rotate the magnetic poles created by the stator current. This will cause the induced poles on the rotor to rotate synchronously with the stator poles, thus creating torque. In motoring mode, the

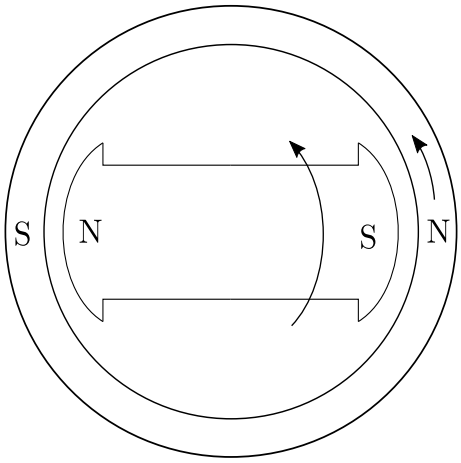

Figure 2.1: A simple rotor to demonstrate the operation of a RSM.

current vector i_s as well as the flux vector ψ_s leads the rotor, thus pulling the rotor in the direction of movement. In generator operation, i_s and ψ_s lag the rotor. Rotor designs of high performance RSMs do not use this simplified design, instead relying on the careful placement of flux barriers to create high and low reluctance paths. One pole of an 8-pole RSM is shown in Figure 2.2, indicating the different axes and flux barriers. The two different flux paths are shown in Figure 2.3. The design of the barriers are thus crucial to ensure optimum machine performance. As such, a lot of design optimisation research has been done on the shape of the barriers [19, 22–24, 31, 39–46].

Most of the research focuses on either increasing the saliency ratio ($\frac{L_d}{L_q}$) [44] or increasing torque and decreasing torque ripple [22, 23, 43, 45]. Work has also been done on machine optimisation for efficiency [24, 29, 37, 41] and on flux barrier design to improve the power factor [31]. The effects of skewing and stator chording are investigated in [47]. The effects that the different machine parameters, such as the flux barrier width and air-gap, have on the performance are investigated in [27], and the effect of the number of flux barriers and stator slots are presented in [23]. When considering the machine volume and cost, it becomes clear that an optimum RSM rotor design is a highly non-linear, multi-objective problem.

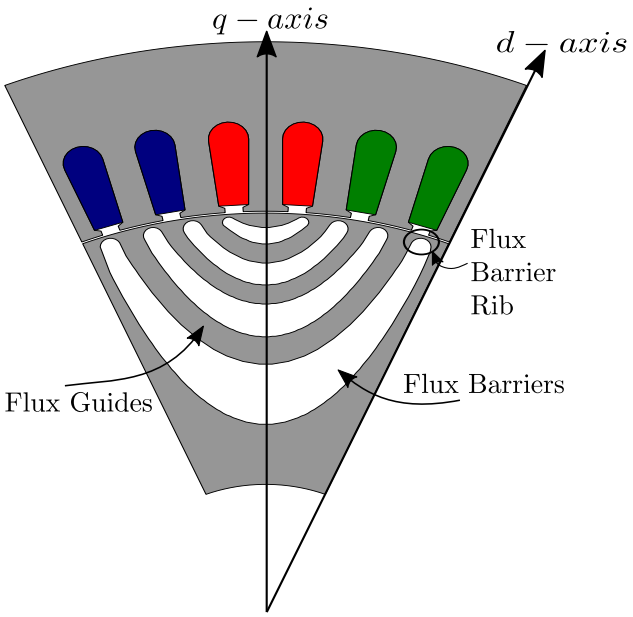

Figure 2.2: One pole model of an 8-pole RSM with the DQ-axes shown.

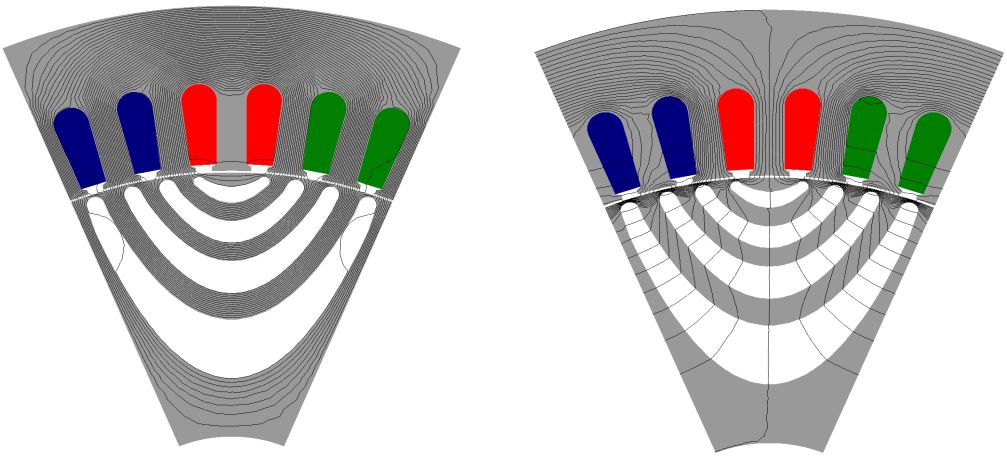

(a) D-axis flux lines.

(b) Q-axis flux lines.

Figure 2.3: Flux lines to illustrate the two different flux paths created by the flux barriers.

2.2 Assisted reluctance synchronous machine

Besides the rotor design optimisation methods referenced above, other improvements which propose physical alterations to the rotor also exist. The best known of these modifications is the PMA-RSM. This entails adding low-cost ferrite magnets to the rotor of a RSM, which

increases the torque density and power factor of the machine [48]. The magnets are inserted such that they oppose the q-axis flux linkage. PMA-RSMs are similar to conventional IPM machines, but use less magnets that have lower magnetic strength [48, 49]. This reduction in q-axis flux linkage leads to an increase in produced torque, which can be seen by studying the torque equation for an RSM, $T = \left(\frac{3p}{2}\right)\left(\psi_d i_q - \psi_q i_d\right)$. This also leads to a smaller q-axis inductance, improving the saliency ratio of the machine. An increase in saliency ratio has been shown to lead to an increase in the power factor [44, 50]. Lastly, the addition of the permanent magnets (PMs) result in a lower supply voltage needed at rated and over rated conditions, which lowers the required inverter kVA rating.

The other proposed topologies [29], are called the compensated reluctance synchronous machine (CRSM) and the ARSM, which add a rotor winding on either the q- or the d-axis, respectively. An illustration of these topologies is shown in Figure 2.4. These rotor topologies aim to solve, at least partially, the drawbacks of the RSM without the use of PMs or additional power electronics. The authors also suggest using the DC-bus link of BTB VSCs as the exciter for the field winding.

This type of rotor would place both the CRSM and the ARSM in the wound rotor, DC-excited synchronous machines category. In the CRSM, the rotor winding serves the same purpose as the magnets in the PMA-RSM. In the ARSM, the field winding generates positive d-axis flux, thus requiring a lower d-axis current, instead of lowering the q-axis flux linkage. The focus of this thesis will be on the ARSM, specifically as a generator in a wind

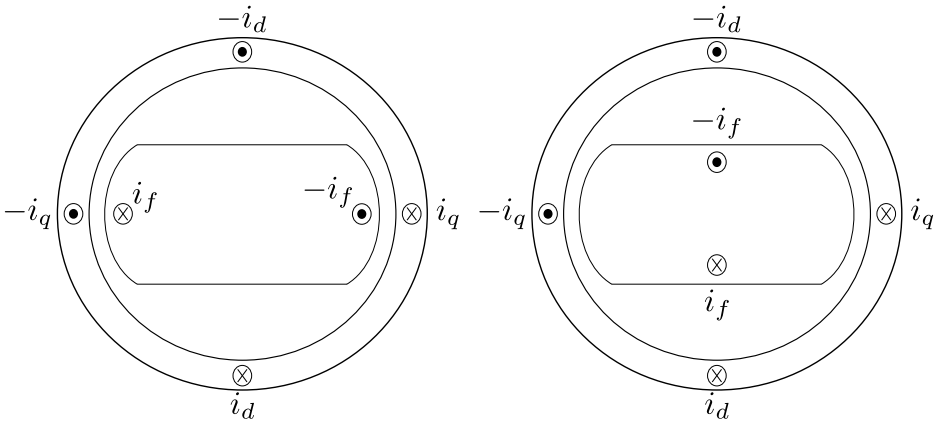

Figure 2.4: The (a) CRSM rotor and (b) the ARSM rotor

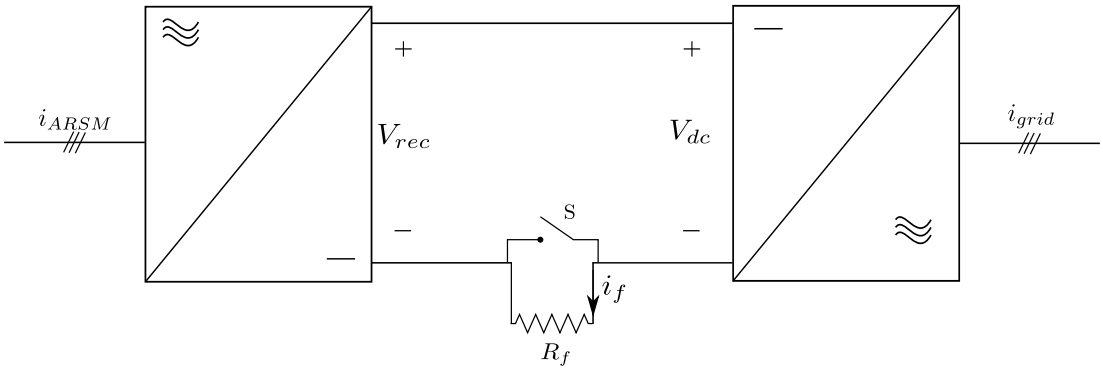

(a) Series rotor connection.

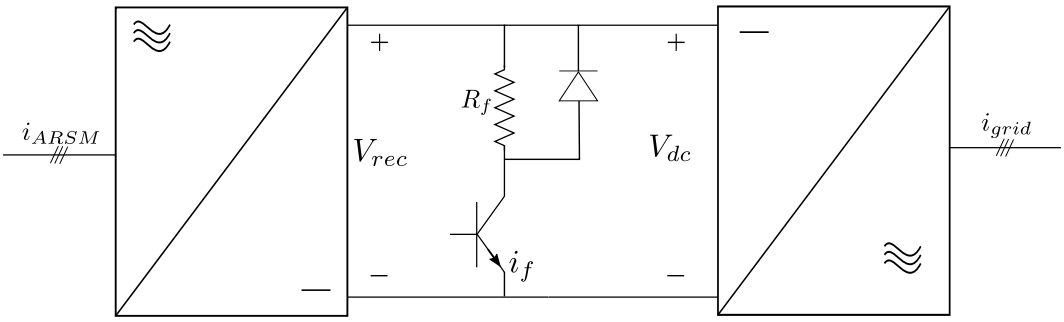

(b) Parallel rotor connection.

Figure 2.5: Two connection topologies for connecting the rotor winding of the ARSM.

turbine set up. There are two ways that the rotor can be connected to the DC-bus link, as shown in Figure 2.5. The advantage of the series connection in Figure 2.5a is that it does not require any extra power electronics to function. The drawback to this connection is the lack of control over the field current. The parallel connection shown in Figure 2.5b provides full control of the rotor current, but it requires the use of an extra voltage converter.

For this project, the series connection is used. The proposed generator drive is shown in Figure 2.6. In Figures 2.5 and 2.6 the field winding is displayed by the field resistance R_f, though the rotor winding has a significant inductance also. Some of the benefits of this connection and the ARSM are:

1. Should the status of DC-link connection be monitored, the switch can be closed in case of an emergency or fault, and the machine can be operated as a RSG, resulting in less downtime.

2. The assisted winding acts as a DC-link filter inductance, i.e. as a "choke" inductor,

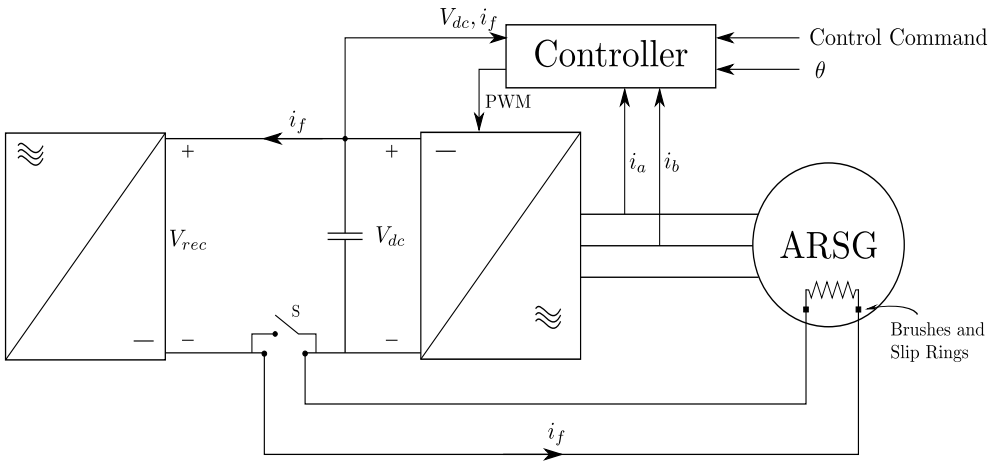

Figure 2.6: Proposed ARSG drive.

thus saving costs.

3. Certain PSC methods, such as a rotating high frequency voltage injection method, may be measured at the DC field terminals (across the switch), thus simplifying the PSC of the drive.

4. The improved power factor at rated conditions result in a lower inverter kVA rating, reducing the cost of the overall system.

5. Since the DC-bus link current increases as the power in the system increases, the winding, slip rings and brushes would only conduct the rated field current when the turbine is producing rated power. This minimises the losses in the rotor winding during low power situations.

One of the most obvious disadvantages of the ARSM is the brushes and slip rings. This increases the maintenance and costs of the system, but the use of slip rings are not uncommon in wind turbines e.g., in DFIGs or traditional WRSGs. The control and design of the ARSM is also more complex than a RSM.

2.3 Performance equations of the ARSG

This section provides the equations that are used to analytically evaluate the different performance aspects of the ARSG design. The modelling and evaluation is done in steady

state, hence the equations and equivalent circuit diagrams are all representative of steady state operation. A full derivation of the ARSM including system dynamics is done in Chapter 3.

The analytical evaluation is based on the equivalent steady-state dq circuits, shown in Figures 2.7a and 2.7b, and the phasor diagram, shown in Figure 2.7c. The circuits and equations are given with the machine in generator mode.

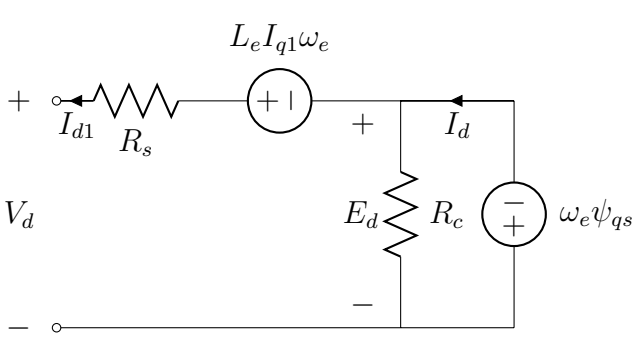

(a) D-axis circuit

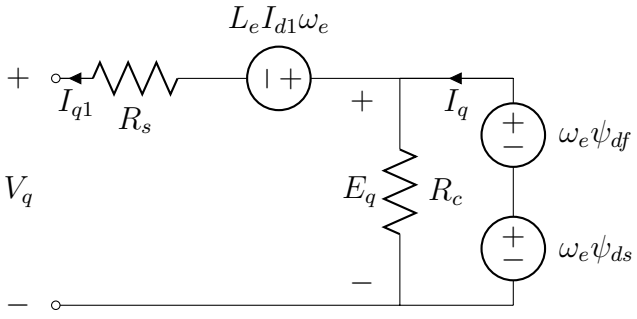

(b) Q-axis circuit

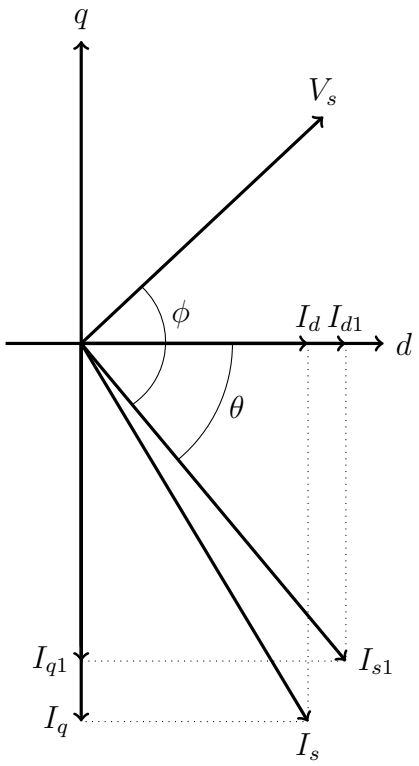

(c) Phasor Diagram

Figure 2.7: The DQ equivalent circuits and phasor diagram of the ARSG.

The only notable difference between the equivalent circuits drawn in Figure 2.7 and the dq circuits of a conventional RSG is the additional speed voltage term on the q-axis circuit. With the addition of the field winding, the generator's respective flux linkages can be written as

$$\begin{aligned}\psi_d &= \psi_{ds} + \psi_{df} \\ &= L_d I_d + L_{df} i_f, \qquad (2.1)\\ \psi_q &= \psi_{qs} = L_q I_q, \qquad (2.2)\\ \psi_f &= \psi_{ff} + \psi_{df} \\ &= L_f I_f + L_{df} i_d. \qquad (2.3)\end{aligned}$$

From the equivalent circuits, the steady state d- and q-axis voltage equations are given by

$$\begin{aligned}V_d &= E_d - L_e I_{q1}\omega_e - I_{d1}R_s,\\ V_q &= E_q + L_e I_{d1}\omega_e - I_{q1}R_s, \qquad (2.4)\end{aligned}$$

with R_s being the stator winding resistance, E_d and E_q the speed voltages ($-\omega_e\psi_q$ and $\omega_e\psi_d$, respectively), and ω_e being the electrical rotor speed. The voltage contribution of the end winding leakage inductances is shown as $L_e I_{q1}\omega_e$ and $L_e I_{d1}\omega_e$, with I_{d1} and I_{q1} being the total d- and q-axis currents at the terminals V_d and V_q. The equations used to calculate L_e are given in Appendix A. The core resistance R_c can be calculated by

$$R_c = \frac{3E_a^2}{P_{core}}, \qquad (2.5)$$

with E_a being the RMS value of the induced voltages, given by

$$E_a = \sqrt{0.5\big(E_d^2 + E_q^2\big)}. \qquad (2.6)$$

P_{core} can be calculated analytically, as illustrated in [41, 51], nut the analytical calculation falls outside the scope of this study. The currents I_{d1} and I_{q1} can be calculated by

$$I_{d1} = I_d + \frac{\omega_e\psi_q}{R_c}, \qquad (2.7)$$

$$I_{q1} = I_q - \frac{\omega_e\psi_d}{R_c}, \qquad (2.8)$$

with I_d and I_q being the current inputs. With these values known, the power factor of the generator can be calculated by

$$\phi = atan\left(\frac{V_q}{V_d}\right) - atan\left(\frac{I_{q1}}{I_{d1}}\right), \tag{2.9}$$

$$PF = \cos\phi. \tag{2.10}$$

Other performance characteristics that are evaluated, include the generator torque T_g, torque ripple T_r and efficiency η_g, given in Eq. (2.11), Eq. (2.12) and Eq. (2.13) respectively.

$$T_g = \left(\frac{3p}{2}\right)\left(\psi_d I_q - \psi_q I_d\right), \tag{2.11}$$

$$T_r = \frac{T_{max} - T_{min}}{T} \times 100\%, \tag{2.12}$$

$$\eta_g = \left(P_{out}/P_{in}\right) \times 100\%. \tag{2.13}$$

P_{out} can be determined as

$$P_{out} = P_{in} - P_{losses}, \tag{2.14}$$

with $P_{in} = T_g\omega_m$ and the losses consisting of copper losses (P_{cu}), stator core losses (P_c) and the friction and windage losses (P_{fw}). The rotor iron losses (eddy current and hysteresis losses) are assumed to be negligible. P_{cu} is given by

$$P_{cu} = \underbrace{3I_{s1}^2 R_s}_{\text{Stator Losses}} + \underbrace{I_f^2 R_f}_{\text{Rotor Losses}} . \tag{2.15}$$

The method and equations used to determine the number of turns and the field current are given below, as they are presented in [29]. Assuming the losses in the inverter are negligible, i.e., a unity efficiency, for the power balance to hold,

$$I_f V_{dc} = 3V_s I_s \cos\theta, \tag{2.16}$$

from which the rated field current can be approximated by

$$I_{f(rated)} = \frac{\eta_g P_{in(rated)}}{V_{rec}}. \tag{2.17}$$

In Eq. (2.16), V_{DC} is the DC-bus link voltage, which is kept constant at the rated value of the inverter. In Eq. (2.17), P_{in} is the rated mechanical shaft power of the ARSG at I_f = 0 A and $V_{rec} = V_{dc} + i_f R_f$.

The equation used to determine the number of rotor turns per slot z_f is given by

$$z_f \leq \frac{J_f A_f k_f}{I_f}, \tag{2.18}$$

where J_f is the field current density, A_f is the field slot area per pole and k_f is the fill factor of the field winding. Determining the best possible z_f is not trivial, as this depends on (i) how effectively the rotor winding generates the field flux and (ii) to what extent the rotor winding must assist the stator d-axis. One method is to first calculate the maximum d-axis flux linkage $\psi_{d(rated)}$ with I_f set to zero. Then, with the current angle $\theta = 90°$, z_f is increased with the chosen field current density until the required percentage of the rated flux linkage is reached, keeping in mind that z_f can not exceed the limitation placed on it in Eq. (2.18).

2.4 Assisted reluctance synchronous generator design

The Electrical Machines Lab's in-house developed FE program, SEMFEM, is used for the design and evaluation of the different rotor topologies. The stator and its model is provided by ACTOM, a manufacturer and supplier of electro-mechanical equipment. During the FE design of the ARSG, the simulations are run using current density. This allows the design of the generator without the need to know exactly how many turns there need to be on the rotor winding. The rated stator current density is $J_s = 6.1\ A/mm^2$. The rotor designs are all 8-pole, 1.7 kW and with a rated speed of 750 revolutions per minute (RPM). The rotors under evaluation in this section are not optimised and serve only as a proof-of-concept for the topology and control systems developed in the next chapter. A RSG-rotor is designed first, with this basic layout used as a basis for the ARSG design and comparisons. Four different ARSG rotor designs are done, with the evaluations done for the following criteria: torque, torque ripple, power factor, efficiency, total rotor copper area and the relative inverter size under rated conditions. All the rotors are skewed, to ensure the torque ripple is minimised.

2.4.1 RSG

To aid the design process, the following decisions are made with regards to the rotor structure:

1. The shape of the flux barriers are parabolas.
2. The number of flux barriers is chosen as 4.
3. The rib height is chosen as 0.5 mm.
4. The width of each individual iron flux guide is kept constant.

A small script is written which draws the parabola using the formula $y = ax^2 + k$, where k is the offset from the origin and a is given by $a = \frac{(y-k)}{x^2}$. The ribs are formed by connecting the flux barrier lines with a circle.

Figure 2.8 shows the RSG rotor. Figure 2.9 shows the torque, power factor and efficiency curves of the RSG calculated using static FE analysis and the analytical models described in Section 2.3. Table 2.1 gives the rated values of this machine at the chosen operating point. These are the values that are used as the baseline comparison in the next section.

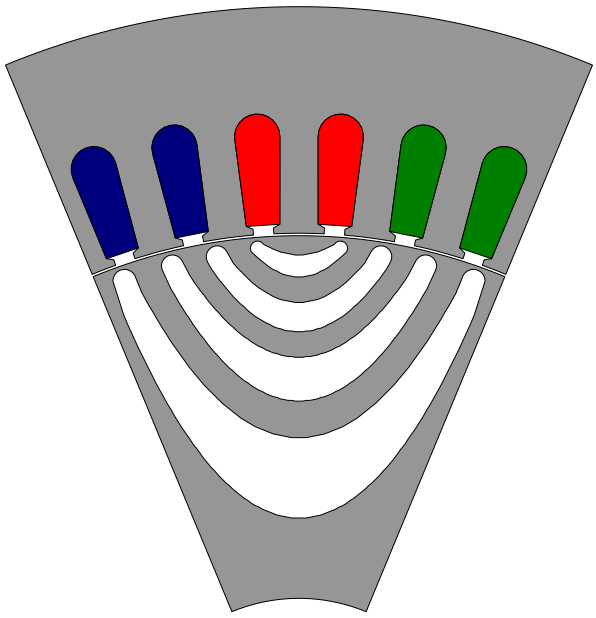

Figure 2.8: One pole of the 8-pole RSG rotor and stator.

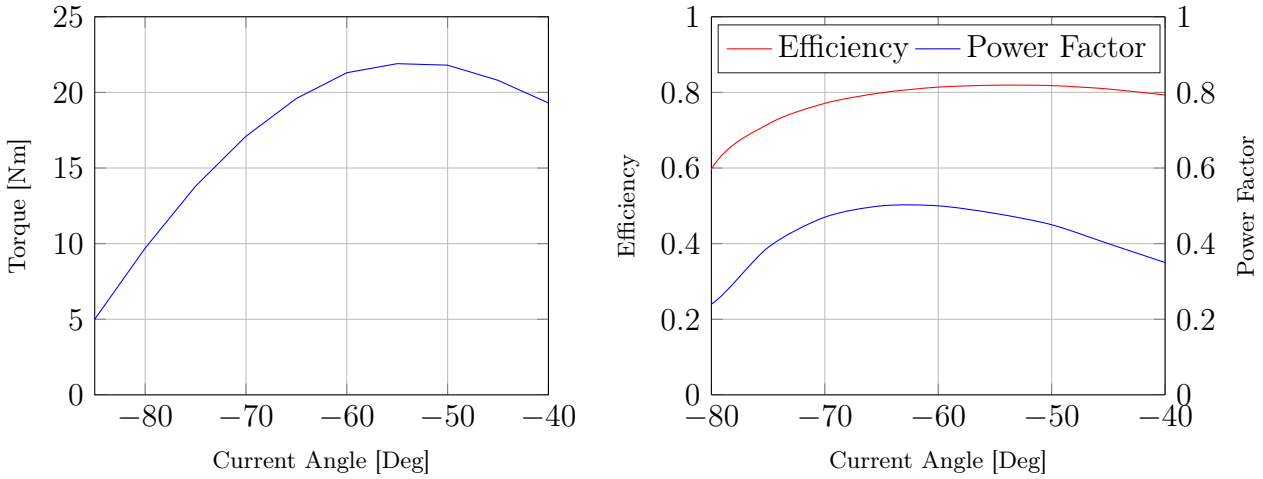

(a) Torque versus current angle.

(b) Efficiency versus current angle.

Figure 2.9: Performance curves of the RSG.

Table 2.1: RSG specifications.

RSG Specifications							
J_s $[A/mm^2]$	θ [°]	P_{in} [kW]	T_g [Nm]	T_r [%]	PF []	Eff [%]	S_{inv} [kVA]
6.1	55	1.7	22	6.8	0.48	84.6	3.6

J_s - Stator Current Density; θ - Current Angle; P_{in} - Generator Input Power; T_g - Average Torque; T_r - Torque Ripple; PF - Power Factor; Eff - Efficiency; S_{inv} - Inverter Rating;

2.4.2 Assisted RSG

Using the RSG design as a basis, four different ARSG topologies are investigated. The first option involves removing the top two barriers of the RSG and replacing them with a winding slot, as shown in Figure 2.10a. The field slot shape is also based on the parabola form used for the flux barriers. The slot ribs are the same thickness as the barrier ribs. In the second design, a small winding slot is added in place of the first flux barrier, with the second and third flux barriers modified so that they can also be wound. This option is shown in Figure 2.10b. The slot ribs are 0.75 mm thick. The third design keeps the same layout as the previous design, with the bottom flux barrier also forming part of the field

winding, as shown in Figure 2.10c. The last design evaluated does not use a separate rotor slot at all. Instead, it uses the first three barriers as winding slots. This model is shown in Figure 2.10d.

To compare these different rotor designs, they are all simulated with and without field current. To simplify the design for this study, the rated field current density is chosen as 6 A/mm^2, and z_f is calculated to provide the maximum amount of assistance to the stator d-axis. The value of I_s is then determined using Eq. (2.16), for the rated current angle, in this case -50°. The results are compared using the RSG as a baseline. The relevant performance outcomes, as dictated by the criteria mentioned earlier, is shown in Table 2.2.

Table 2.2: Rotors comparison with J_f set at 0 and 1 p.u. RSG data are given for comparison.

Unit	T_g [Nm]	T_r [%]	PF []	Eff [%]	A_f $[mm^2]$	J_s $[A/mm^2]$
RSG	22	6.8	0.48	84.6	n/a	6.1
ARSG 1: $J_f = 0$ p.u.	21.5	12.5	0.44	82.9	209	6.1
ARSG 1: $J_f = 1$ p.u.	22	9.9	0.73	86.1	"	3.87
ARSG 2: $J_f = 0$ p.u.	21.9	13.5	0.46	83.5	292.3	6.1
ARSG 2: $J_f = 1$ p.u.	22	10.3	0.72	83	"	3.87
ARSG 3: $J_f = 0$ p.u.	22.2	16.9	0.49	83.6	658	6.1
ARSG 3: $J_f = 1$ p.u.	22	12	0.74	72.5	"	3.7
ARSG 4: $J_f = 0$ p.u.	22.1	12.5	0.45	83.5	290	6.1
ARSG 4: $J_f = 1$ p.u.	22	13.3	0.73	82.6	"	3.87

T_g - Average Torque; T_r - Torque Ripple; PF - Power Factor; Eff - Efficiency; A_f - Slot Area; J_s - Stator Current Density

The first rotor design is chosen, as it had the best efficiency and uses the least amount of copper. From the comparison shown in Figure 2.11, the addition of the slot to the RSG results in a slight decrease in power factor but does not significantly affect the torque or the efficiency. When J_f is at the rated value, there is a big increase in the power factor, as well as a significant increase in the efficiency of the ARSG.

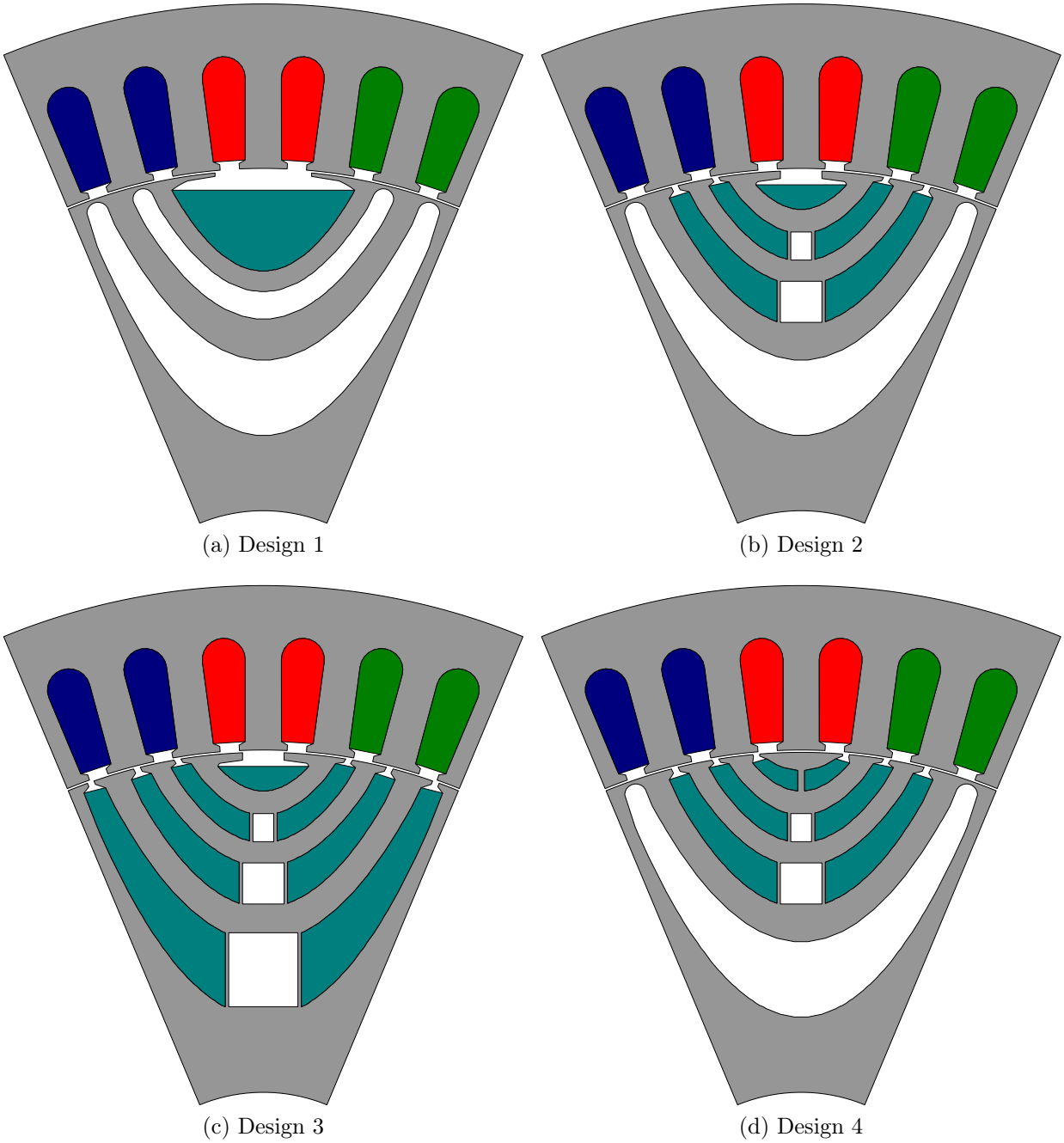

(a) Design 1

(b) Design 2

(c) Design 3

(d) Design 4

Figure 2.10: Different design options for the A-RSG, based on the normal RSG.

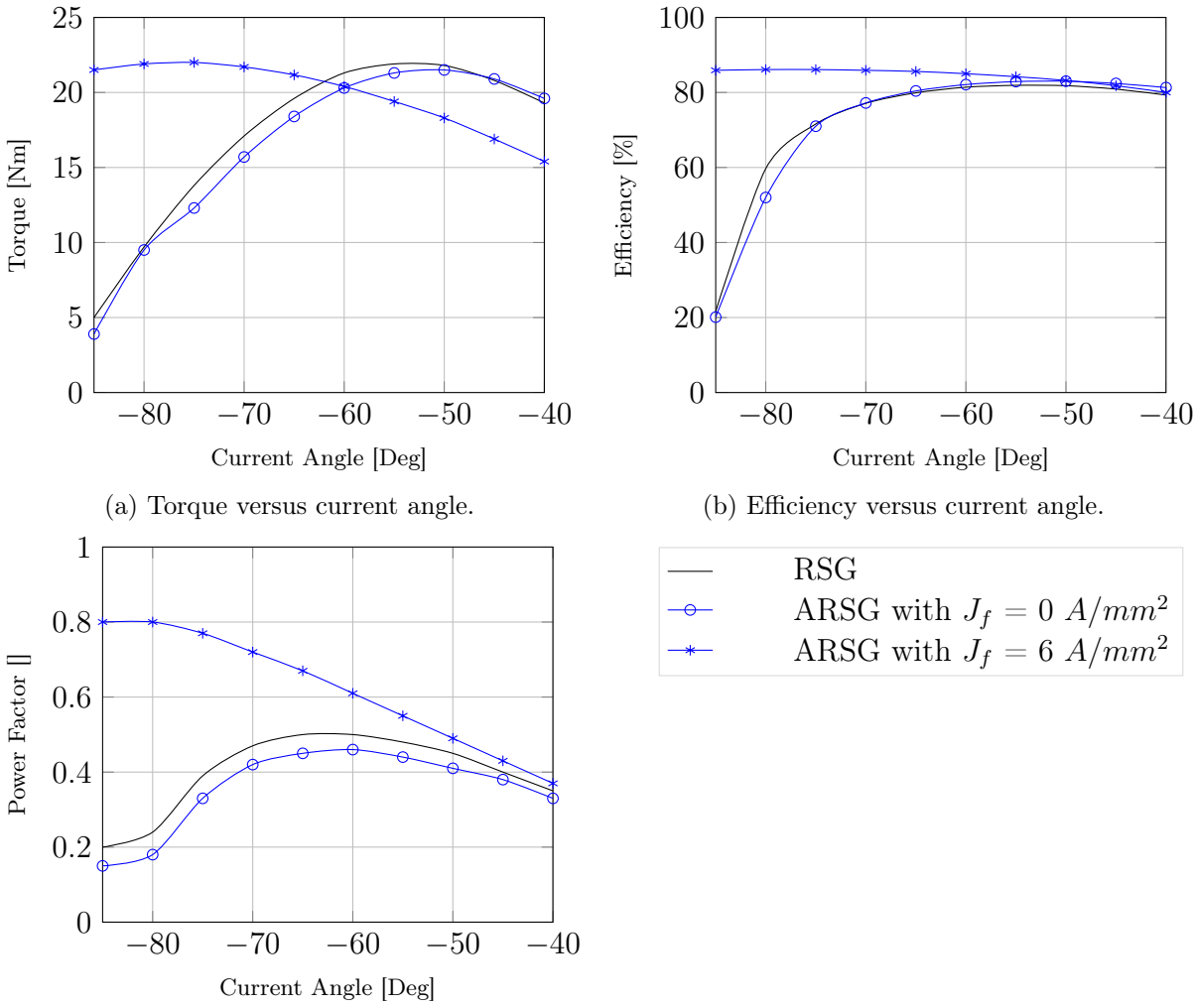

(a) Torque versus current angle.

(b) Efficiency versus current angle.

(c) Power factor versus current angle.

Figure 2.11: Performance comparison between the RSG and ARSG at $J_f = 0$ and 6 A/mm^2.

Using Equations (2.17) and (2.18) to determine the rated current and the number of turns, the final ARSG specifications are given in Table 2.3.

Table 2.3: Final performance comparisons.

	T_g	T_r	PF	Eff	S_{inv}	J_s	J_f	z_f
Unit	[Nm]	[%]	[]	[%]	[kVA]	$[A/mm^2]$	$[A/mm^2]$	[]
RSG	22	6.8	0.48	84.6	3.6	6.1	n/a	n/a
ARSG	22	9.9	0.73	86.1	2	3.87	6	150

T_g - Average Torque; T_r - Torque Ripple; PF - Power Factor; Eff - Efficiency; S_{inv} - Inverter Rating; J_s - Stator Current Density; J_f - Field Current Density; z_f - Field Winding Turns

Chapter 3

Control System Theory and Design

This chapter contains the theory and design for the control of the various subsystems of a wind turbine system. The first section contains the derivation of a full mathematical dq-model of the ARSM. Afterwards, the theory and design of the current, torque and wind turbine controllers are presented in their respective sections.

3.1 ARSM mathematical model

The derivation of the mathematical model of the ARSM is given below. This is a combination of the work done in [29] and [52]. For this derivation, the effects of core losses and end winding leakage inductances are ignored.

Q-axis circuit

The q-axis voltage equation is given as

$$u_q = R_s i_q + \frac{d\psi_q}{dt} + \omega_e \psi_d, \tag{3.1}$$

where ψ_d is as given in Eq. (2.1). The derivative of the q-axis flux linkage can be written as shown in Eq. (3.2). The change in flux linkage with rotor position is omitted, as it is small enough to be negligible [26].

$$\begin{aligned}\frac{d}{dt}\psi_q &= \frac{\partial\psi_q}{\partial i_q}\frac{di_q}{dt} + \frac{\partial\psi_q}{\partial i_d}\frac{di_d}{dt} \\ &= L_q\frac{di_q}{dt} + L_{dq}\frac{di_d}{dt}.\end{aligned} \tag{3.2}$$

In Eq. (3.2) the q-axis inductance is represented by L_q and the mutual inductance by L_{dq}. Substituting this result back into Eq. (3.1) gives the equation describing the q-axis of the ARSM. The circuit is shown in Figure 3.1.

$$u_q = R_s i_q + L_q\frac{di_q}{dt} + L_{dq}\frac{di_d}{dt} + \omega_e\psi_d. \tag{3.3}$$

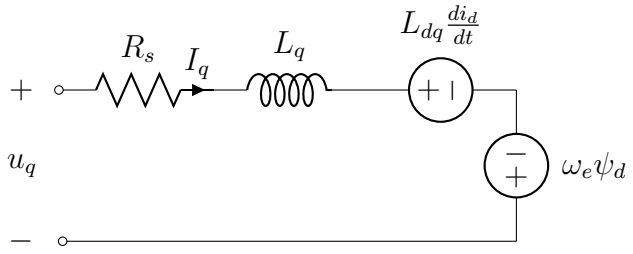

Figure 3.1: q-axis circuit diagram.

D-axis circuit

To get the complete d-axis winding model, the field circuit needs to be referred from the rotor to the stator. To achieve this, it is necessary to define the effective winding ratio between the d-axis and field winding. This can be stated as

$$a_{eff} = \frac{k_{w1}N_1}{k_{wf}N_f}, \tag{3.4}$$

where $k_{w1}N_1$ and $k_{wf}N_f$ are the effective turns in series for the d-axis winding and the field winding respectively.

The equation for the d-axis and field winding voltages is given by

$$u_d = R_s i_d + \frac{d}{dt}\psi_d - \omega_e \psi_q, \tag{3.5}$$

$$u_f = R_f i_f + \frac{d}{dt}\psi_f. \tag{3.6}$$

For this part of the derivation, the copper losses, the q-axis speed voltage and mutual inductances are left out, with the voltage equations then becoming,

$$u_d = \frac{d}{dt}\psi_d, \tag{3.7}$$

$$u_f = \frac{d}{dt}\psi_f. \tag{3.8}$$

The above equations can be rewritten such that they are expressed using the machine inductances, as shown in Eq. (3.9).

$$\left.\begin{aligned} u_d &= L_d \frac{di_d}{dt} + L_{df}\frac{di_f}{dt}, \\ u_f &= L_f \frac{di_f}{dt} + L_{df}\frac{di_d}{dt}. \end{aligned}\right\} \tag{3.9}$$

The mutual inductance L_{df} is given by

$$L_{df} = \frac{k_{w1}N_1\varphi_{fd}}{i_f} = \frac{k_{wf}N_f\varphi_{df}}{i_d}, \tag{3.10}$$

where $\varphi_{fd}, \varphi_{df}$ are the mutual fluxes between the axis windings. The fluxes of the respective windings can be given as

$$\varphi_d = \varphi_{ld} + \varphi_{fd}, \tag{3.11}$$

$$\varphi_f = \varphi_{lf} + \varphi_{df}. \tag{3.12}$$

From Equations (3.10) and (3.11) and using Eq. (3.4), the d-axis inductance can be expressed as

$$L_d = \frac{k_{w1}N_1\varphi_d}{i_d} = \frac{k_{w1}N_1\varphi_{ld}}{i_d} + \frac{k_{w1}N_1\varphi_{fd}}{i_d} \tag{3.13}$$

$$= L_{ld} + aL_{df} \tag{3.14}$$

$$= L_{ld} + L_{md}. \tag{3.15}$$

Similarly, an expression for the field inductance can be given by

$$\begin{aligned} L_f &= \frac{k_{wf} N_f \varphi_f}{i_f} \\ &= \frac{k_{wf} N_f \varphi_{lf}}{i_f} + \frac{k_{wf} N_f \varphi_{df}}{i_f} \\ &= L_{lf} + \frac{L_{fd}}{a} \\ &= L_{lf} + L_{mf}. \end{aligned} \tag{3.16}$$

From Eq. (3.15) and Eq. (3.16), note that $L_{md} = aL_{df} = a^2 L_{mf}$.
Now, let

$$\left.\begin{aligned} \frac{u_{fd}}{u_f} &= a, \\ \frac{i_{fd}}{i_f} &= \frac{1}{a}. \end{aligned}\right\} \tag{3.17}$$

Substituting these results back in Eq. (3.7), so that the voltage induced in the d-axis is given as

$$u_d = \frac{d\psi_d}{dt} = L_{ld}\frac{di_d}{dt} + L_{md}\frac{di_d}{dt} + aL_{df}\frac{di_{fd}}{dt} \tag{3.18}$$

$$= L_{ld}\frac{di_d}{dt} + L_{md}(\frac{di_d}{dt} + \frac{di_{fd}}{dt}). \tag{3.19}$$

Similarly, the voltage induced in the field winding can be given by

$$u_{fd} = au_f = a(\frac{d\psi_f}{dt}) = a(L_{lf}\frac{di_f}{dt} + L_{mf}\frac{di_f}{dt} + L_{df}\frac{di_d}{dt}) \tag{3.20}$$

$$= a(L_{lf}a\frac{di_{fd}}{dt} + \frac{L_{md}}{a^2}a\frac{di_{fd}}{dt} + \frac{L_{md}}{a}\frac{di_d}{dt}) \tag{3.21}$$

$$= L_{lf}a^2\frac{di_{fd}}{dt} + L_{md}\frac{di_{fd}}{dt} + L_{md}\frac{di_d}{dt} \tag{3.22}$$

$$= L_{lfd}\frac{di_{fd}}{dt} + L_{md}(\frac{di_{fd}}{dt} + \frac{di_d}{dt}). \tag{3.23}$$

Adding the losses, mutual inductances and speed voltages to Eq. (3.19) and Eq. (3.23) completes the voltage equations, which are given in Equations (3.24) and (3.25). The circuit diagram is shown in Section 3.1.

$$u_d = R_s i_d + L_{ld}\frac{di_d}{dt} + L_{qd}\frac{di_q}{dt} + L_{md}(\frac{di_d}{dt} + \frac{di_{fd}}{dt}) - \omega_e \psi_q, \tag{3.24}$$

$$u_{fd} = R_{fd} i_{fd} + L_{lfd}\frac{di_{fd}}{dt} + L_{md}(\frac{di_{fd}}{dt} + \frac{di_d}{dt}). \tag{3.25}$$

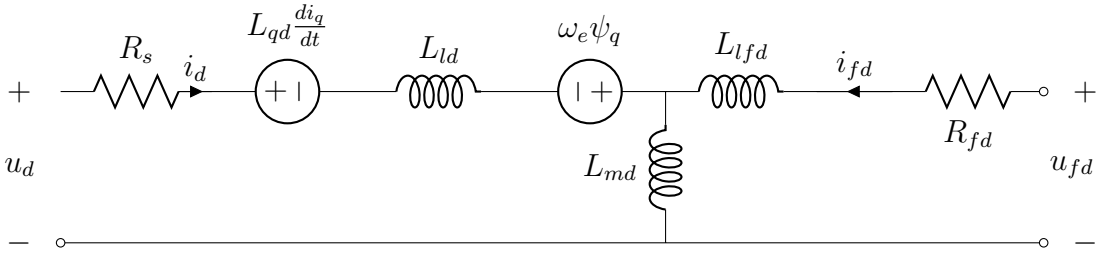

Figure 3.2: Combined direct and field circuit diagrams.

3.2 Controller design

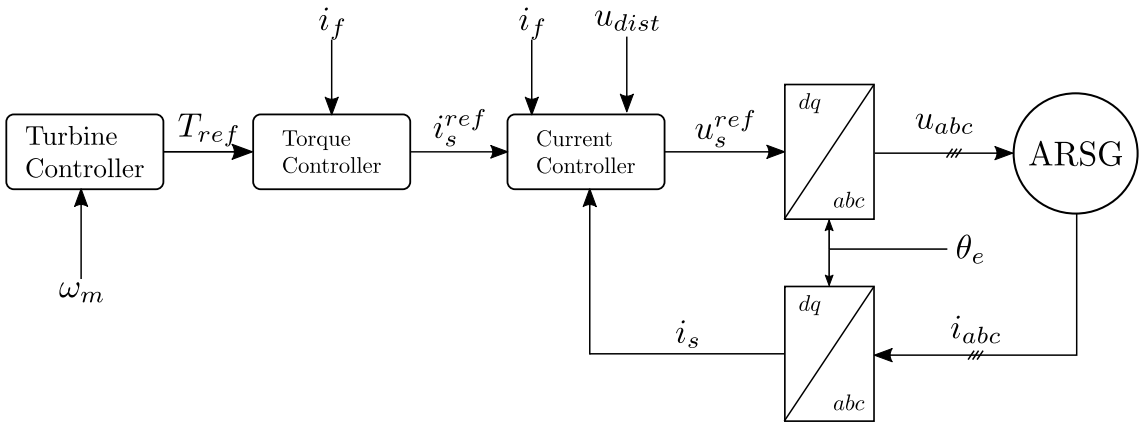

Figure 3.3: The proposed cascaded control structure.

The proposed control structure is shown in Figure 3.3. This structure is of a cascading nature, consisting of three layers, with the innermost part consisting of a current controller. The development of current controllers for reluctance synchronous machines has been extensively researched [7, 11, 26, 32–36, 53]. All of these use classical PI control, based on field orientated control (FOC) or vector control, and utilises space vector PWM (SVPWM) [33].

The second, or middle, control loop consists of a controller that supplies the current reference. These typically consist of either speed control [7, 26, 32, 36, 54] or torque control [11, 55–59]. Only torque control is considered here.

The outermost control loop is the turbine controller. This generates either a torque or speed reference, depending on the control structure used. This control loop is engaged with the maximum power extraction from the turbine [60]. These control algorithms are classified as maximum power point tracking (MPPT) algorithms, and have been the focus of wide-ranging research [60–65]. The algorithms can be divided into three main research areas, namely tip speed ratio (TSR) control, hill-climb and search (HCS) control and power signal feedback (PSF) control [64, 65].

The remainder of this chapter is devoted to a more detailed discussion of the control loops mentioned above.

3.2.1 Current control

As mentioned, the various current control strategies reviewed use a classical PI structure. This controller structure calculates the reference voltages that will induce the reference current. Some authors developed discrete controllers [7, 32, 36], but this did not provide significant performance improvements, as the switching and sampling frequencies of the practical system are very high [11]. Both fixed gains [32] and gain scheduling methods [7, 11] are investigated. While the fixed gain controllers perform satisfactorily and are easier to design and implement, the highly non-linear nature of the ARSM suggests that the current controls would benefit from the non-linear nature of a gain scheduling strategy.

Referring to Equations (3.3) and (3.24), the cross coupling due to the speed voltage and mutual inductances are evident. Two separate feed-forward compensation strategies are present in literature to handle these terms. One method, presented in [34], involves rewriting the dq-voltage equations in their respective state space form and simultaneously solving the current derivatives. The resulting answer is then manipulated to create an auxiliary inductance, $L^d_{s,aux}$ and $L^q_{s,aux}$, for each axis. This inductance term is combined with the speed voltage term to form a disturbance term, which is decoupled from the controller by using disturbance compensation. This is an elegant solution for the decoupling procedure of a RSM, where there are only two axis equations. However, the d-axis of the ARSM contains a term from the rotor circuit, which makes the derivation of auxiliary

inductances non-trivial.

The second method, suggested in [53], is used in the design of the controllers, with a small adjustment to account for the rotor circuit cross magnetisation term, rewriting Equations (3.3) and (3.24) as

$$u_d + \omega_e \psi_q - L_{qd}\frac{di_q}{dt} - L_{md}\frac{di_{fd}}{dt} = R_s i_d + L_{md}\frac{di_d}{dt}, \tag{3.26}$$

$$u_q - \omega_e \psi_d - L_{dq}\frac{di_d}{dt} = R_s i_q + L_q\frac{di_q}{dt}. \tag{3.27}$$

From these equations, the disturbance terms are defined as

$$u_d^{dist} = \omega_e \psi_q - L_{qd}\frac{di_q}{dt} - L_{md}\frac{di_{fd}}{dt}, \tag{3.28}$$

$$u_q^{dist} = -\omega_e \psi_d - L_{dq}\frac{di_d}{dt}. \tag{3.29}$$

The mutual inductances may also be excluded, as they represent a small fraction of the overall disturbance term [7]. These disturbance equations are then decoupled as shown in Figure 3.4. The plant model, denoted as $G_d(s)$ and $G_q(s)$ in Figure 3.4, are given in Equations (3.30) and (3.31).

$$G_d(s) = \frac{\frac{1}{R_s}}{1 + s\frac{L_{md}}{R_s}}, \tag{3.30}$$

$$G_q(s) = \frac{\frac{1}{R_s}}{1 + s\frac{L_q}{R_s}}. \tag{3.31}$$

Three goals are generally favoured when designing a PI controller, namely small overshoot, good damping and a fast response [66]. The modulus optimum (MO) criterion is used as tuning method because of its simplicity and fast response [66, 67] and has been proved to be robust against parameter inaccuracies [11], but any suitable tuning criterion can be used.

The MO criterion is specifically used for systems that are modelled as first order plus dead time (FOPDT) transfer functions, which take the form,

$$G(s) = \frac{K}{(1 + sT)}e^{-\tau s}, \tag{3.32}$$

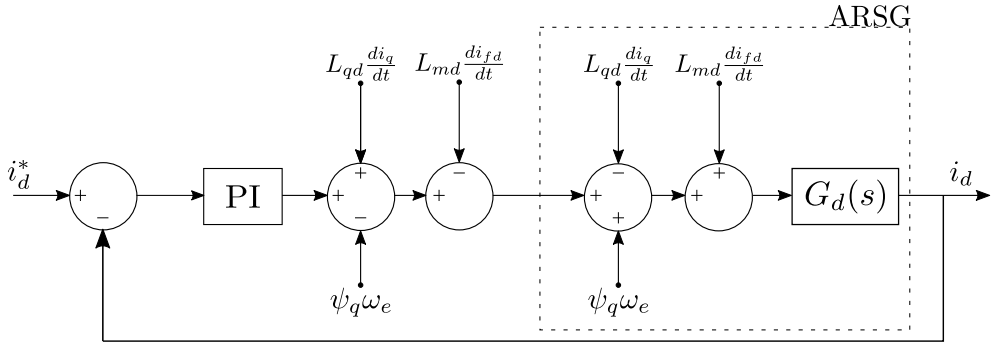

(a) D-axis current control decoupling.

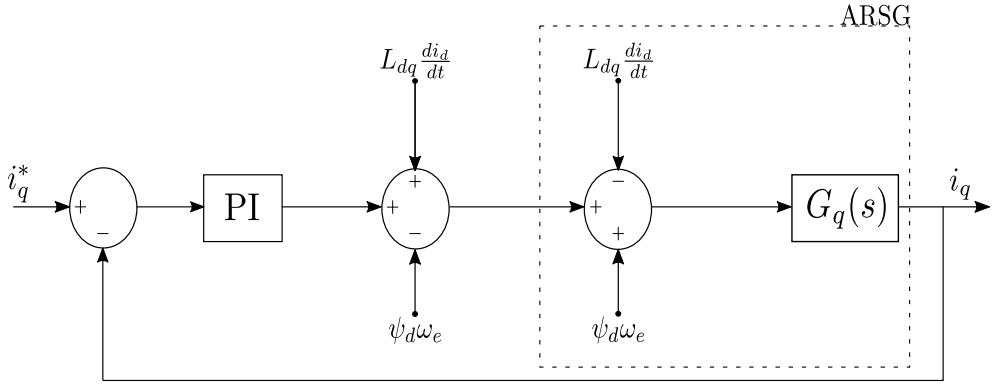

(b) Q-axis current control decoupling.

Figure 3.4: The decoupled dq current controllers.

where τ is the dead time of the system, in this case the switching delay introduced by the VSC. An approximation of the dead time is manipulated into the ARSM plant models, which can now be given as

$$G_s(s) = \frac{\frac{1}{R_s}}{(1+sT_s)(1+sT_{delay})}, \tag{3.33}$$

where $T_s = \frac{L_s}{R_s}$ and the subscript s refers to the stator quantities. The idea behind MO tuning is to compensate for the larger time constant, in this case, the machine's electrical time constant T_s. The PI controller has a general form of

$$D(s) = K_c(1 + \frac{1}{T_i s}), \tag{3.34}$$

where K_c and T_i are defined by the MO criterion as

$$\left.\begin{aligned} K_c &= \frac{T_s}{2T_{delay}K} = \frac{L_s}{2T_{delay}}, \\ T_i &= \quad T_s \quad\quad = \frac{L_s}{R_s}. \end{aligned}\right\} \tag{3.35}$$

Since the time constants of the ARSM are non-linear functions of the stator currents i_s and field current i_f, a fixed estimation of the inductances, L_s, would result in inaccurate placement of the controllers' closed-loop poles. Look-up tables (LUTs) containing the flux linkages and inductances of the ARSM at a wide variety of currents are obtained from the FE model presented in Chapter 2, thus providing a way the current controller gains can be continuously updated on-line. The same method is used to ensure that the disturbance term is also an accurate representation of the ARSM at a given operating point. The LUTs for the flux linkages and inductances are four dimensional by nature, as they represent the change in the ARSM parameters with any variation of i_d, i_q and i_f, i.e., $\psi_s^{LUT}(i_d, i_q, i_f)$ and $L_s^{LUT}(i_d, i_q, i_f)$. A more in-depth discussion of the non-linear mapping is done in Section 3.2.1. The d-axis current controller block diagram implementation is given in Figure 3.5. The structure of the LUT method is given in Figure 3.6

Anti-windup limits

A well known problem with classical controllers that include an integral term is integral windup. This scenario happens when the given set-point cannot be reached due to any limitation placed on the practical system, e.g. the DC-bus link voltage that limits the output voltage of the VSC. A simple method to prevent this is to continuously check if the controllers' output is at or above the saturation limit and then disabling the integrator output, as is shown in Figure 3.5.

Non-linear mapping of the ARSM

The mathematical model of both the ARSM and the PI controllers, require knowledge of the machine parameters, which are highly non-linear. One method to account for this non-linearity is by using the FE model to generate flux linkage maps. By using a FE simulation, the maps account for the affect that saturation and cross-coupling have on the ARSM. The flux maps for $i_f = 0$ and 1 p.u. is shown in Figure 3.7. These flux maps highlights a unique property of the ARSM when connected to the DC-bus link. Since i_f

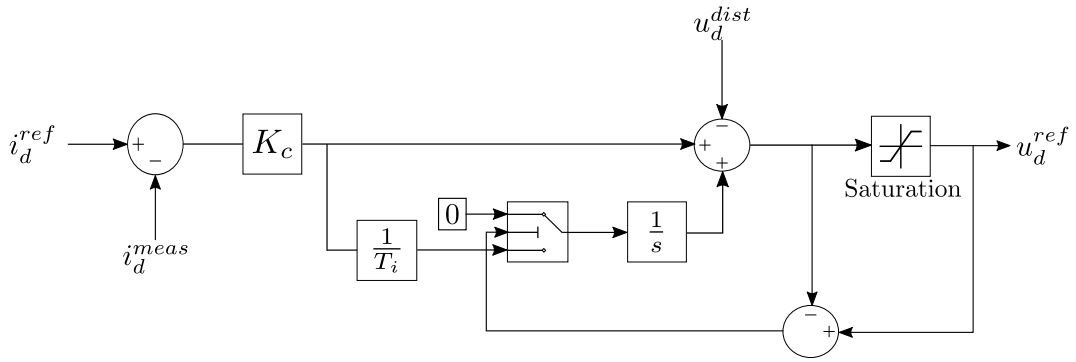

Figure 3.5: D-axis PI controller with anti-windup implementation.

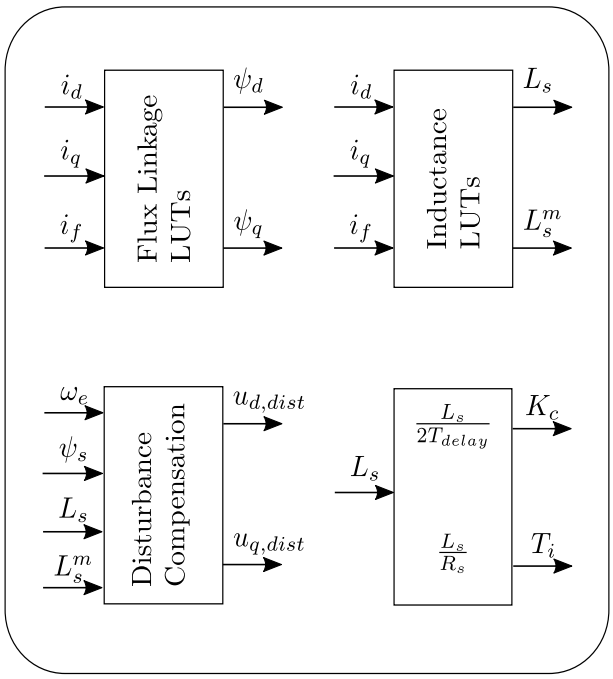

Figure 3.6: The structure of the various LUTs used for the current controllers - superscript m is used to indicate the mutual inductances.

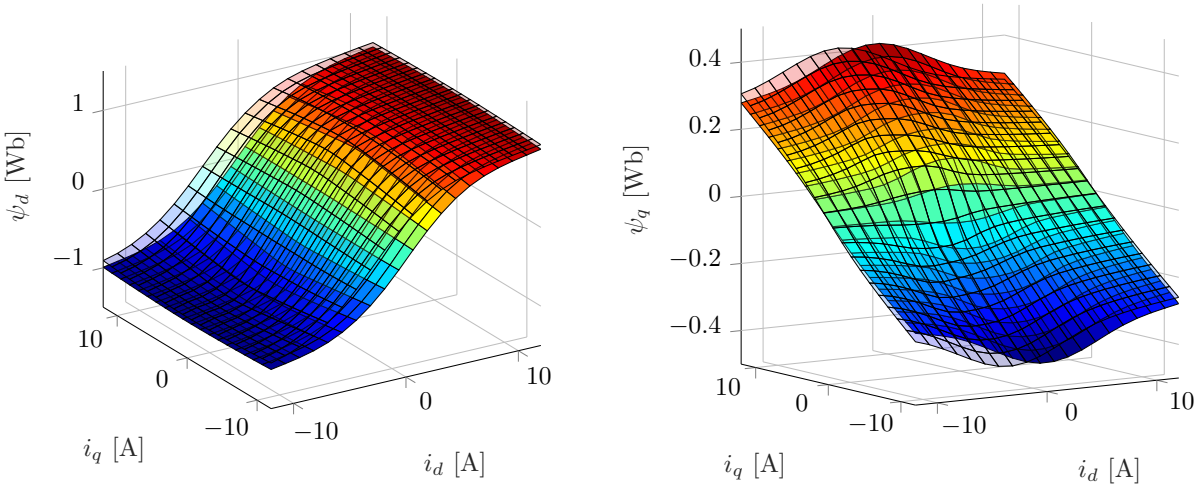

(a) D-axis flux linkage maps

(b) Q-axis flux linkage maps

Figure 3.7: The flux maps of the ARSM at $i_f = 0$ p.u. (opaque) and $i_f = 1$ p.u. (transparent).

flows in different directions depending on whether the machine is operated as a motor or generator, the ARSM has to be operated at a current angle which will ensure that the d-axis flux linkage generated is in the same direction as that of the flux linkage caused by the field current. The ARSM can thus not be arbitrarily operated in any quadrant.

While the plant models given in Equations (3.30) and (3.31) can be used to simulate the ARSM in Simulink, a more elegant method of doing so would be to implement a model based on the equation given in Eq. (3.36). Doing so ensures that the cross-coupling, mutual inductances and the effect of the field current is automatically included in the electrical model. The ARSM block diagram is given in Figure 3.8. The flux linkage maps are interpolated to produce the correct 2D flux maps for the given field current, $\psi_s^{LUT'}$. They are then passed to the 2D inverse interpolation block, the implementation of which is provided by the author of [11]. This block then produces the stator currents of the machine for the applied voltage u_s and field current value.

$$u_s = R_s i_s + \frac{d\psi_s}{dt}. \tag{3.36}$$

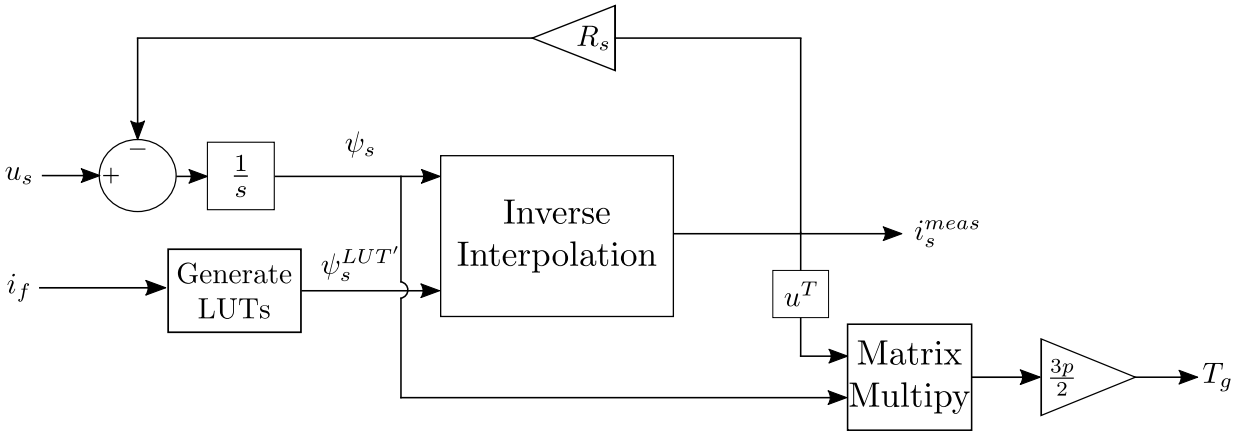

Figure 3.8: Block diagram of the electrical model in Simulink.

3.2.2 Torque control

In the proposed cascaded control structure presented in Figure 3.3, the torque controller supplies the current reference, i_s^{ref}. The controller's objective is to determine an optimum current vector given a torque reference T_{ref}. Since this is an open-loop controller, it can be assumed that T_{ref} is achieved within the time constant of the current controllers. A machine specific output limit must still be imposed to ensure the machine stays within a safe operating range. The focus of this section is on the maximum torque per ampere (MTPA) family of algorithms.

There are several suggested MTPA methods. While linear control methods, such as the one proposed in [57], are simple to design and can be highly effective for machines that have linear characteristics, such a strategy would not consider the non-linearities of the ARSM and would thus perform quite badly. In [59] a MTPA strategy based on a virtual small signal injection and extreme seeking control is suggested. This method is parameter independent and robust against any harmonics in the voltage and current measurements. The disadvantage of this strategy is its complex design and implementation. It also requires a closed-loop torque controller, as the proposed system requires feedback of the dq machine voltages. [68] suggests a similar method, with both methods only implemented for IPMSMs.

The authors of [56] suggest a control strategy based on a FE analysis. This structure relies on two 2D LUTs to provide the d- and q-axis reference currents. As the current references are a function of both the torque reference and the maximum allowable flux linkage, such that $i_s^{ref}(T_{ref}, |\psi_r|_{max})$ and $|\psi_r|_{max}(U_{dc}, \omega_e)$, this control strategy will work for

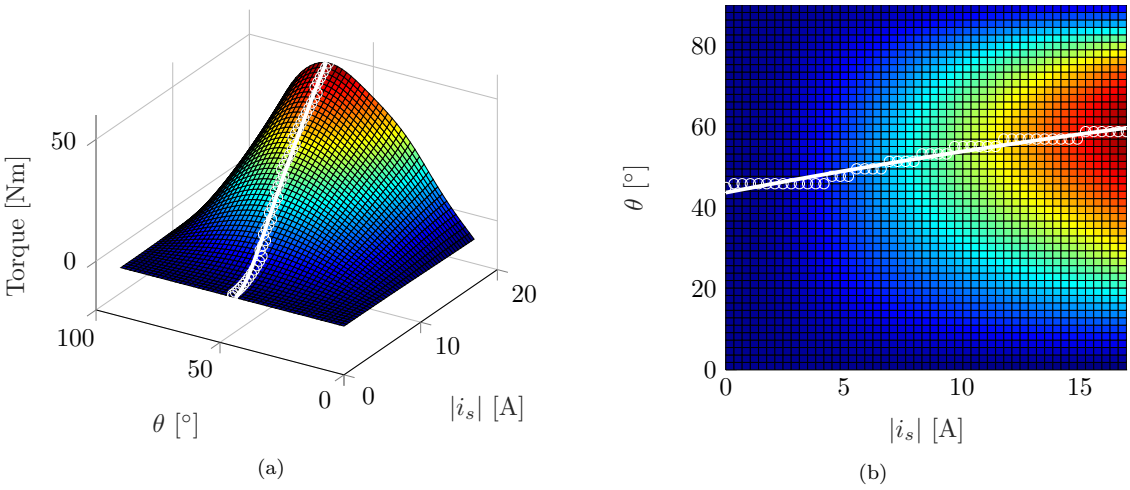

Figure 3.9: The results of the MTPA algorithm for $i_f = 0$ A.

any speed and DC-bus link voltage. Another LUT-based MTPA method is suggested in [11] for constant DC-bus link operation. In this method, two 1D LUTs are used to represent each of the current magnitude and angle references such that $i_s^{ref}(T_{ref})$ and $\theta_{ref}(T_{ref})$. Both these methods are computationally inexpensive, as the LUTs are generated off-line, and both show a good response.

The torque control strategy used for this project is derived from the above mentioned LUT based methods. The torque maps of the ARSM, similar to the flux maps, are a function of the stator and field currents, i.e. $T(i_d, i_q, i_f)$. Evaluating the torque maps of the ARSG at different set values of i_f allows the formulation of a MTPA algorithm, as shown in Figure 3.9 for $i_f = 0$ A.

The algorithm essentially compares each point on a torque map until the lowest current combination is found for a given torque reference. This result forms the MTPA contour for that value of i_f. This is done for a range of field current values, with the MTPA contours from each combined into two 2D LUTs, one for the current magnitude reference and one for the current angle reference. These two LUTs are shown in Figure 3.10, with the block diagram implementation of the controller given in Figure 3.11.

3.2.3 Wind turbine simulation and control

As a wind turbine is a device that converts the energy present in wind pockets into a more useful form, the control of a turbine has an immense effect on the quality and amount

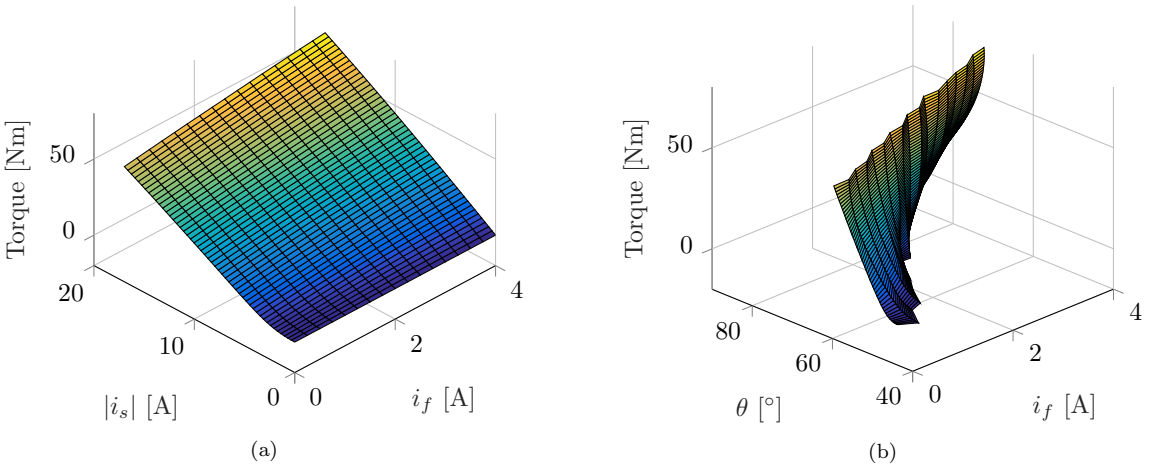

Figure 3.10: The final MTPA LUTs.

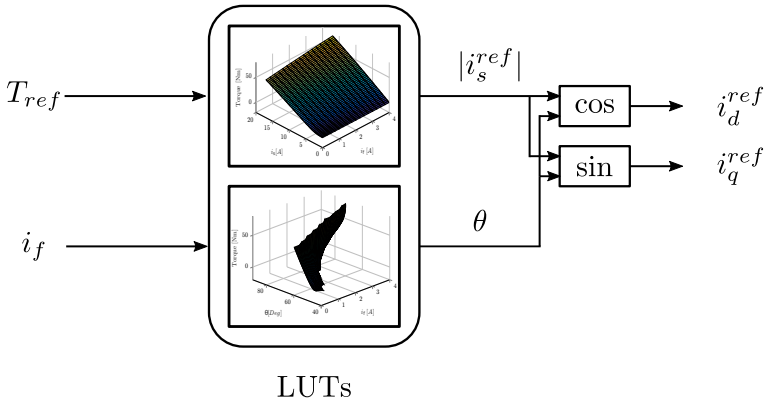

Figure 3.11: The structure of the torque controller.

of power being extracted. It is thus critical that the turbine controller ensures that the turbine is operated at optimal efficiency. This maximum efficiency can be achieved by keeping λ at its optimum value [11], meaning that the efficiency can be indirectly controlled by regulating the TSR. TSR control ordinarily requires knowledge of the wind speed and the blade characteristics, and as such performs well [7]. Measuring the wind speed is problematic in practical systems, however, the need for a wind speed measurement can be avoided by deriving a suitable controller [7, 11]. Depending on the design of the controller and the inner control loops, the output command can either be a speed [7, 69] or torque reference [4] to ensure MPPT of the turbine's C_p and by extension regulate the TSR. Using a speed-controlled MPPT would track the optimal C_p more accurately, but results

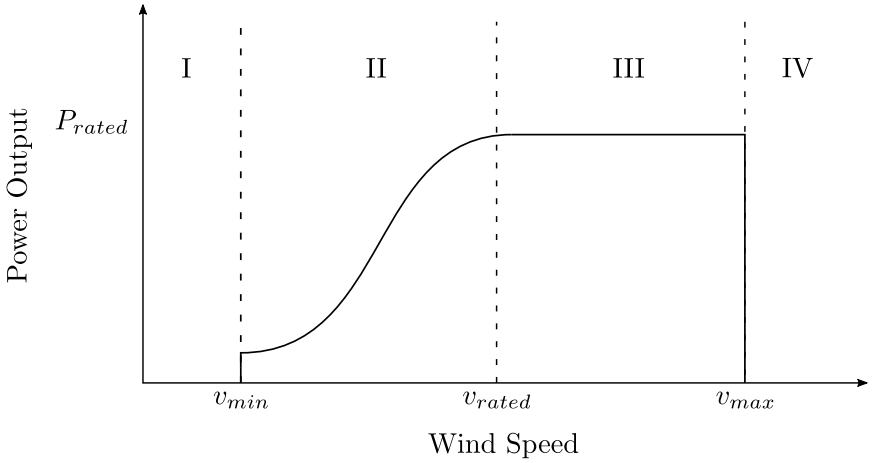

Figure 3.12: The ideal power curve of a variable speed turbine.

in more variations of the rotor speed and drivetrain torque. The torque-controlled MPPT algorithm results in less extreme variations in torque and speed, but does have a lower power tracking performance [7].

Within this overall control objective, there are smaller directives, depending on the region of operation. An illustration of the different operating regions is shown in the power versus wind speed curve given in Figure 3.12.

Four operating regions are defined on this curve. Region I consists of wind speeds which are below v_{min}, where it is economically inefficient to run the turbine. The turbine is allowed to turn freely, and no power is generated. The speed is observed until the wind speed rises above v_{min} and thus enters into the second operating region.

Region II consists of wind speeds between v_{min} and v_{rated}. During this time, the generator is operated under MPPT by tracking the optimum C_p value. This region is also known as the maximum power region.

Region III, or the constant power region, occurs during wind speeds between v_{rated} and v_{max}. During this region, the controller adjusts the operating point to ensure the generated power remains at its rated value. This is done by soft, or passive, stalling [11] and involves either decreasing λ to reduce the lift on the blades or by increasing λ, such that the blades will stall through turbulence.

Region IV occurs during extremely high wind speeds where the turbine can no longer be controlled safely. The turbine should be actively shut down, to avoid any mechanical or electrical damage to the turbine and generator.

As the control for Regions I and IV are relatively straightforward, only Regions II and III are considered for this project.

Wind Turbine Controller

Rearranging Eq. (1.3) as shown in Eq. (3.37) and substituting it into the original wind power equation, one arrives at the power equation given in Eq. (3.38). The power equation is now only dependent on λ, C_p and ω_t, where $\omega_t = \frac{\omega_m}{n_g}$.

$$v_w = \frac{r_b \omega_t}{\lambda}, \tag{3.37}$$

$$P_w = \frac{1}{2}\rho A C_p(\lambda)(\frac{r_b \omega_t}{\lambda})^3. \tag{3.38}$$

Dividing by ω_t and substituting $A = \pi r_b^2$, the turbine torque can be written as

$$T_w = \frac{1}{2}\frac{\rho \pi r_b^5 C_p(\lambda)}{\lambda^3}\omega_t^2. \tag{3.39}$$

From Eq. (3.39), the control law for region II can be stated as

$$T_{g,ref} = k_{opt}\omega_m^2, \tag{3.40}$$

where k_{opt} is a fixed optimal value based on the optimum values of C_p and λ as defined in Eq. (3.41).

$$k_{opt} = \frac{1}{2}\frac{\rho \pi r_b^5 C_p^{opt}}{n_g^3 \lambda_{opt}^3}, \tag{3.41}$$

with $C_p^{opt} = C_p(\lambda_{opt})$. When operating in Region III, the control law can be stated as [4],

$$T_{g,ref} = \frac{P_{max}}{\omega_m}. \tag{3.42}$$

By choosing Eq. (3.42) as the control directive for this region, the rotor speed is allowed to increase to stall the blades through turbulence. This allows the turbine to operate in Region III for higher speeds and longer periods without overloading the generator. A second option, decreasing the rotor speed, would keep the rotor at safe speeds, but can overload the generator at high wind speeds. Equations (3.40) and (3.42) presents two

different controllers for the respective regions, with a seamless transition between them being preferred. A solution, proposed in [4], is to rewrite the control law as

$$T_{g,ref} = \frac{P_{ref}}{\omega_m}, \tag{3.43}$$

where P_{ref} is defined as,

$$P_{ref} = \begin{cases} k_{opt}\omega_m^3 & : P_{ref} \leq P_{max} \\ P_{max} & : P_{ref} > P_{max} \end{cases} \tag{3.44}$$

If the damping factor of the system is known, it can be used to compensate for the damping torque acting on the turbine in Region II, i.e. $P_{ref} = k_{opt}\omega_m^3 - B_{tot}\omega_m^2$ [4]. This term is generally small enough to be negligible [62,69]. The final turbine controller is shown in Figure 3.13.

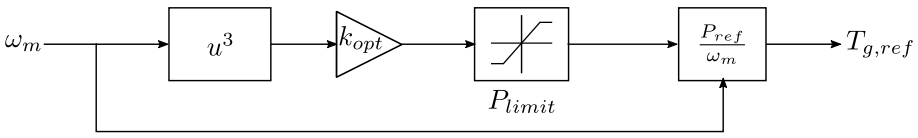

Figure 3.13: The block diagram implementation of the turbine controller.

To properly test the designed control systems, the behaviour of a wind turbine needs to be simulated. A static step response model will not capture realistic turbine behaviour. It is thus necessary to emulate the behaviour of a wind turbine and wind conditions. The following subsections discuss the three subsystems needed for such a simulation.

Wind speed generator

Wind speed input data can either be real or synthetic data, but the controlled conditions of synthetic data are preferred for testing control systems [7, 11]. The equation used for the generation of wind speed data is given by

$$v_w = V_o + v_t, \tag{3.45}$$

where V_o is the mean wind speed and v_t is the turbulence component. The turbulence is generated by applying a filter with the correct power spectrum, such as the Kaimal [7, 70] and von Karman models [71]. The von Karman model is chosen for this project, with the

correct frequency distribution being achieved by passing white noise through the transfer function given in [71] as

$$W(s) = K_F \frac{(m_1 T_F s + 1)}{(T_F s + 1)(m_2 T_F s + 1)}. \tag{3.46}$$

In Eq. (3.46), K_F and T_F are the gain and time constant related to the filter. The time constant is related to turbulence length scale, L, and the mean wind speed V_o by

$$T_F = \frac{L}{V_o}. \tag{3.47}$$

The turbulence length scale is typically considered as the length of the eddies in the free stream. An approximation is given in [71] reflecting

$$L = 6.5h, \tag{3.48}$$

where h is the height of the tower. K_F can be given as

$$K_F = \sqrt{\left(\frac{2\pi}{11.1}\right)\left(\frac{T_F}{0.04}\right)}. \tag{3.49}$$

The block diagram implementation is shown in Figure 3.14. The scaling factor σ_u is to ensure the amplitude of the turbulence is scaled to the correct intensity, given the terrain. σ_u is given as

$$\sigma_u = k_\sigma V_o, \tag{3.50}$$

where k_σ is the turbulence factor, which is dependant on the terrain conditions. Relatively open sites have k_σ values of ≈ 0.189 [71]. An example of a wind speed data set generated using Figure 3.14 is shown in Figure 3.15.

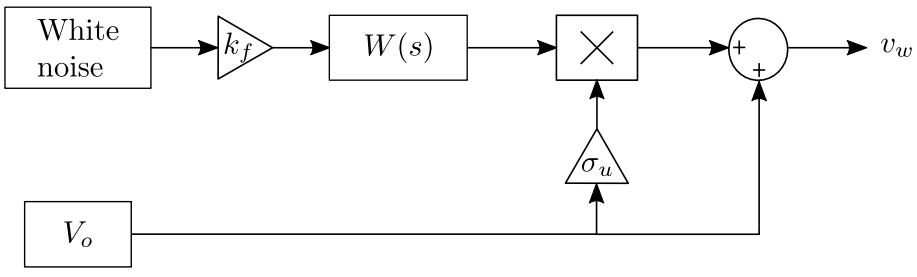

Figure 3.14: Schematic representation of the wind speed model.

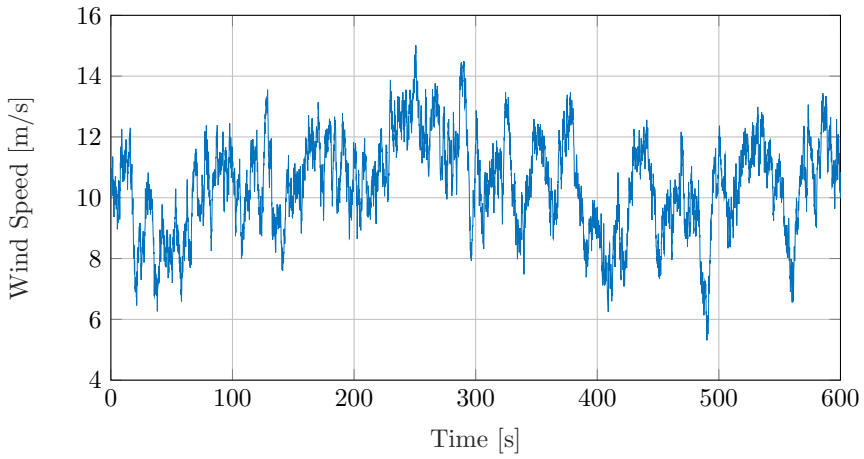

Figure 3.15: An example of a generated wind speed time series.

Turbine aerodynamics

This subsystem simulates the interaction between the turbine blades and the wind, providing aerodynamic torque T_w experienced at the hub, using Eq. (3.51). This is a simplified simulation of the interaction between the wind and the blades, as the wind shear effect, tower shadow effect and the smooth effect are ignored. Eq. (1.3) is used to determine λ. The resulting subsystem is shown in Figure 3.16.

$$T_w = \frac{\pi \rho r_b^2 v_w^3 C_p(\lambda)}{2\omega_t}. \tag{3.51}$$

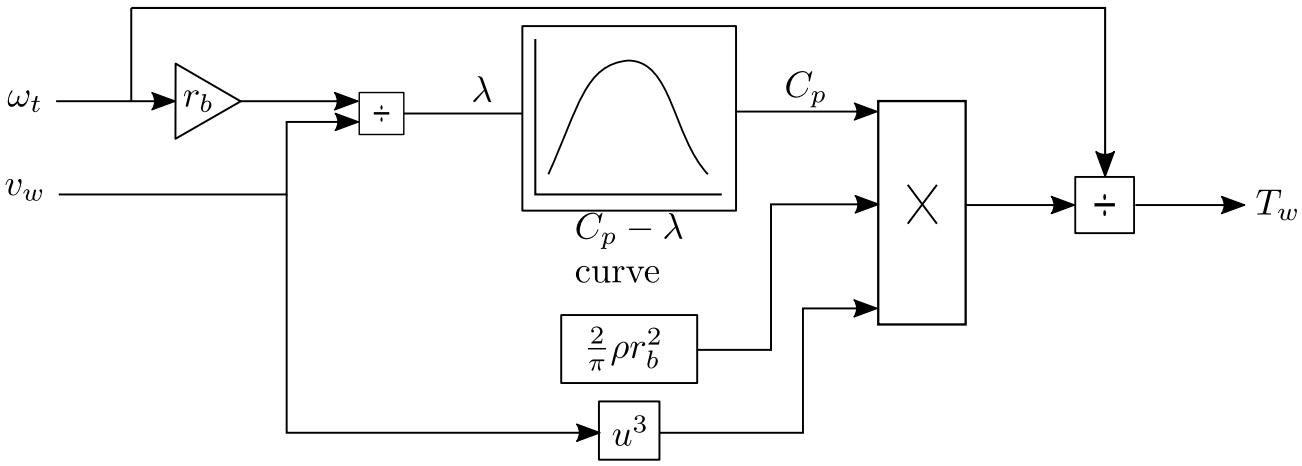

Figure 3.16: Aerodynamic torque simulator.

Drive train

The drive train subsystem contains the mechanical dynamics of the turbine in a two-mass system, as explained in Section 1.1.2. The resulting block diagram is shown in Figure 3.17.

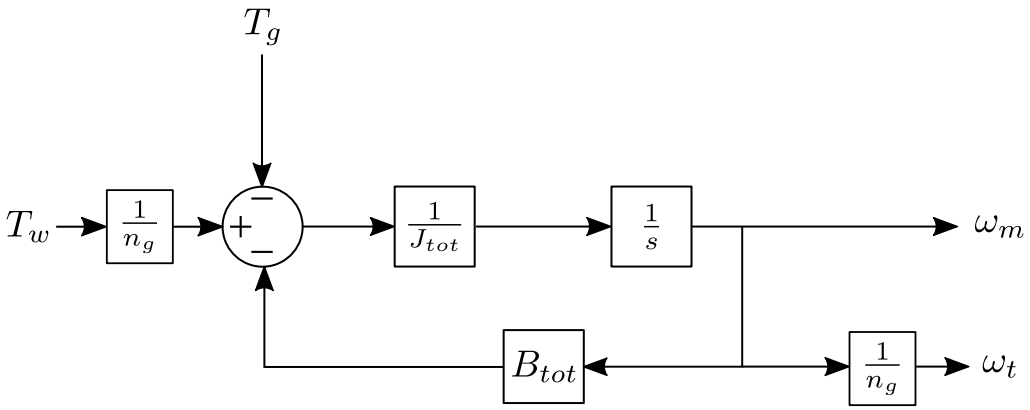

Figure 3.17: Block diagram of the turbine's drive train.

Chapter 4

Simulation and Measured Results

In this chapter, a comparison of the simulated and measured results for the generator and control systems designed in Chapters 2 and 3 are given.

An overview of the test bench is presented first, after which the generator design results are discussed, with comments given on the assembly of the rotor. The measured torque, power factor, and efficiency curves are presented, with the FE results given alongside for comparison. The results are discussed, with tables that provide a direct comparison of the measured and simulated values at certain chosen operating points.

The ARSG current and torque controllers are then presented. The step response of the simulated and measured system is given, then a comparison of the torque maps used for the MTPA control are presented and discussed. The performance of the torque control algorithm is assessed, with the results of the wind turbine controller indicated at the end.

4.1 Test bench

The test bench used in the laboratory comprised of a 22 kW induction machine, coupled to the ARSG through a step-down gearbox with a gear ratio of 2.6. The rapid prototyping system indicated in Figure 4.1 is Linux-based with the real-time applications interface (RTAI) kernel module installed. This system, called the Pentium System, runs on a 1.5Ghz Pentium processor that communicates with a custom-built FPGA board. This FPGA transmits the various control signals through inverters boards towards the VSCs. The system has six PWM output ports, allowing it to control two machines at the same time.

The inverter boards also provide channels from which measurements can be taken. The machine currents, DC-bus voltage, field current LEM sensor and the torque sensor are connected to the inverter boards. An encoder can be connected to the Pentium System through a digital-to-analogue converter (DAC) board, providing a way to measure the mechanical rotor angle.

The BTB VSCs used in this project are provided by SEW-EURODRIVE. They provide automatic current protection and correct dead-time switching. The VSCs are specially made for the Electrical Machines Lab and are connected directly to the Pentium System. The external DC voltage source shown in Figure 4.1 is used to test the controllers and measure the ARSM's performance at set values of i_f.

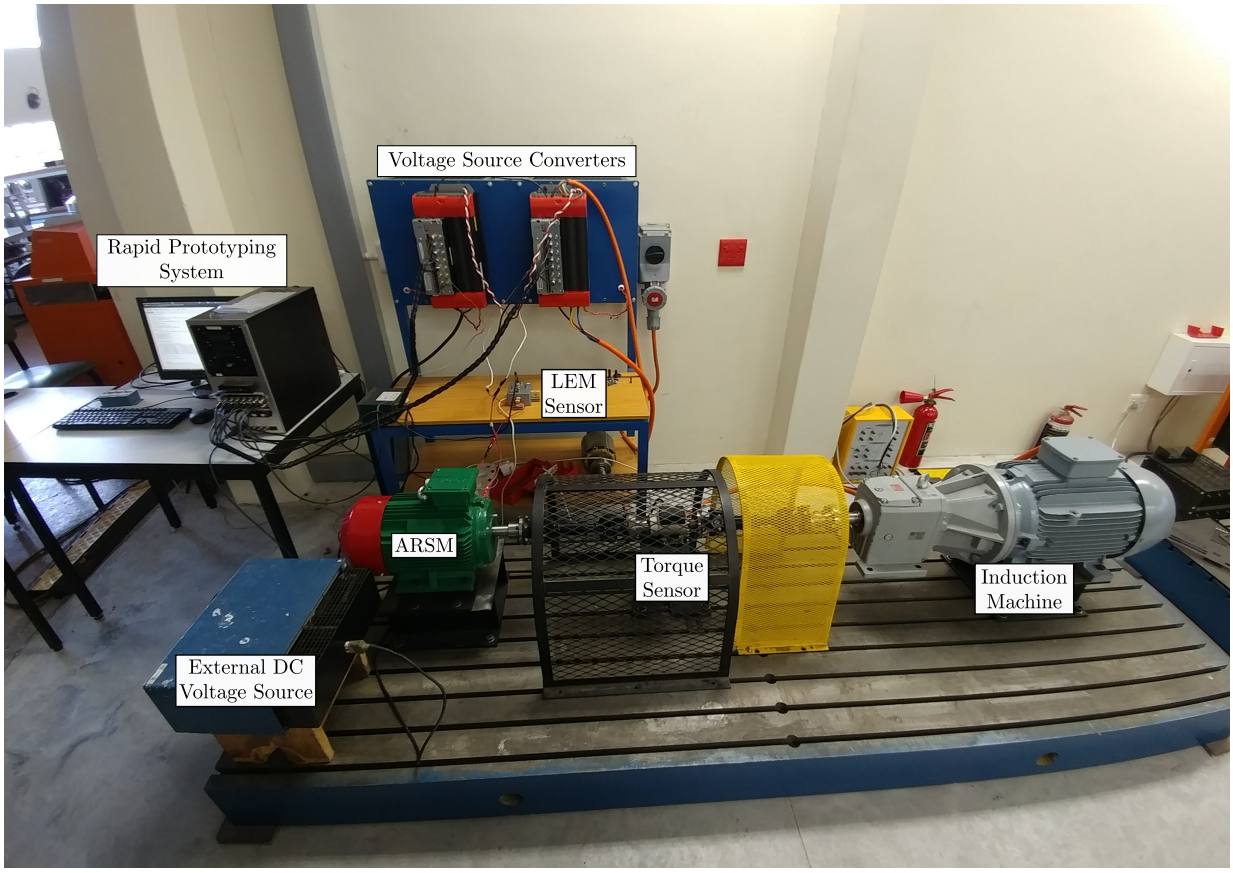

Figure 4.1: The practical assembly.

4.2 Generator design results

4.2.1 Assembly and manufacturing

The rotor of the ARSM is shown in Figure 4.2. A lamination thickness of 0.5 mm is used and assuming a unity stacking factor, the rotor would require 230 laminations. The actual number of laminations used to achieve the stack length of 115 mm were 220, resulting in a stacking factor of 0.96.

The ribs of the slot opening proved to be to thin, as they were easily bent out of shape or broken. This was also evident during the winding of the rotor, as the slot ribs made it difficult to wind the rotor without damaging them. The rotor slot, because of the unconventional shape, also necessitated that a thinner 0.9 mm wire be used. This leads to an increase in the resistance of the field coil, which has a measured value of 6.5 Ω. This measurement includes the resistance of the brushes, which are 0.3 Ω each. This also means

(a) The finished stack of the ARSG.

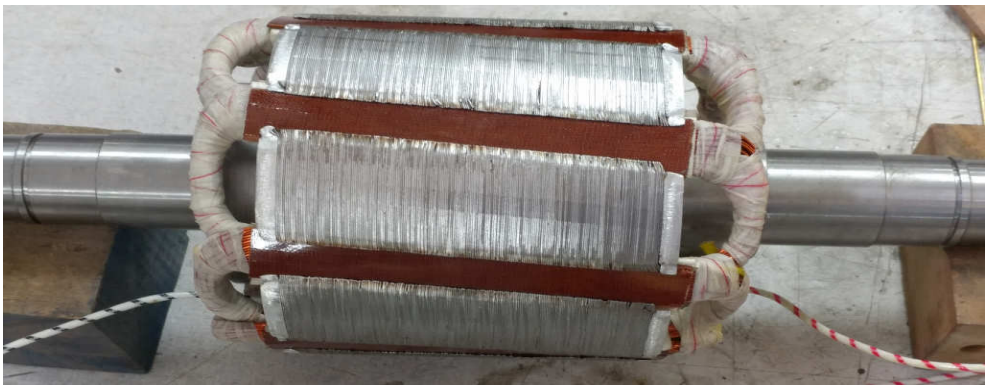

(b) Complete ARSG rotor.

Figure 4.2: The rotor before and after winding.

Table 4.1: A comparison between the simulated and practical ARSM.

	FE Model	Real ARSM
z_f	150	140
w_d	1.2	0.9
R_f	5.0	6.5

z_f - Field Winding Turns; w_d - wire diameter; R_f - Field winding resistance

that the field winding has a lower fill factor than assumed in the FE model.

To avoid having to make extensive modifications to the existing shaft and stator casing, the slip rings are placed on either side of the rotor. This allows use of the same shaft that the induction motor uses, with the only modification to the casing being the cuts at the front and back, which allows for the installation of the brushes. The slip ring placement and modifications to the stator casing are shown in Figure 4.3 and some of the practical comparisons given in Table 4.1.

4.2.2 Measured results

Table 4.2 provides a direct comparison between the FE and measured results for $I_f = 0$ and 1 p.u., with the rated field current being 2.5 A. The FE efficiency shown in this comparison includes the measured friction losses, shown in Figure 4.4, and uses the measured value of R_f in the calculation of $P_{r,cu}$, to provide a more accurate comparison. The current angle is held constant at 50°and 70°for the respective field current values.

To provide a better overview of the ARSG's performance, the torque, efficiency and power factor are measured over a range of field current angles. A side-by-side comparison with the simulated results is presented in Figures 4.5 to 4.7. For this comparison, the measured stator and field current are used in the FE model. Measurements are taken at $I_f = 0$, 1, 2 and 3 A, with the stator current adjusted to ensure that the peak measured torque does not exceed 20 Nm. This torque limit is chosen because it provides a baseline torque that the machine can reach regardless of the field current. The particular field current values are specifically chosen as they effectively demonstrate the effect that the rotor winding has in a wide variety of conditions, i.e., a low field current, a field current

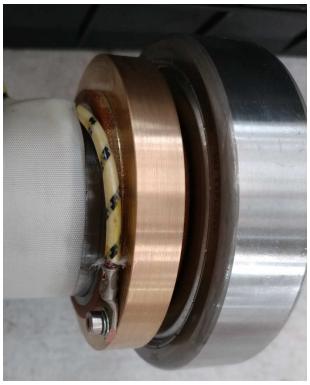

(a) The right slip ring

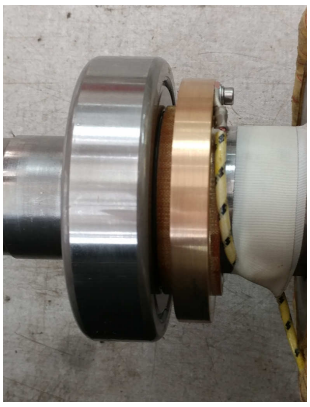

(b) The left slip ring

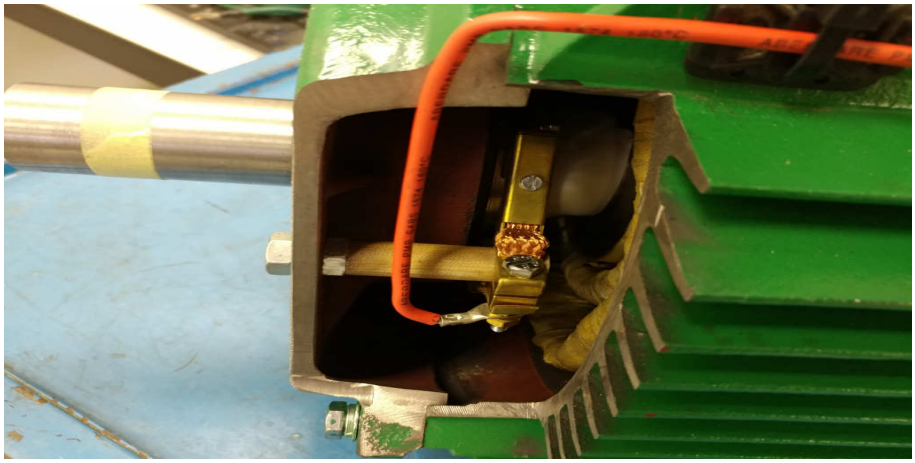

(c) The left slip ring and brush inside the stator

Figure 4.3: The modifications to the stator casing to accommodate the slip rings.

Table 4.2: A comparison between the FE and the practical ARSGs.

	$I_f = 0$ p.u.		$I_f = 1$ p.u.		Unit
	FE Values	Measured Values	FE Values	Measured Values	
T_g	21.5	19.5	22	22	[Nm]
T_r	12.5	8.1	9.9	9	[%]
PF	0.44	0.3	0.73	0.51	[]
Eff	82.9	76	86.1	82	[%]
I_s	5.64	5.64	3.4	3.75	[A]

T_g - Torque; T_r - Torque Ripple; PF - Power Factor; Eff - Efficiency; I_s - RMS Stator Current;

just below and a field current just above the rated.

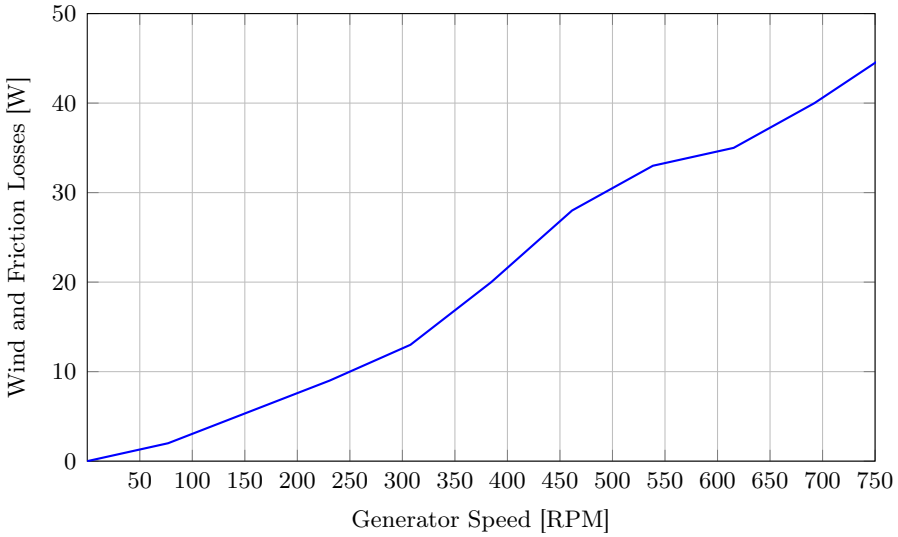

Figure 4.4: Wind and friction losses vs speed.

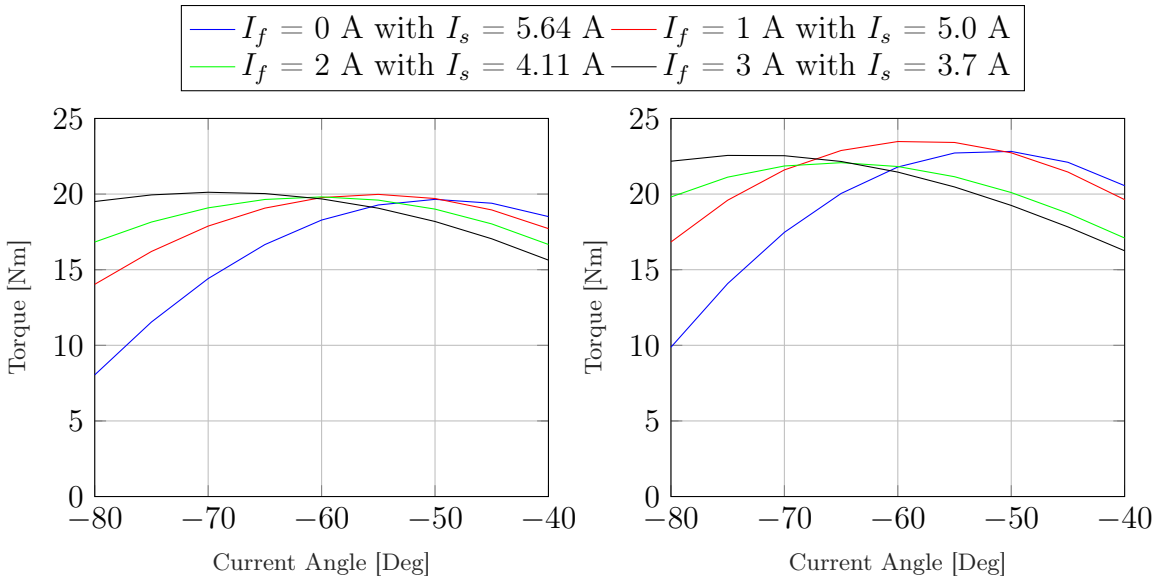

Figure 4.5: The torque curves for the ARSG at 20 Nm. The figure on the left shows the measured torque, and the figure on the right shows the simulated torque at the same stator and field current.

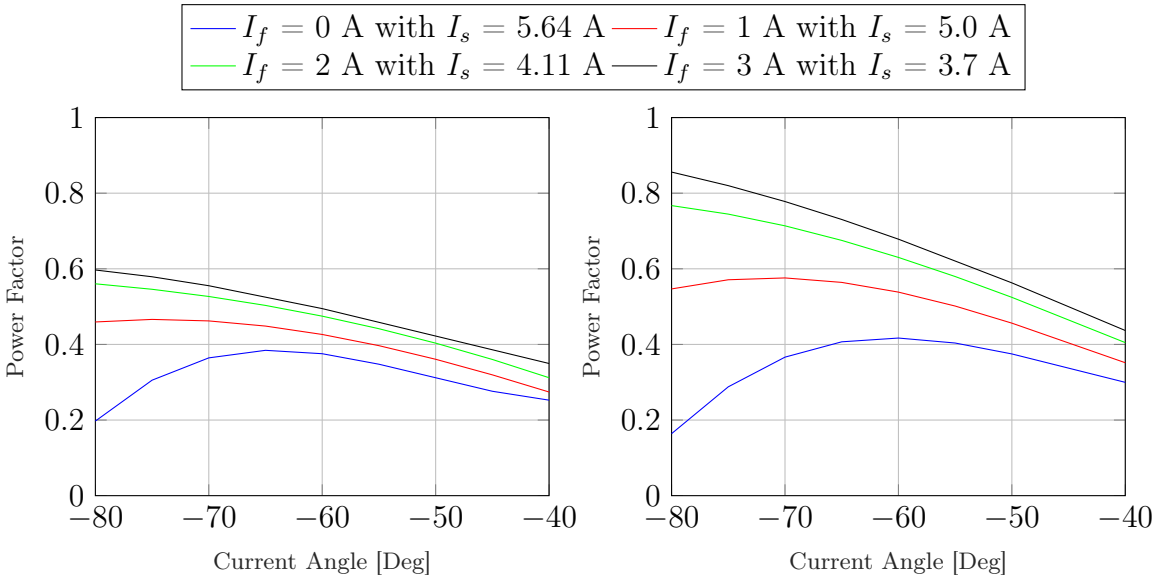

Figure 4.6: The power factor curves for the ARSG at 20 Nm. The figure on the left shows the power factor calculated from measured values, and the figure on the right shows the power factor calculated from simulated values at the same stator and field current.

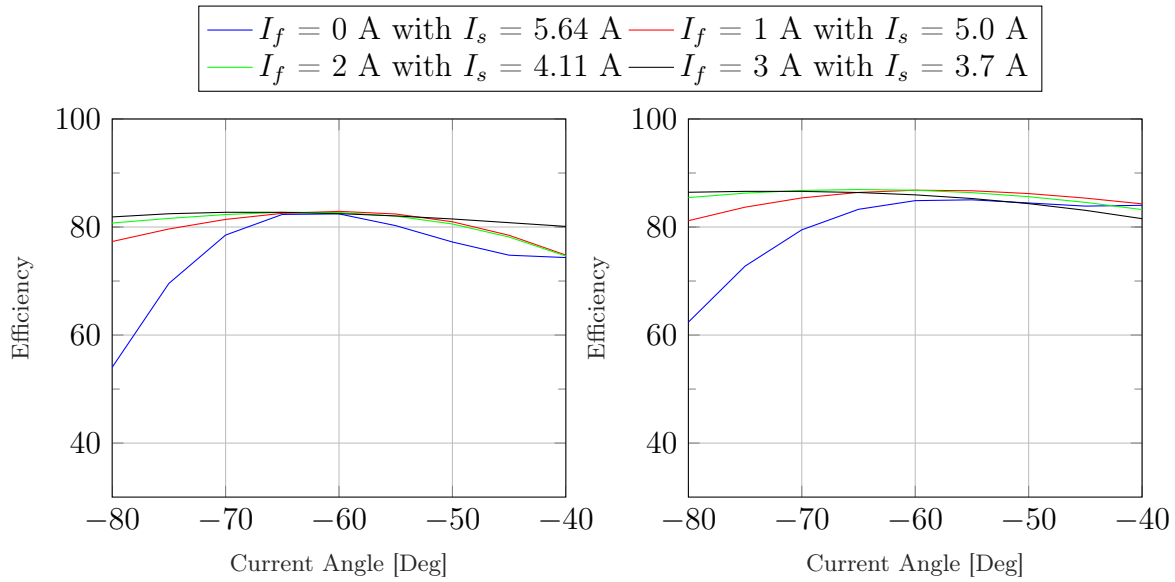

Figure 4.7: The efficiency curves for the ARSG at 20 Nm. The figure on the left shows the measured efficiency, and the figure on the right shows the simulated efficiency at the same stator and field current.

The biggest discrepancy between the torque curves appears at $I_f = 1$ A, with a difference in peak values of 4 Nm. The peak values also occur at different current angles i.e., -50°for the measured peak and -59°for the simulated peak.

The power factor comparison reveals a noticeable difference between the measured and simulated values. While the curves for $I_f = 0$ A match closely, their peak values also occur at different current angles. There is an almost 5°difference between the two, with the peak values differing with 0.05. The bigger discrepancy lies at the higher values of the field current. While the same shift in the current angle at which the peak value occurs is not apparent, the difference between the peak values are substantial. The biggest difference occurs at a field current of 3 A, where the simulated values are higher than the measured value by a value of 0.22.

The efficiency results shown in Figure 4.7 match closer to the FE simulation than that of the power factor. Though the shift in the current angle is still visible, the difference between the peak values are not overly large, with the biggest difference being five percent.

The error between the simulated and measured results can be attributed to several assumptions being made during the FE modelling of the ARSG. The B-H curve in SEMFEM is interpolated, and as such does not match the real B-H curve of the material. The FE model of the generator also did not account for the rotor losses due to magnetic hysteresis, eddy currents and the core losses are just an approximation. The assumption that both the stator and rotor materials are the same cannot be verified, and as such, the stator lamination could be of a different material, which would also lead to inaccuracies in the model. The effect that the field current has on the rotor and stator core losses and eddy currents is also not accounted for. Combined with this, the effect of the manufacturing and winding of the rotor could result in the major discrepancy seen in the power factor results. This omission seems to match with the measured results, as the discrepancy between the measured and simulated power factor increases as the field current increases.

The effect of saturation would mean that the generated torque would be less than predicted, as the above tests are done at rated conditions. In Section 4.3.2, it is shown that the torque discrepancy decreases as the generator is operated at below rated conditions. Note also that the limited performance gain between $I_f = 2$ and $I_f = 3$ A, i.e., for values just below and just above the rated field current. This seems to suggest that a proper optimisation would result in a lower rated field current.

One of the big advantages of the ARSG can be seen in the efficiency plots, as the

presence of the field current keeps the efficiency constant over the range of current angles. Take, for example, the blue curves in the above results. If the ARSG is operated on the basis of MTPA, then it is likely to operate at around -50°. This would mean that the generator would be operating at 75 percent efficiency, instead of its optimum, which is closer to 83 percent. Following the same thought process for the ARSG when operated at I_f = 3 A and θ = -70°, the generator will then be at optimum torque and efficiency.

Another advantage that can be gleaned from these results, is that the machine can be controlled by maximum power factor per ampere (MPFPA) without sacrificing torque and efficiency performance. When operating as an RSG under MPFPA, the optimum current angle would be -65°. At this angle, the torque generated would be 16 Nm, about 4 Nm less than optimum. Operating as a ARSG under MPFPA control would see the generator at a current angle of -80°, where the torque generated would be 19.5 Nm, only 0.5 Nm less than optimum.

To demonstrate the effect the field winding has in a wind turbine set up, consider the general speed curve provided in Figure 4.8. On the curve, four points are indicated at which the generator drive will be evaluated under both RSG and ARSG operation. This test is only done for the practical machine and the results should not be compared to the FE results in Chapter 2. The tests are also done under MTPA control, and as such the power factor and efficiency might be lower than could be achieved otherwise. The measured results at the operating points for RSG operation are given in Table 4.3 and for ARSG operation in Table 4.4.

Under RSG operation, the generator performs rather poorly, especially when considering the power factor of the generator. The efficiency is also extremely low, especially at

Table 4.3: Results of RSG operation at the chosen evaluation points.

Evaluation Point	Power [W]	i_f [A]	i_s [A]	Current Angle [°]	Power Factor []	Efficiency [%]
1	50.7	0	2.3	-50	0.213	45
2	520	0	4.8	-48.8	0.204	47
3	1000	0	5.2	-48.2	0.283	63
4	1600	0	5.64	-47.91	0.324	73.75

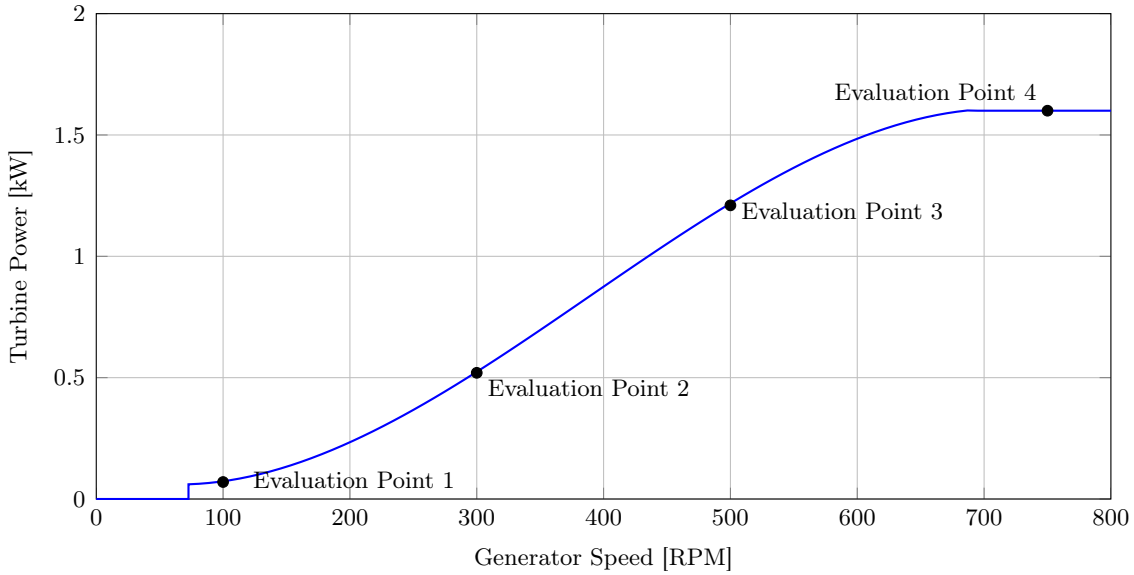

Figure 4.8: A general power-speed curve with four evaluation points.

Table 4.4: Results of ARSG operation at the chosen evaluation points.

Evaluation Point	Power [W]	i_f [A]	i_s [A]	Current Angle [°]	Power Factor []	Efficiency [%]
1	50.7	0.07	2.2	-50.4	0.222	45
2	520	0.767	4.4	-52	0.241	51
3	1000	1.5	4.2	-55	0.434	76
4	1600	2.41	3.8	-64.1	0.5	84

the start of the curve.

When comparing the results from the table with the field current, the performance of the generators at the start of the curve is nearly identical. As the speed and power increases, the performance of the generator improves above that of the RSG. The power factor increases to 0.5, an improvement of 35 percent, and the efficiency rises to 84 percent, an increase of 10 percent of that of the RSG.

4.3 Control system results

This section provides the comparison between the theoretical and measured performance of the developed control systems. The current controller will be presented first, after which the torque control is discussed. A comparison between the torque maps obtained from SEMFEM and the measured torque maps is done, with the results from the torque controller given last. The tests for the current controller are done with an external power supply supplying the field winding. The power supply is used to test both the current controller and the torque controller at certain field current values.

After the preliminary tests are done, the field circuit of the generator is connected to the DC link. The first test done is to show a comparison between the calculated field current used in Simulink and the measured field current. This same test also shows the torque controller and, by extension, the current controller work under dynamic conditions. Finally, the wind turbine controller results are given and discussed.

4.3.1 Current Control

The performance of the adaptive gain current controller is shown and discussed in this section. The controllers are tested at rated speed and for values of $i_f = 0$ and 2.5 A. For both intervals, the controllers are tested with and without the disturbance compensations terms, as well as with the disturbance compensation term filtered and a reduced gains controller. The controllers are also tested for other values of i_f, nonetheless they are not shown here to restrict the length of the document.

The simulated current controller response is shown in Figure 4.9. As the model used in Simulink does not include a VSC model, and both the controller and generator model rely on the same flux maps, the simulated response appears ideal. The d- and q-axis controllers both have settling times 3 ms.

The measured current controller response for $i_f = 0$ A is shown in Figure 4.10. The d-axis controller has a good response with and without the compensation terms, although the aggressive nature of the MO tuning criteria causes a small amount of oscillation around the desired set points. The q-axis controller behaviour is similar to that of the d-axis controller for the first two tests. The controllers' responses with the disturbance term filtered at 500 Hz in Section 4.3.1 show improved performance, with the d-axis showing less oscillation at

the 0 A set point. To determine if a smoother response can be achieved, the gains produced by MO tuning are reduced. The results, shown in Section 4.3.1, demonstrate a smoother response for both axes, but has a slower settling time.

The results obtained at the other set field current values are shown in Figure 4.11. Only the responses for the filtered compensation term and reduced gain tests are presented.The controller performance increases as the field current increases, with the response time of the reduced gain controller decreasing, and the overshoot disappearing.

From the results presented in Section 4.2.2, it can be inferred that there is a discrepancy between the FE generated flux linkage data and the actual flux linkage of the ARSM. In [11], a comparison between the measured flux map and the FE flux map, obtained for a generator of the same material type, shows that this error can be as significant as 0.15 Wb and 0.1 Wb for the d- and q-axis flux linkages, respectively. As this controller requires the

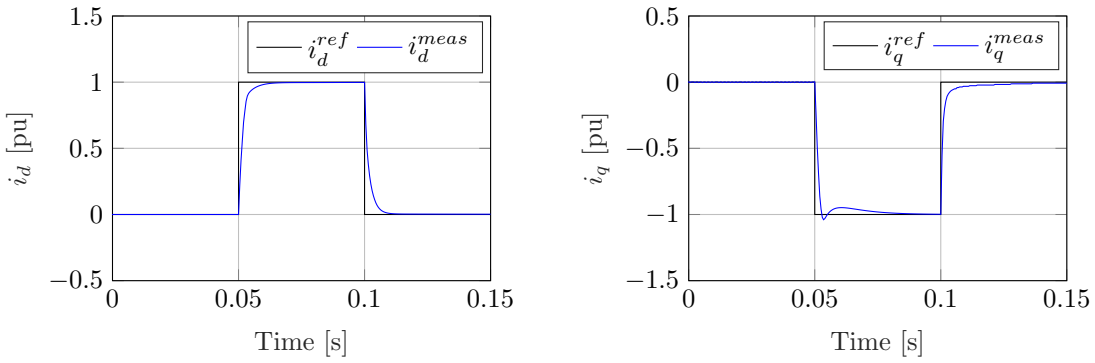

(a) Response for $i_f = 0$ A.

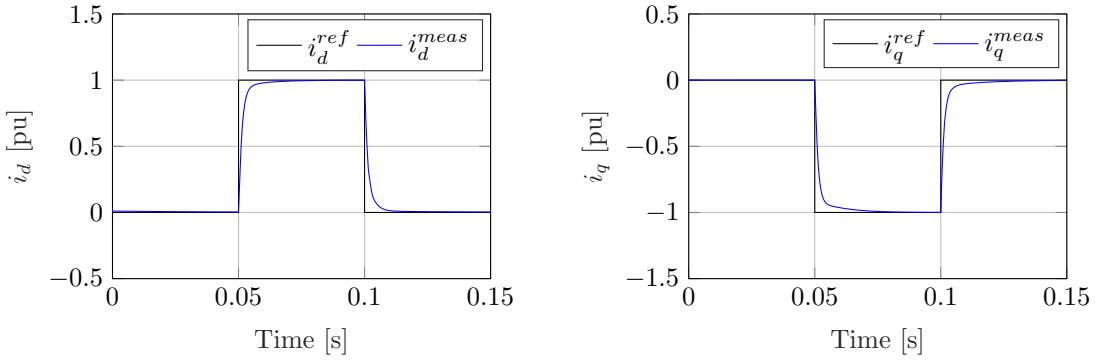

(b) Response for $i_f = 2.5$ A.

Figure 4.9: The simulated response of the current controllers for field current values of 0 and 2.5 A at rated speed.

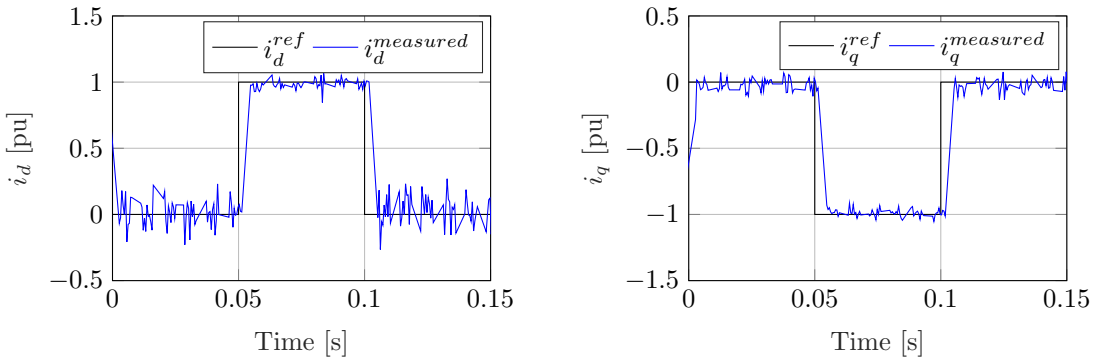

(a) Measured response without a compensation term.

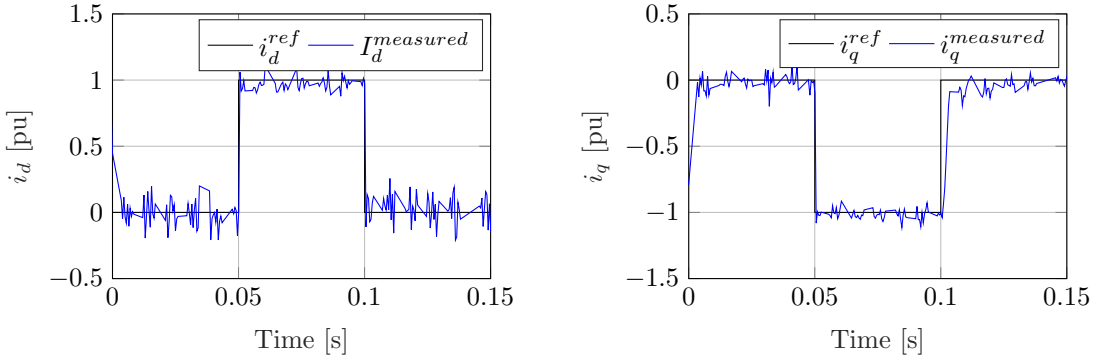

(b) Measured response with a compensation term.

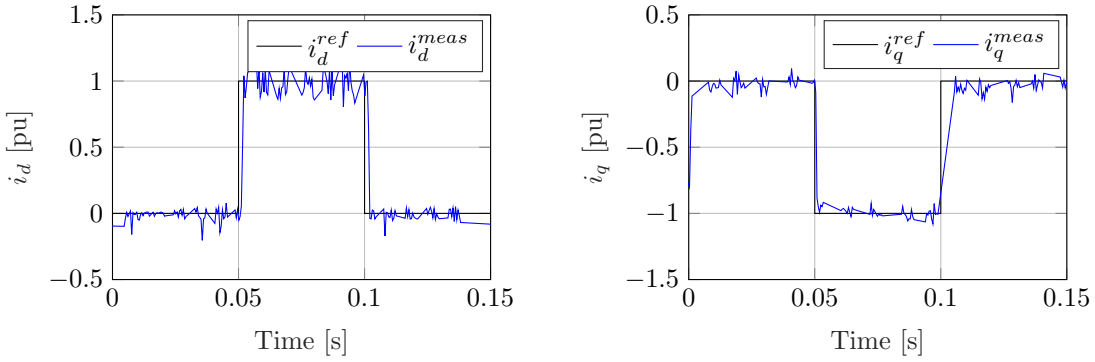

(c) Measured response with a compensation term filtered at 500 Hz.

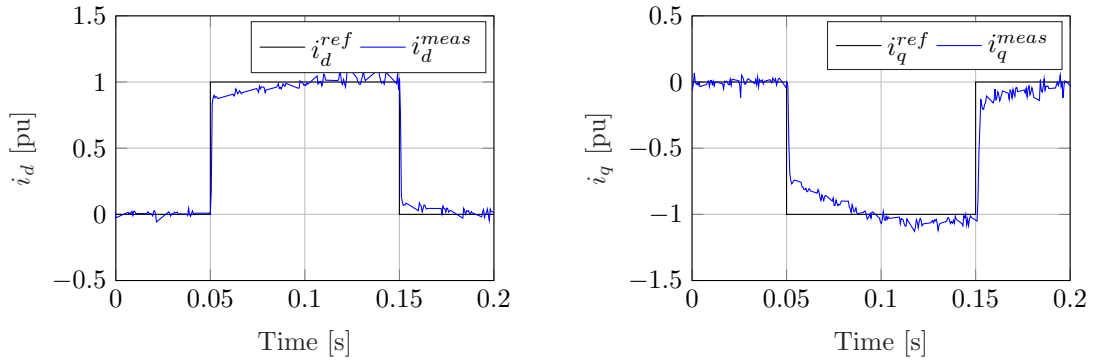

(d) Measured response with reduced controller gains.

Figure 4.10: The measured current controller response for $i_f = 0$ A under different conditions.

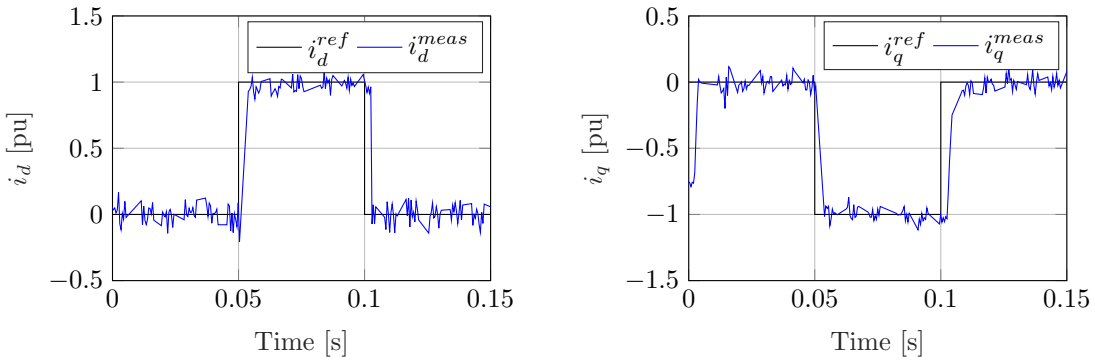

(a) Measured response with filtered compensation term.

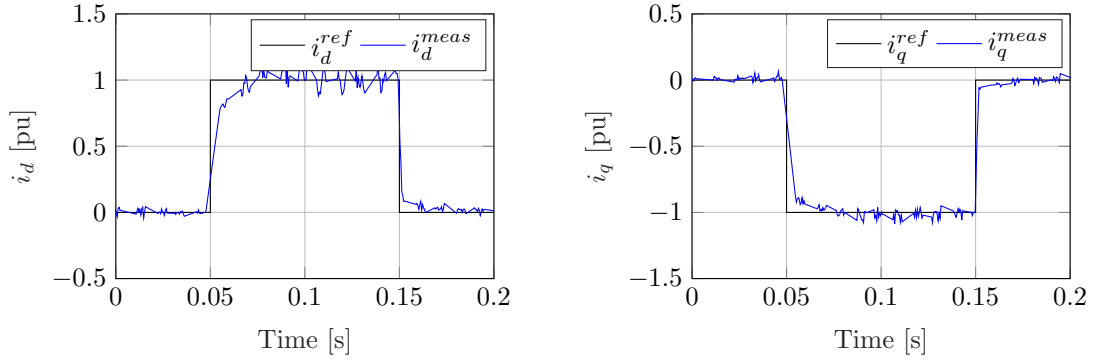

(b) Measured response reduced gains.

Figure 4.11: The measured current controller response for $i_f = 2.5$ A.

flux maps of the generator at different values of i_f, these maps are not practically verified. Despite the probable discrepancy, the current controllers prove to be robust, providing fast and stable responses.

4.3.2 MTPA map validation and response

Figure 4.12 shows the torque map for RSG operation i.e., for $i_f = 0$ A. The ARSM clearly goes into saturation earlier than the FEM model. This effect is more pronounced in motoring mode than it is for generator operation, as can be seen from the error map shown in Figure 4.12b. The error is less than ten percent for regions inside rated operation conditions, but increases to twenty percent for overrated conditions.

Any deviation in the torque data will cause an error in the LUTs used for the proposed MTPA control, especially in the current angle LUT. To ensure satisfactorily torque controller performance, the torque maps of the ARSG are measured. Measurements are only

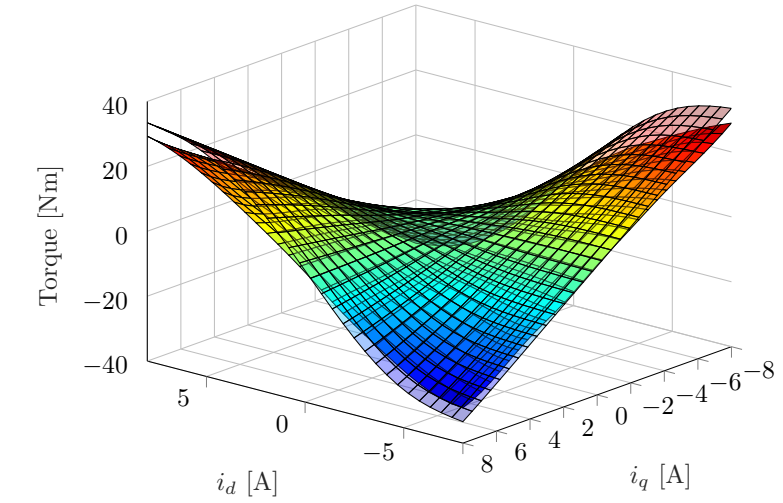

(a) Measured torque map together with the FE (transparent) torque map.

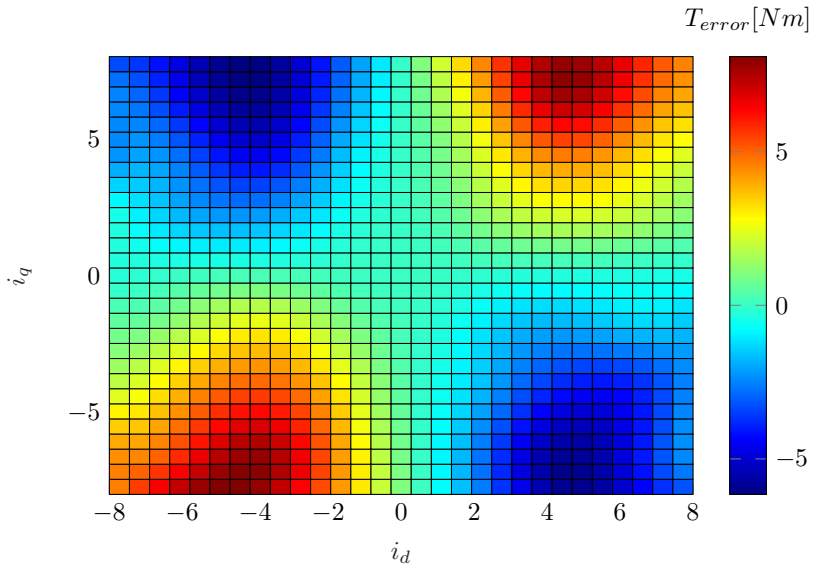

(b) Torque Error ($T_{FEM} - T_{meas}$)

Figure 4.12: Comparison between the measured and FE torque maps for $i_f = 0$ A i.e., for RSG operation.

taken for fourth quadrant operation and at field current intervals of 0.5A, up to 3A. These maps are not shown here, but the LUTs derived from the data are compared to the LUTs compiled using the FEM model data in Figures 4.13 and 4.14.

Figure 4.13b effectively demonstrates the effect that saturation has on the torque controller. The torque output error increases as i_s and i_f increase.

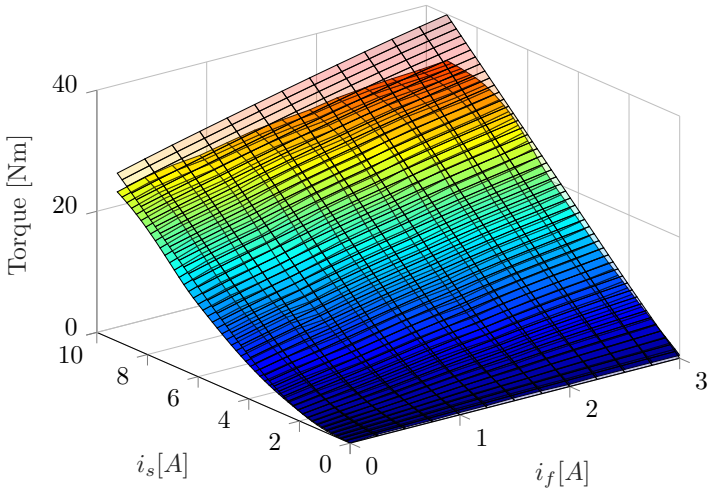

(a) Current torque LUT based on the FE simulation (transparent) and measured torque maps (solid).

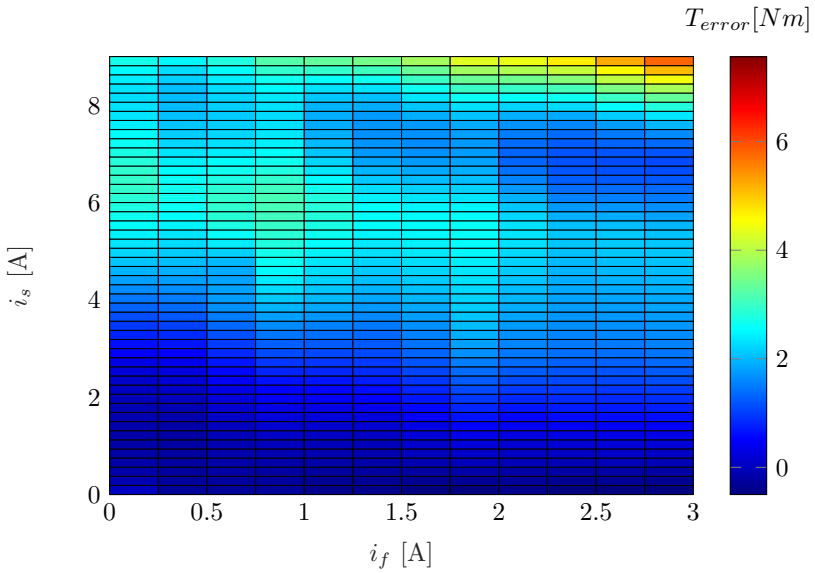

(b) The torque output error between the measured data based LUT and FEM data based LUT.

Figure 4.13: Comparison between the current LUTs generated by the FE and measured data.

Considering the comparison of the torque-angle LUTs in Figure 4.14, the discrepancy between the measured and calculated LUTs is very pronounced. The difference gets as big as 20°when operated above the rated torque of the ARSG. This pronounced effect can be caused by two diverse sources. The first factor is the saturation of the lamination material, as this will cause the optimum current angle to change. The second factor are the eddy current losses. As can be seen from the results discussed in Section 4.2.2, the effects of eddy currents can cause a shift in the optimum current angle. This shift is shown to be as big as 5°in some cases. The last factor, is regarding the data obtained from the FE model. For the generation of the control system LUTs, the FE model ignores the core and end winding leakage losses. When the errors that each of these factors contribute are combined, it can add up to the significant error seen between the two LUTs. As such, it was decided that the measured LUTs be used when doing the practical testing of the torque controller.

As is the case with simulated current controllers, the simulated torque controller shown in the top two results in Figure 4.15 shows an ideal response. As such, the simulated results for only $i_f = 0$ and 2.5 A are shown.

The torque tests shown in Figure 4.15 are done with an external DC voltage source, as is the case with the current controller tests in the previous section. The torque measurement shown here is derived from the frequency output of the torque sensor which tends to be very noisy. As such, the measured torque output is filtered. The torque response is shown for field current values of 0 and 2.5 A. The torque response is considered satisfactory, as the biggest error is five percent, with an average offset of three percent.

With the torque controller tests concluded, the control system has been shown to perform adequately for static field current values. To demonstrate the performance of the controllers under dynamic conditions, the rest of the results presented in this section are done with the field winding connected to the DC link of the two inverters.

One of the important facets in the simulation of the ARSG drive system in Simulink, is the use of an estimated DC-bus link current, calculated with Eq. (2.17). To verify this, a test is done where the torque is held constant, while step commands for the speed is given, which results in an increase in power and DC link current. The result shown in Figure 4.16 contains the estimate, the measured and low-pass filtered field current. The estimate is done using the measured torque and speed, with an efficiency estimate of 80 percent.

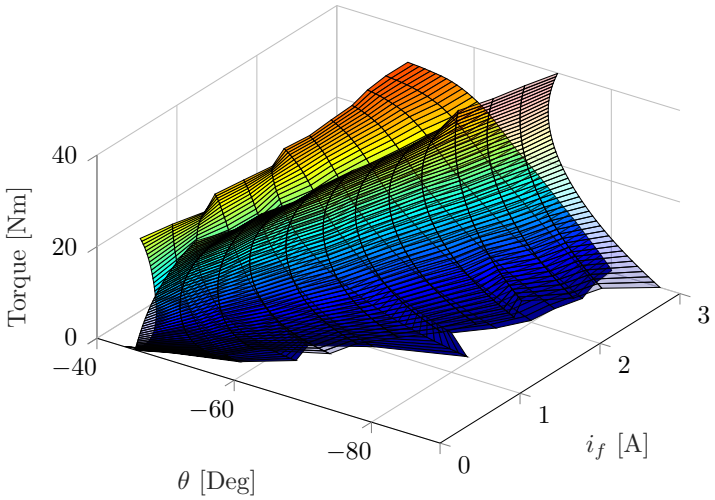

(a) Torque angle LUT based on the FEM simulation (transparent) and measured torque maps (solid).

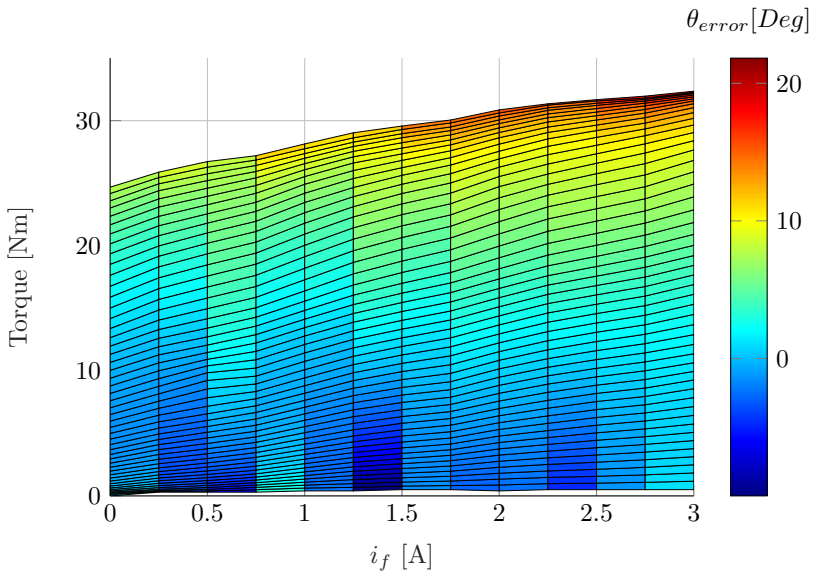

(b) The current angle output error between the two LUTs.

Figure 4.14: Comparison between the angle LUTs generated by the FE and measured data.

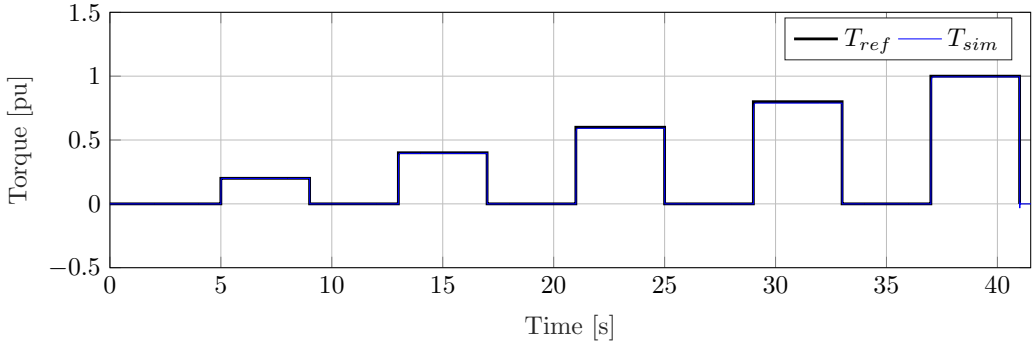

(a) Simulated response for $i_f = 0$A

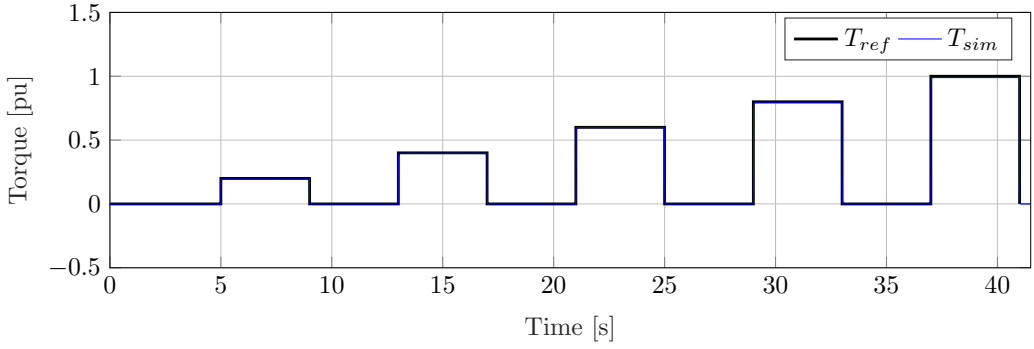

(b) Simulated response for $i_f = 2.5$ A.

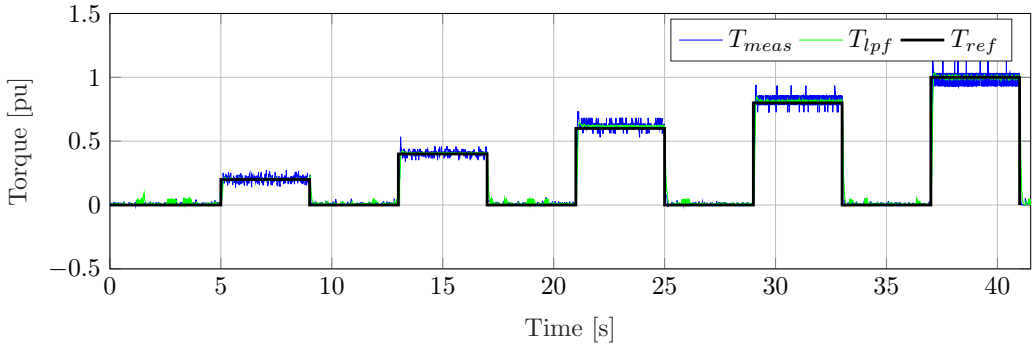

(c) Measured response for $i_f = 0$ A.

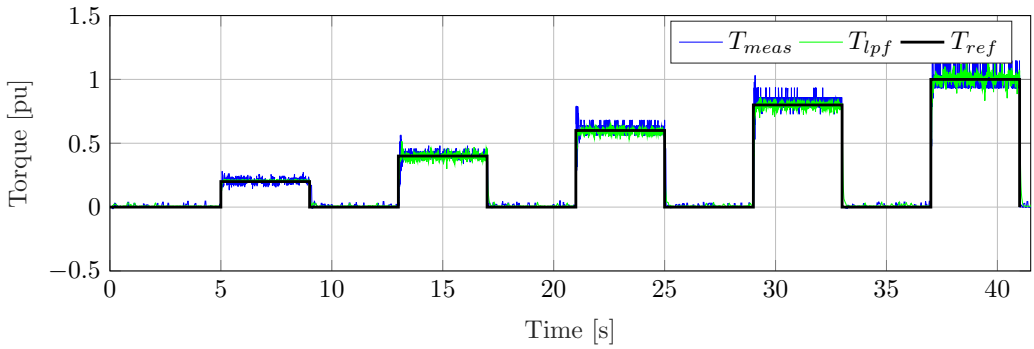

(d) Measured response for $i_f = 2.5$ A.

Figure 4.15: The simulated and measured torque controller response for field current values of 0 and 2.5 A at rated speed.

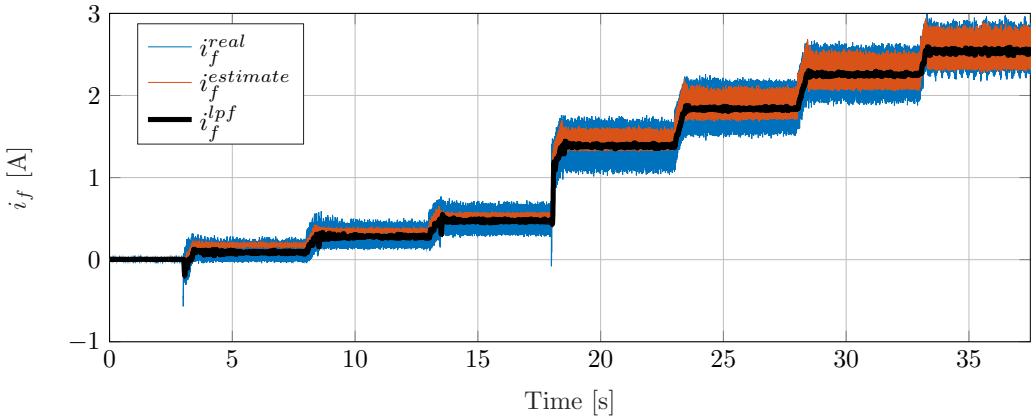

(a) Measured, low-pass filtered and estimated field current.

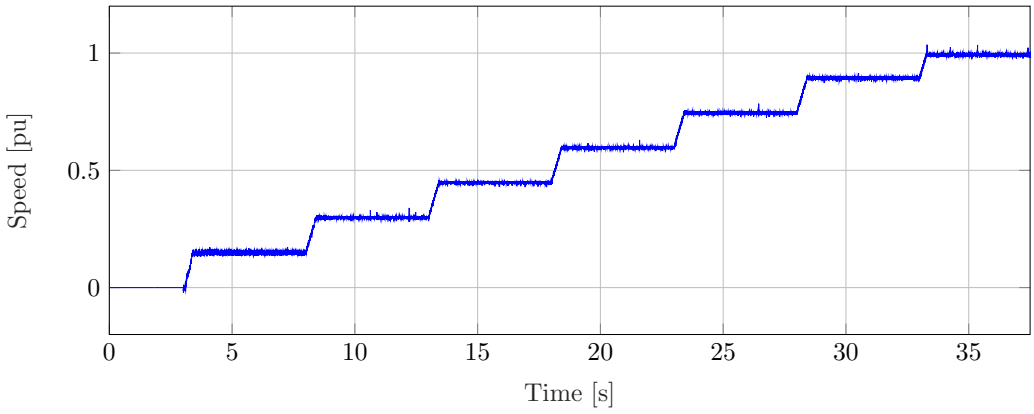

(b) The measured speed of the generator.

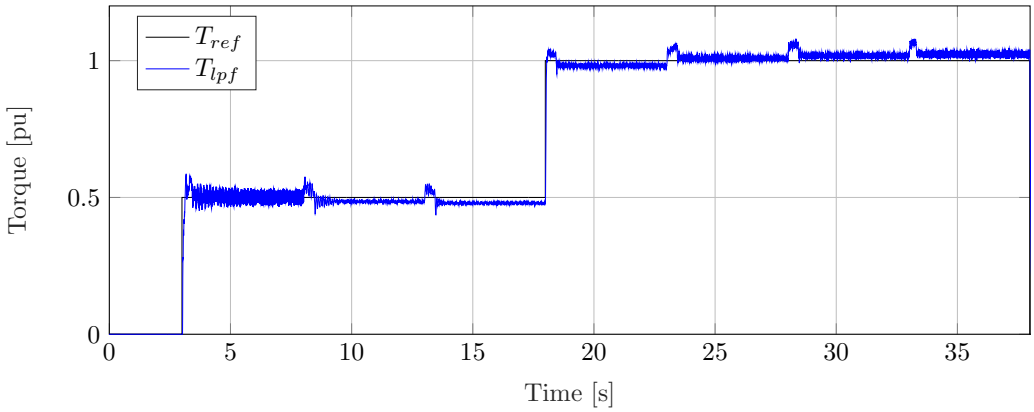

(c) The torque response for the above test.

Figure 4.16: Comparisons of the LUTs used for the MTPA algorithms.

4.3.3 Wind turbine control system

This section presents the simulated and measured results from the wind turbine control theory discussed in Section 3.2.3. Table 4.5 shows the specifications of the turbine used in these tests.

Table 4.5: Turbine specifications

	Value	Unit
V_o	8	m/s
n_t	250	RPM
P	1.6	kW
C_p^{opt}	0.48	[]

V_o - Mean wind speed; n_t - Turbine speed in revolutions per minute; P - Turbine power; C_p^{opt} - Turbine's performance coefficient.

Figure 4.17 shows the wind speed data that is generated by the wind speed subsystem. The simulated wind speed contains 60 000 data points and had to be down sampled for use in the practical tests. Figures 4.18 to 4.20 show the simulated wind turbine for a period of 500 s. The practically emulated wind turbine and turbine controller results for 550 s are presented in Figures 4.21 to 4.23. The practical measurements are taken on a WTS emulator using an induction machine as the prime mover. The simulation results show that the turbine's output power and C_p are precisely controlled using the TSR control method detailed in Section 3.2.3. It also clearly shows that the turbine acts as a sort of filter for the available power in the wind. Despite the less detailed wind speed data used on the practical system, the performance still mirrors that of the simulated turbine. These results also demonstrate the good dynamic performance of the current and torque controllers, with only a very slight offset in the torque controller output and none for the current tracking. Figure 4.22c does show that the emulator did struggle under dynamic power tracking conditions when compared with the simulated system. This can be attributed to the inability of the emulator to properly compensate for the damping that the IM and gearbox introduces to the system, which is not included in the simulations and would not be present in a real turbine system. Another reason for this could also be that the IM

torque is indirectly controlled through a volts-hertz speed controller. This is done because direct torque control on the IM could not be calibrated to provide consistent torque set points. It has been noted in [11] that torque control performance is greatly reduced when operating at a small fraction of the IM's rated torque. The two above mentioned factors combined with the known power tracking issues of a torque-controlled MPPT algorithm, resulted in the lower power tracking performance of the emulated system when compared with the simulated system.

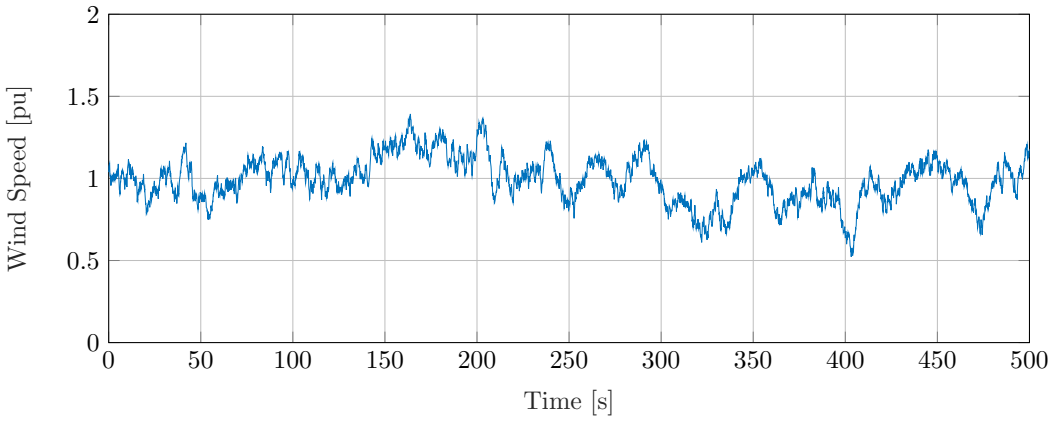

(a) Wind speed data used for the simulated turbine

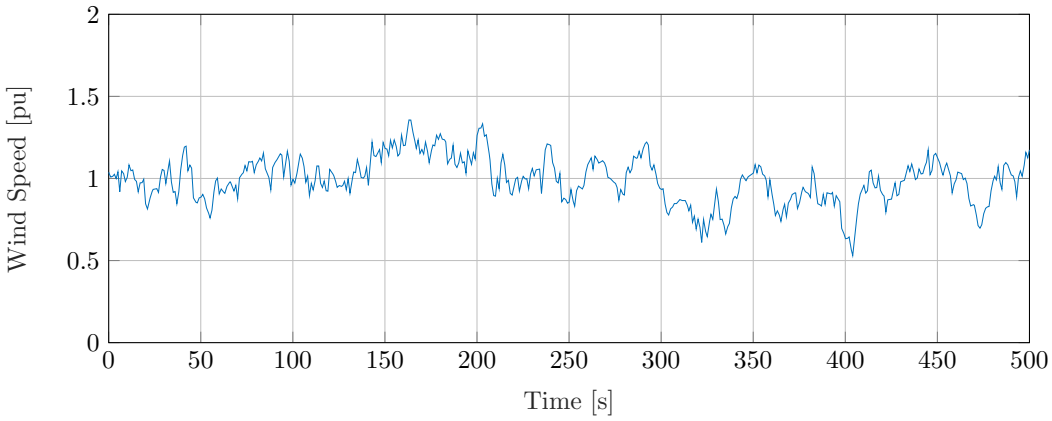

(b) Wind speed data used for the practically emulated turbine

Figure 4.17: A comparison of the wind speed data used for the simulation and practical tests of the controller.

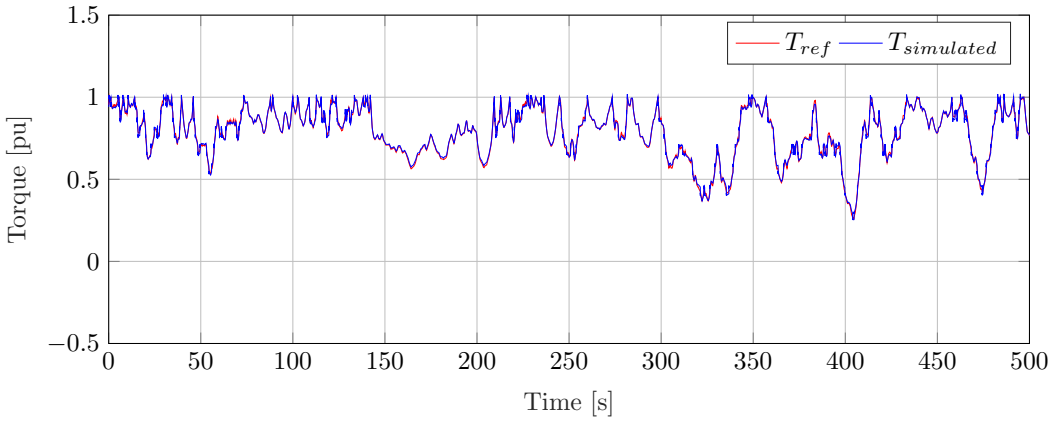

(a) Simulated torque response for the turbine controller.

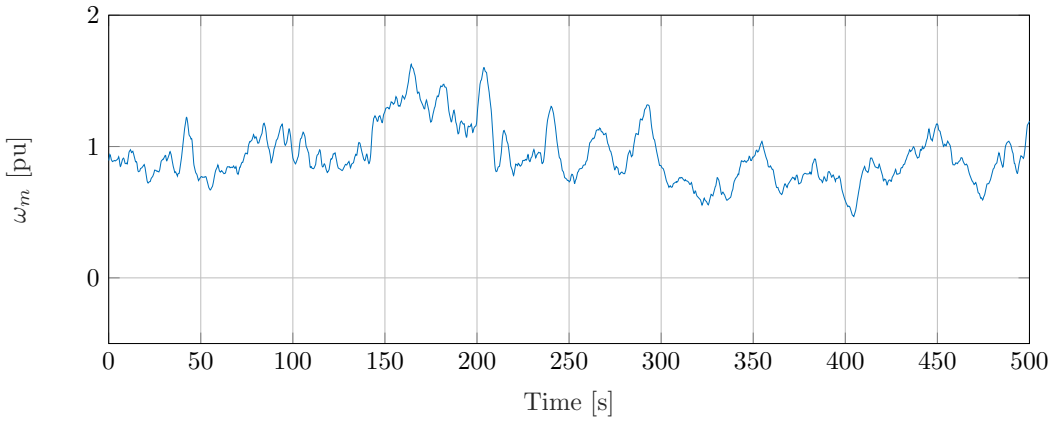

(b) The generator speed.

Figure 4.18: The generator speed and torque response for the turbine controller simulation.

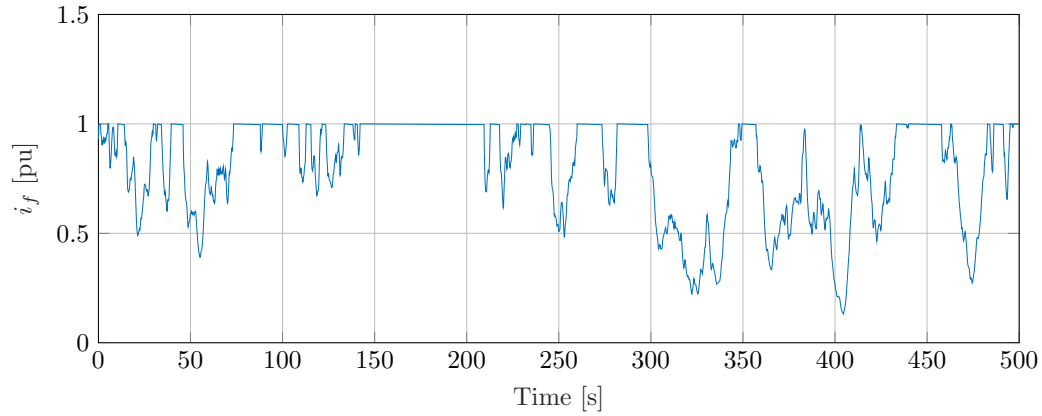

(a) The estimated DC-bus link current, using Eq. (2.17).

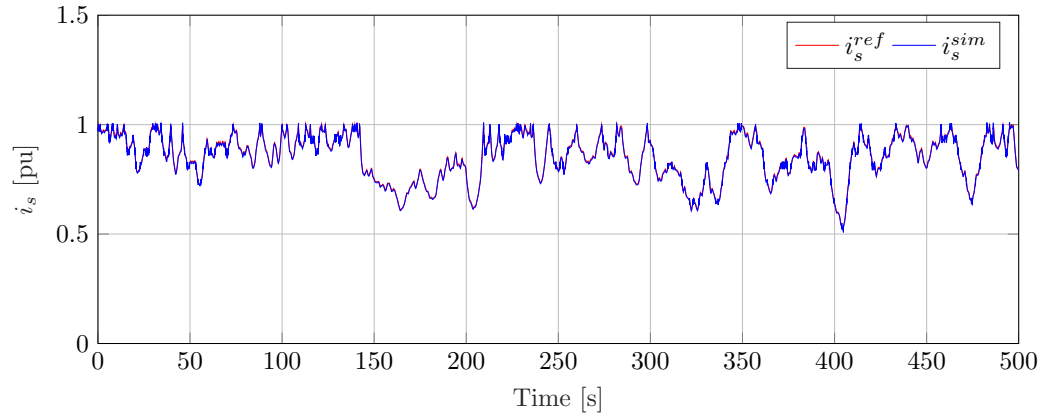

(b) The current controller response.

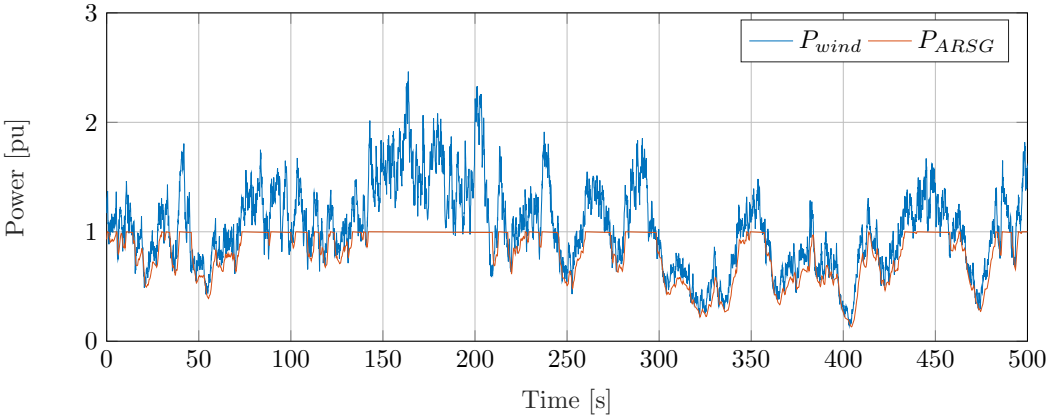

(c) The power available from the wind, as well as the power generated

Figure 4.19: Simulated I_f, I_s and power from the turbine emulation control.

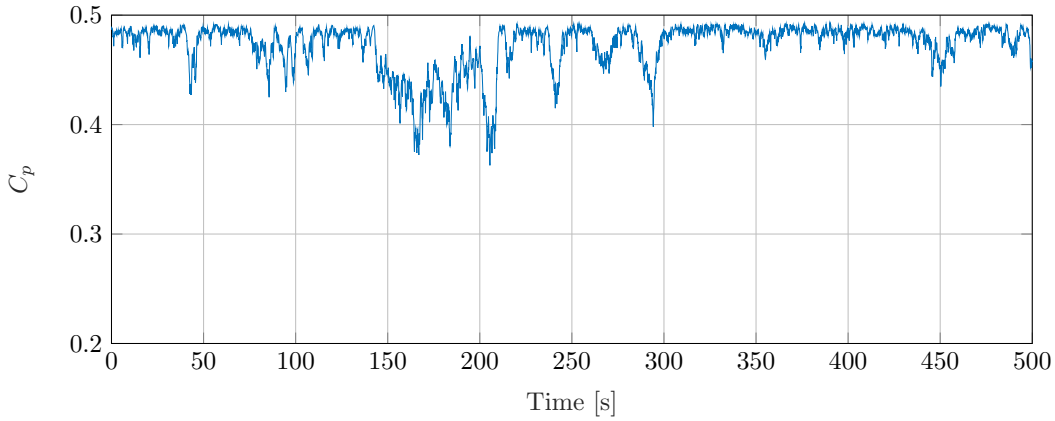

(a)

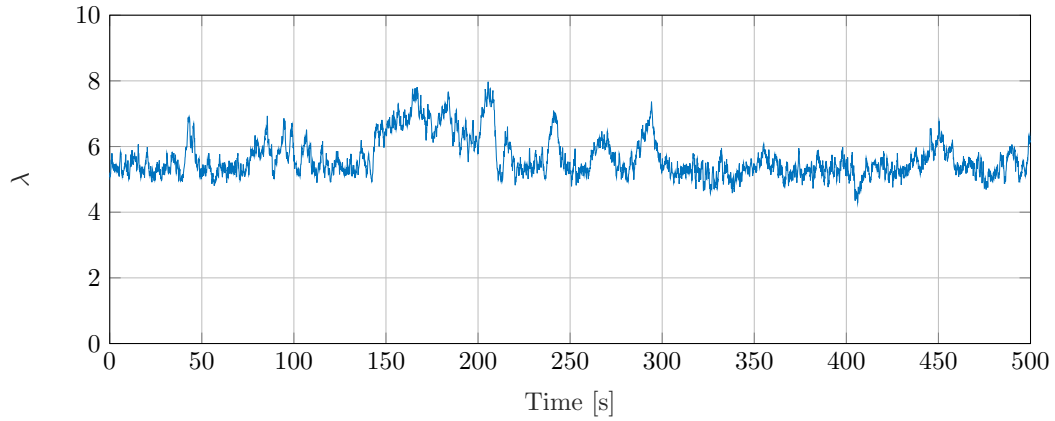

(b)

Figure 4.20: The simulated C_p and λ.

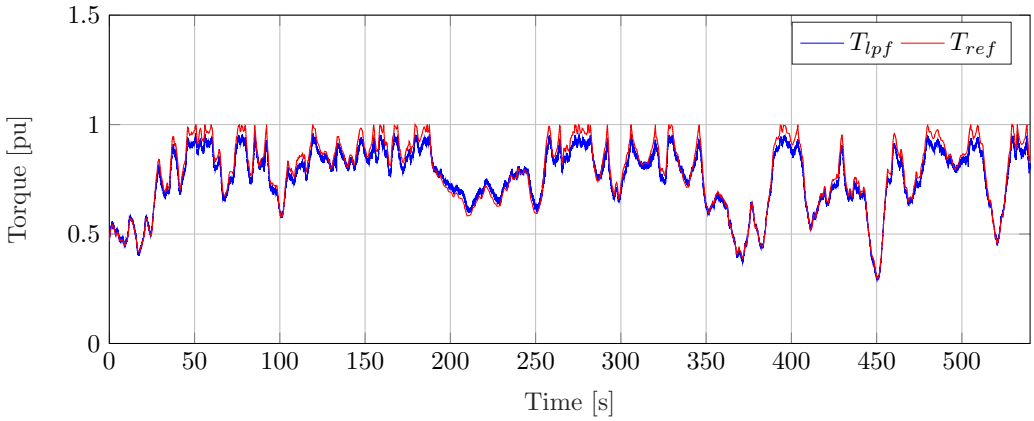

(a)

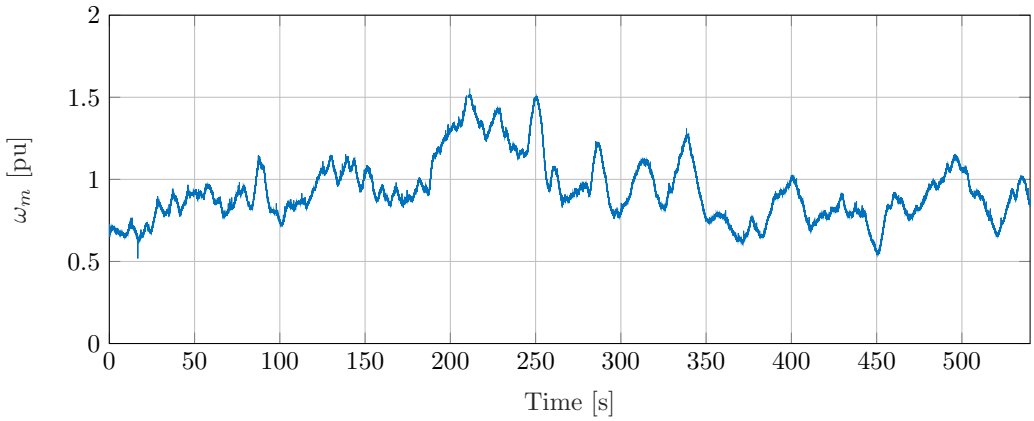

(b)

Figure 4.21: The measured torque and speed response.

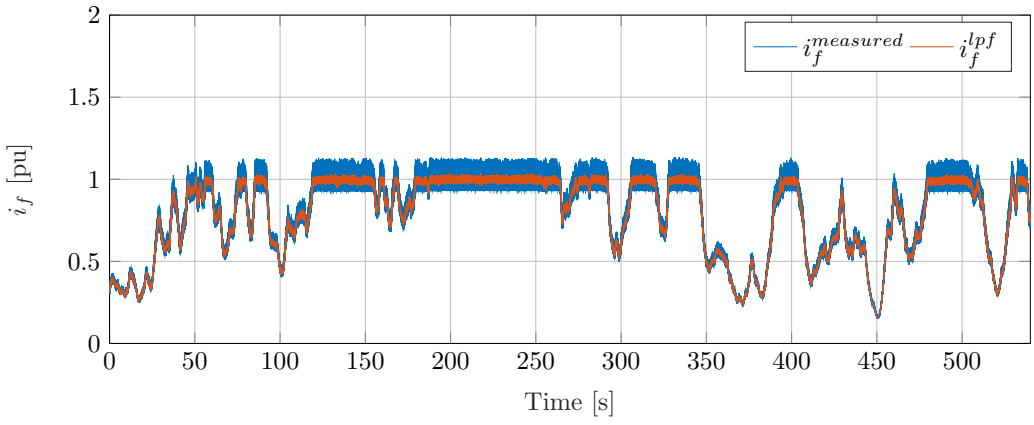

(a)

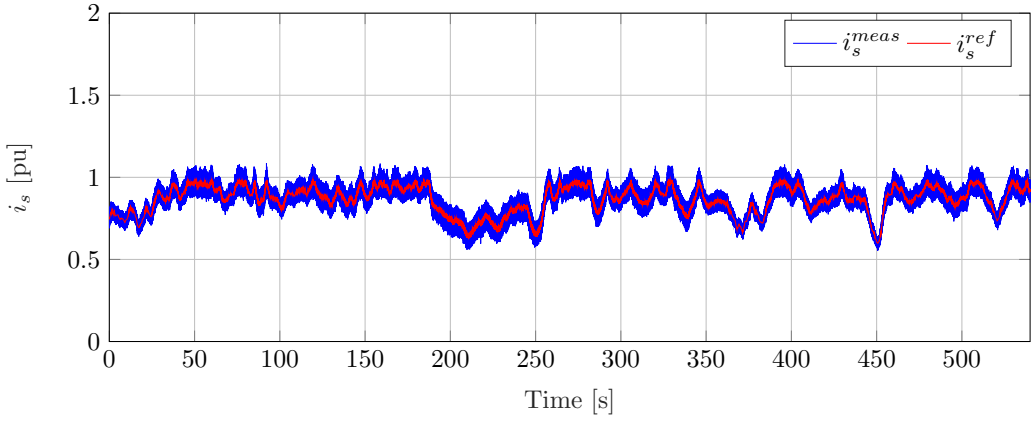

(b)

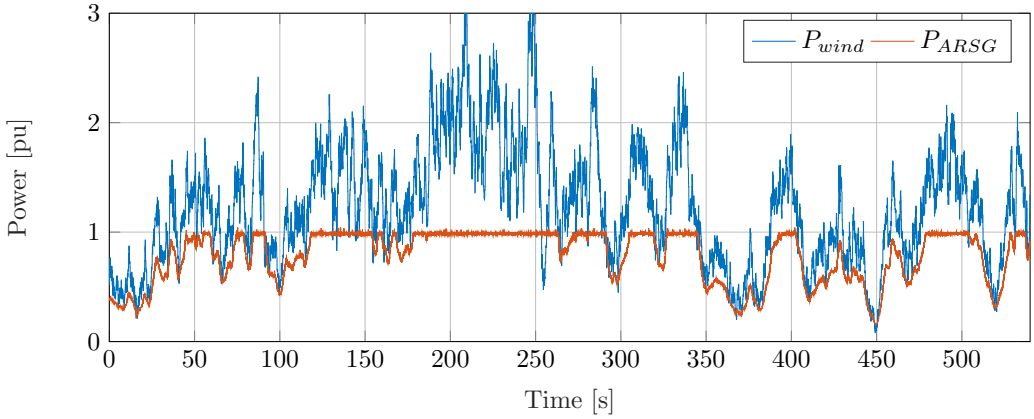

(c)

Figure 4.22: The measured I_f, I_s and power values.

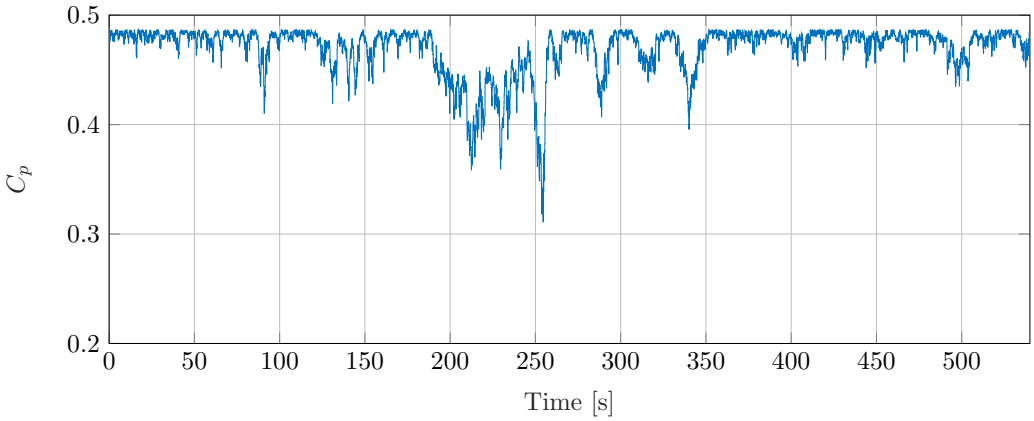

(a)

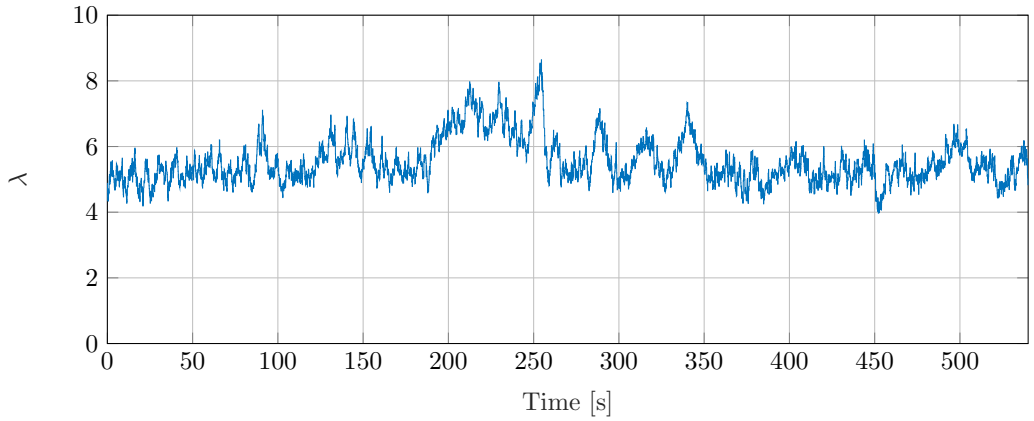

(b)

Figure 4.23: The measured C_p and λ.

Chapter 5

Conclusions and Recommendations

5.1 Conclusions

For this project, the control of a variable speed, fixed-pitch wind turbine using an assisted reluctance synchronous generator was investigated. A proof-of-concept 8-pole ARSG rotor was designed and built. A normal 8-pole IM stator was used, supplied by ACTOM. This elementary study provided some insights into the workings of the topology and its design. The rotor slot, for one, needs to be considered carefully to ensure optimum d-axis assistance. The effect of the field winding can be seen when looking at the increase in power factor. The torque and efficiency results have a favourable relation to the simulated values. Another positive from the results, is the very flat efficiency curves, as this has good implications for the control of the ARSG.

A non-linear current controller was designed, dependent on the flux linkage data generated by the FE simulations. The MO tuning method is used for this controller, which is shown to have satisfactory performance, even given inaccurate flux linkage data. The MO tuning method has shown overly aggressive gains, and for the best performance, the controller gains had to be reduced. Another tuning method might prove to be more suitable.

A torque controller based on LUTs was also designed, implemented and tested. The generator was tested using a separate DC current source, as well as the DC bus link. The torque maps of the generator were measured and compared to the simulated maps. This shows that there is little discrepancy between the two however, the effect of saturation led to a large difference in the current angle LUT, and as such the measured maps are used for

the LUTs. During testing, the largest offset during any torque command was five percent. This controller is only tested for generator mode, and the performance will be different for motoring mode.

The assumption made in the calculation of the rated field current in Eq. (2.17) was shown to be very accurate. This is due to the flat efficiency curves of the ARSG and a highly efficient VSC.

Lastly, a controller was designed for a small scale, variable speed, fixed-pitch turbine. The controller was designed in such a way that it functions without wind speed measurements and can transition seamlessly between the above and below rated wind speed regions. When operating in above rated conditions, the controller stalls the turbine by increasing the TSR. Stalling the turbine in such a way ensures that the generator is never overloaded, as the maximum current will be the rated current. The controller performed well in both simulated and practical tests.

5.2 Recommendations and future work

A number of aspects of this research lend itself to further work and improvements. Some of the work that can be done in the future are:

- The design and optimisation of the ARSG rotor. Work on the rotor slot could include the size and shape of the slot, as well as investigations into the optimum type of slot. This research should also consider the ease of winding, as this has a big effect on the manufacturing of the rotor. The current density used during the design should also be optimised for the specific slot, as this would have a big effect on the efficiency of the system. A stator should be designed and optimised along the rotor, to ensure that the generator performs optimally. Such a design would allow the optimisation of current densities in the stator and rotor. It is likely that such a design will lead to smaller and more competitive machines. Alongside this, a stator casing should be designed that can accommodate the slip rings. A proper analysis of the generator using 3D FE software would also provide more insight into the ARSG topology.

- A proper investigation into the effect that the field winding has on the rotor and stator core losses and eddy current losses should be done. This could also include the effect that the manufacturing of the rotor has.

- Other, more simple methods of current control should be investigated. While the LUT-based method works, the 3D LUTs take much time to generate for a more finely meshed FE machine model. The LUTs are also cumbersome to work with. Some more complex control structures, such as fuzzy or neural network control can be investigated. Alternatively, the use flux maps averaged over a range of field current values can be tested. Less aggressive tuning methods, such as the symmetrical optimum criterion, can be used to avoid the oscillations exhibited with the M.O. criterion.

- The use of 3D FE simulations, which could include the core losses and leakage inductances, can be used for the construction of the torque control LUTs. This would provide more accurate LUTs and would remove the need to measure the torque maps. For ease of use, the LUTs can be compiled into the dq-coordinates, rather than polar coordinates, off-line, thus removing the need to calculate the reference during operation. Some of the other methods of torque control, such as those based on virtual signal injection [59, 68], can also be investigated. Alternatively, torque control methods based on fuzzy control or neural networks can be considered.

- The potential for PSC of the machine should be investigated. As mentioned in [29], the field winding might make it easier to determine the position of the rotor, thus making PSC a lot easier than in a normal RSG.

- Throughout this project, the ARSG is connected to the DC-bus link without a switch. The implementation of an error detection algorithm and practical switch should be investigated.

- Additional work needs to be done on the wind turbine emulator. A properly sized IM and gearbox can be used, which would improve the power tracking performance. With the properly sized IM, direct torque control can also be implemented, which should also increase the performance of the emulated system.

- A comparison should be done between a optimised RSG, ARSG and PMSG to properly determine how competitive the ARSG is.

Appendices

Appendix A

Transformations and Miscellaneous Parameter Calculations

A.1 Reference frame transformations

Throughout this thesis the $dq0$ - reference frame is used as a way to simplify the design, analysis and control of the ARSM. This reference frame simplifies the three phase equations of the machine into equations that use DC signals, which allow for simple PI controllers to be designed. The $dq0$-reference frame rotates synchronously with the rotor of the machine; hence it is also referred to as the rotor fixed reference frame. Figure A.1 illustrates the $dq0$-reference frame on an ideal two pole machine.

As a definition, the d-axis of the machine is aligned with the phase a-axis when the mechanical angle θ_m ($\theta_e = \theta_m$*poles/2) is zero. The q-axis is then defined to be 90°in front of the d-axis. The transformation from abc quantities to the equivalent $dq0$ values is defined as given in [72]

$$s_{dq0} = T_r s_{abc} \tag{A.1}$$

$$\begin{bmatrix} s_d \\ s_q \\ s_0 \end{bmatrix} = \frac{3}{2} \begin{bmatrix} \cos(\theta_e) & \cos(\theta_e - \frac{2\pi}{3}) & \cos(\theta_e + \frac{2\pi}{3}) \\ -\sin(\theta_e) & -\sin(\theta_e - \frac{2\pi}{3}) & -sin(\theta_e + \frac{2\pi}{3}) \\ \frac{1}{2} & \frac{1}{2} & \frac{1}{2} \end{bmatrix} \begin{bmatrix} s_a \\ s_b \\ s_c \end{bmatrix} \tag{A.2}$$

where s is the desired stator quantity to be transformed. For a balanced three phase system it holds true that $s_a + s_b + s_c = 0$, thus the 0-term of the $dq0$ axis falls away.

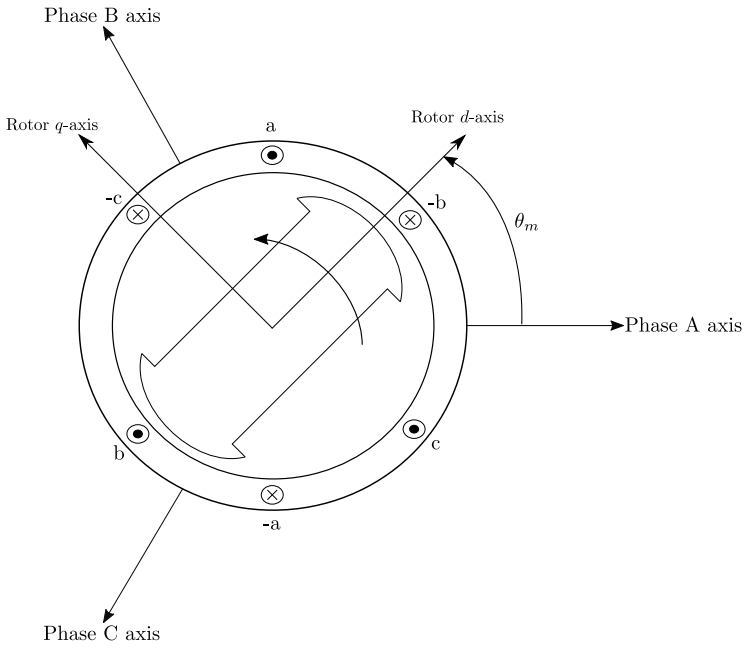

Figure A.1: Ideal two pole reluctance synchronous machine.

A.2 End winding leakage inductance

There are several methods which can be used to estimate the value of the end winding leakage inductance for a given machine. The method used in this thesis is the one given in [30]. The end winding leakage inductance is given, in henrys per phase, as

$$L_e = V_u N_{ph} d_i \Big(\frac{2W k_d k_{p(u)}}{p}\Big)^2 k_{e(p)} \times 10^{-8} \tag{A.3}$$

where,

N_{ph} = Number of phases

d_i = Stator inner diameter

W = Number of turns in series per phase

k_d = Standard distribution factor

p = Number of pole pairs

$V_{(u)}$ and $k_{p(u)}$ are dependent on the shape of the end winding, where the subscript u denotes the shape:

$u = 1$ for v-shaped end windings

$u = 2$ for elliptically shaped end windings

$u = 3$ for rectangular shaped end windings

$V_{(u)}$ is a shape factor, with the values given as:

$$V_{(1)} = 465, \tag{A.4}$$
$$V_{(2)} = 920, \tag{A.5}$$
$$V_{(3)} = 1040, \tag{A.6}$$

and $k_{p(u)}$ can be calculated by

$$k_{p(1)} = \frac{3\sin(\frac{\pi c_s}{6q})}{4 - (\frac{c_s}{3q})^2}, \tag{A.7}$$
$$k_{p(3)} = \sin(\frac{\pi c_s}{6q}), \tag{A.8}$$
$$k_{p(2)} \approx \frac{(k_{p(1)} + k_{p(3)})}{2}, \tag{A.9}$$

where c_s represents the number of slots being spanned by a coil and q is the number of slots per pole per phase. The factor $k_{e(p)}$ is an end winding factor for a certain pole p. The values given in [30] are:

$$k_{e(2)} = 0.51, \tag{A.10}$$
$$k_{e(4)} = 0.595, \tag{A.11}$$
$$k_{e(6)} = 0.64, \tag{A.12}$$
$$k_{e(8)} = 0.785. \tag{A.13}$$

Bibliography

[1] A. Tummala, R. K. Velamati, D. K. Sinha, V. Indraja, and V. H. Krishna, "A review on small scale wind turbines," *Renewable and Sustainable Energy Reviews*, vol. 56, pp. 1351–1371, 2016.

[2] Z. Alnasir and M. Kazerani, "An analytical literature review of stand-alone wind energy conversion systems from generator viewpoint," *Renewable and Sustainable Energy Reviews*, vol. 28, pp. 597–615, 2013.

[3] J. Pitteload and S. Gsanger, "2015 small wind world report," in *The 15th World Wind Energy Conference and Exhibition*, (Tokyo, Japan), 2016.

[4] J. Mitchell, M. Kamper, and C. Hackl, "Small-scale reluctance synchronous generator variable speed wind turbine system with dc transmission linked inverters," in *Energy Conversion Congress and Exposition (ECCE), 2016 IEEE*, pp. 1–8, IEEE, 2016.

[5] F. D. Bianchi, R. J. Mantz, and H. De Battista, *The wind and wind turbines*. Springer, 2007.

[6] G. M. Masters, *Renewable and efficient electric power systems*. John Wiley & Sons, 2013.

[7] J. P. du Plooy, *Development of a Converter-Fed Reluctance Synchronous Generator Wind Turbine Controller*. Masters, Stellenbosch University, 2015.

[8] J. Stegmann and M. Kamper, "Economic and efficiency evaluation of different battery charging wind generator systems," in *Southern African Universities Power Engineering Conference (SAUPEC), Johannesburg, South Africa*, Citeseer, 2010.

[9] M. M. Hossain and M. H. Ali, "Future research directions for the wind turbine generator system," *Renewable and Sustainable energy reviews*, vol. 49, pp. 481–489, 2015.

[10] Q. Wang and L. Chang, "An intelligent maximum power extraction algorithm for inverter-based variable speed wind turbine systems," *IEEE Transactions on power electronics*, vol. 19, no. 5, pp. 1242–1249, 2004.

[11] J. Mitchell, *The Control of Back-to-Back Power Converters for Small-Scale Reluctance Synchronous Generators in Grid-Connected Wind Turbine Systems*. Masters, Stellenbosch University, 2016.

[12] P. Ashwini and T. Archana, "Mathematical modeling of wind energy system using two mass model including generator losses," *International Journal of Emerging Trends in Electrical and Electronics*, 2016.

[13] I. P. Girsang, J. S. Dhupia, E. Muljadi, M. Singh, and L. Y. Pao, "Gearbox and drivetrain models to study dynamic effects of modern wind turbines," *IEEE Transactions on Industry Applications*, vol. 50, no. 6, pp. 3777–3786, 2014.

[14] M. R. Islam, Y. Guo, and J. Zhu, "Power converters for wind turbines: Current and future development," *Materials and Processes for Energy: Communicating Current Research and Technological Developments*, pp. 559–571, 2013.

[15] F. Blaabjerg and K. Ma, "Future on power electronics for wind turbine systems," *IEEE Journal of Emerging and Selected Topics in Power Electronics*, vol. 1, no. 3, pp. 139–152, 2013.

[16] K.-T. Chau, W. Li, and C. H. Lee, "Challenges and opportunities of electric machines for renewable energy," *Progress In Electromagnetics Research B*, vol. 42, pp. 45–74, 2012.

[17] D. Kadam and B. Kushare, "Overview of different wind generator systems and their comparisons," *International Journal of Engineering Science & Advanced Technology,[IJESAT]*, vol. 2, no. 4, pp. 1076–1081, 2012.

[18] J. Kostko, "Polyphase reaction synchronous motors," *Journal of the American Institute of Electrical Engineers*, vol. 42, no. 11, pp. 1162–1168, 1923.

[19] A. Cruickshank, R. Menzies, and A. Anderson, "Axially laminated anisotropic rotors for reluctance motors," in *Proceedings of the Institution of Electrical Engineers*, vol. 113, pp. 2058–2060, IET, 1966.

[20] P. C. Krause and T. A. ASipo, "Analysis and simplified representations of rectifier-inverter reluctance-synchronous motor drives," *IEEE Transactions on Power Apparatus and Systems*, no. 6, pp. 962–970, 1969.

[21] V. B. Honsinger, "The inductances ld and lq of reluctance machines," *IEEE Transactions on Power Apparatus and Systems*, no. 1, pp. 298–304, 1971.

[22] J. Barta and C. Ondrusek, "Rotor design and optimization of synchronous reluctance machine," *MM Science Journal*, 2015.

[23] M. Palmieri, M. Perta, F. Cupertino, and G. Pellegrino, "Effect of the numbers of slots and barriers on the optimal design of synchronous reluctance machines," in *Optimization of Electrical and Electronic Equipment (OPTIM), 2014 International Conference on*, pp. 260–267, IEEE, 2014.

[24] M. Nagrial, J. Rizk, and A. Hellany, "Analysis and performance of high efficiency synchronous reluctance machines," *international journal of energy and environment*, vol. 2, no. 2, pp. 247–254, 2011.

[25] G. Štumberger, M. Hadžiselimović, B. Štumberger, D. Miljavec, D. Dolinar, and I. Zagradišnik, "Comparison of capabilities of reluctance synchronous motor and induction motor," *Journal of Magnetism and Magnetic Materials*, vol. 304, no. 2, pp. e835–e837, 2006.

[26] W. Villet, *Critical Evaluation and Application of Position Sensorless Control Techniques for Reluctance Synchronous Machines*. Phd thesis, Stellenbosch University, 2013.

[27] M. Kamper and A. Volsdhenk, "Effect of rotor dimensions and cross magnetisation on ld and lq inductances of reluctance synchronous machine with cageless flux barrier rotor," *IEE Proceedings-Electric Power Applications*, vol. 141, no. 4, pp. 213–220, 1994.

[28] A. Vagati, "The synchronous reluctance solution: a new alternative in ac drives," in *Industrial Electronics, Control and Instrumentation, 1994. IECON'94., 20th International Conference on*, vol. 1, pp. 1–13, IEEE, 1994.

[29] M. J. Kamper and W. T. Villet, "Design and performance of compensated reluctance synchronous machine drive with extended constant power speed range," in *Energy Conversion Congress and Exposition (ECCE), 2012 IEEE*, pp. 4330–4337, IEEE, 2012.

[30] M. Kamper, *Design Optimisation of Cageless Flux Barrier Reluctance Synchronous Machine*. Phd thesis, Stellenbosch University, 1996.

[31] E. Howard and M. J. Kamper, "Weighted factor multi-objective design optimisation of a reluctance synchronous machine," in *Electric Machines & Drives Conference (IEMDC), 2015 IEEE International*, pp. 1781–1789, IEEE, 2015.

[32] F. J. W. Barnard, *Position Sensorless Control of a Transverse-Laminated Reluctance Synchronous Machine*. Masters, Stellenbosch University, 2014.

[33] H. W. de Kock, *Position Sensorless and optimal torque Control of Reluctance and Permanent Magnet Synchronous Machines*. Phd thesis, Stellenbosch University, 2009.

[34] C. M. Hackl, M. J. Kamper, J. Kullick, and J. Mitchell, "Current control of reluctance synchronous machines with online adjustment of the controller parameters," in *Industrial Electronics (ISIE), 2016 IEEE 25th International Symposium on*, pp. 153–160, IEEE, 2016.

[35] W. T. Villet and M. J. Kamper, "Position sensorless control of a reluctance synchronous wind generator drive with an lc inverter filter," *Electric Power Components and Systems*, vol. 43, no. 8-10, pp. 1051–1061, 2015.

[36] H. W. de Kock, *Dynamic Control of the Permanent Magnet Assisted Reluctance Synchronous Machine with Constant Current Angle*. Masters, Stellenbosch University, 2006.

[37] P. Zhang, D. M. Ionel, and N. A. Demerdash, "Saliency ratio and power factor of ipm motors optimally designed for high efficiency and low cost objectives," in *Energy Conversion Congress and Exposition (ECCE), 2014 IEEE*, pp. 3541–3547, IEEE, 2014.

[38] I. Boldea, L. Tutelea, and C. I. Pitic, "Pm-assisted reluctance synchronous motor/generator (pm-rsm) for mild hybrid vehicles: electromagnetic design," *IEEE Transactions on Industry Applications*, vol. 40, no. 2, pp. 492–498, 2004.

[39] M. J. Kamper, F. Van der Merwe, and S. Williamson, "Direct finite element design optimisation of the cageless reluctance synchronous machine," *IEEE Transactions on Energy Conversion*, vol. 11, no. 3, pp. 547–555, 1996.

[40] S. Kulkarni and A. Thosar, "Mathematical modeling and simulation of permanent magnet synchronous machine," *International Journal of Electronics and Electrical Engineering*, vol. 1, no. 2, pp. 66–71, 2013.

[41] A. T. Loubser and M. J. Kamper, "Design optimisation of reluctance synchronous machine for drive system efficiency," in *Electrical Machines Design, Control and Diagnosis (WEMDCD), 2015 IEEE Workshop on*, pp. 60–65, IEEE, 2015.

[42] I. C. Proimadis, D. V. Spyropoulos, and E. D. Mitronikas, "An alternative for all-electric ships applications: the synchronous reluctance motor," *Advances in Power Electronics*, vol. 2013, 2013.

[43] T. Lange, B. Kerdsup, C. Weiss, and R. W. De Doncker, "Torque ripple reduction in reluctance synchronous machines using an asymmetric rotor structure," in *Power Electronics, Machines and Drives (PEMD 2014), 7th IET International Conference on*, pp. 1–5, IET, 2014.

[44] D. Staton, T. Miller, and S. Wood, "Maximising the saliency ratio of the synchronous reluctance motor," in *IEE Proceedings B-Electric Power Applications*, vol. 140, pp. 249–259, IET, 1993.

[45] A. Vagati, G. Franceschini, I. Marongiu, and G. Troglia, "Design criteria of high performance synchronous reluctance motors," in *Industry Applications Society Annual Meeting, 1992., Conference Record of the 1992 IEEE*, pp. 66–73, IEEE, 1992.

[46] A. Vagati, M. Pastorelli, G. Francheschini, and S. C. Petrache, "Design of low-torque-ripple synchronous reluctance motors," *IEEE Transactions on Industry Applications*, vol. 34, no. 4, pp. 758–765, 1998.

[47] X. B. Bomela and M. J. Kamper, "Effect of stator chording and rotor skewing on performance of reluctance synchronous machine," *IEEE Transactions on Industry Applications*, vol. 38, no. 1, pp. 91–100, 2002.

[48] Y. Guan, Z. Zhu, I. Afinowi, J. Mipo, and P. Farah, "Design of synchronous reluctance and permanent magnet synchronous reluctance machines for electric vehicle application," *COMPEL: The International Journal for Computation and Mathematics in Electrical and Electronic Engineering*, vol. 35, no. 2, pp. 586–606, 2016.

[49] R. Karimagako, M. H. Nagrial, and J. Rizk, "Analysis and design of permanent magnet assisted synchronous reluctance machines," in *Power Electronics, Machines and Drives (PEMD 2010), 5th IET International Conference on*, pp. 1–6, IET, 2010.

[50] R. R. Moghaddam, F. Magnussen, and C. Sadarangani, "Theoretical and experimental reevaluation of synchronous reluctance machine," *IEEE Transactions on Industrial Electronics*, vol. 57, no. 1, pp. 6–13, 2010.

[51] P. J. J. Van Wyk, *Design and evaluation of medium speed geared direct grid connected wind generator drive train with specific focus on slip permanent magnet coupling*. Stellenbosch : Stellenbosch University, 2015.

[52] J. F. Gieras, R.-J. Wang, and M. J. Kamper, *Axial flux permanent magnet brushless machines*. Springer Science & Business Media, 2008.

[53] P. Fick, *Evaluation of the Constant Current Angle Controlled Reluctance Synchronous Machine Drive*. Masters, Stellenbosch University, 2002.

[54] T. M. Chikouche, A. Mezouar, T. Terras, and S. Hadjeri, "Variable gain pi controller design for speed control of a doubly fed induction motor," *Engineering, Technology & Applied Science Research*, vol. 3, no. 3, pp. 433–439, 2013.

[55] M. M. Bech, T. S. Frederiksen, and P. Sandholdt, "Accurate torque control of saturated interior permanent magnet synchronous motors in the field-weakening region," in *Industry Applications Conference, 2005. Fourtieth IAS Annual Meeting. Conference Record of the 2005*, vol. 4, pp. 2526–2532, IEEE, 2005.

[56] H. W. de Kock, A. J. Rix, and M. J. Kamper, "Optimal torque control of synchronous machines based on finite-element analysis," *IEEE Transactions on Industrial Electronics*, vol. 57, no. 1, pp. 413–419, 2010.

[57] C.-T. Pan and S.-M. Sue, "A linear maximum torque per ampere control for ipmsm drives over full-speed range," *IEEE Transactions on Energy Conversion*, vol. 20, no. 2, pp. 359–366, 2005.

[58] M. F. Rahman, L. Zhong, and K. W. Lim, "A direct torque controlled interior permanent magnet synchronous motor drive incorporating field weakening," in *Industry Applications Conference, 1997. thirty-second IAS Annual Meeting, IAS'97., Conference Record of the 1997 IEEE*, vol. 1, pp. 67–74, IEEE, 1997.

[59] T. Sun, J. Wang, and X. Chen, "Maximum torque per ampere (mtpa) control for interior permanent magnet synchronous machine drives based on virtual signal injection," *IEEE Transactions on Power Electronics*, vol. 30, no. 9, pp. 5036–5045, 2015.

[60] C. Balasundar, S. Sudharshanan, and R. Elakkiyavendan, "Design of an optimal tip speed ratio control mppt algorithm for standalone wecs," *International Journal for Research in Applied Science & Engineering Technology*, vol. 3, 2015.

[61] Q. Wang and L. Chang, "An intelligent maximum power extraction algorithm for inverter-based variable speed wind turbine systems," *IEEE Transactions on Power Electronics*, vol. 19, pp. 1242–1249, 2004.

[62] G. Moor and H. Beukes, "Maximum power point trackers for wind turbines," in *35th IEEE Annual Power Electronics Specialists Conference*, (Aachen, Germany), pp. 2044–2049, 2004.

[63] X. B. Y.D. Song, B. Dhinakaran, "Variable speed control of wind turbines using nonlinear and adaptive algorithms," *Journal of Wind Engineering and Industrial Aerodynamics*, vol. 85, pp. 293–308, 2000.

[64] S. M. R. Kazmi, H. Goto, H.-J. Guo, and O. Ichinokura, "Review and critical analysis of the research papers published till date on maximum power point tracking in wind energy conversion system," in *Energy Conversion Congress and Exposition (ECCE), 2010 IEEE*, pp. 4075–4082, IEEE, 2010.

[65] J. S. Thongam and M. Ouhrouche, "Mppt control methods in wind energy conversion systems," in *Fundamental and advanced topics in wind power*, InTech, 2011.

[66] S. M. Tripathi, A. N. Tiwari, and D. Singh, "Optimum design of proportional-integral controllers in grid-integrated pmsg-based wind energy conversion system," *International Transactions on Electrical Energy Systems*, vol. 26, no. 5, pp. 1006–1031, 2016.

[67] J. Cvejn, "Pi/pid controller design for fopdt plants based on the modulus optimum criterion," in *Carpathian Control Conference (ICCC), 2011 12th International*, pp. 60–65, IEEE, 2011.

[68] S. Calligaro, C. Olsen, R. Petrella, and N. Bedetti, "Automatic mtpa tracking in ipmsm drives: Loop dynamics, design and auto-tuning," in *Energy Conversion Congress and Exposition (ECCE), 2016 IEEE*, pp. 1–8, IEEE, 2016.

[69] S. Tokunaga and K. Kesamaru, "Fem simulation of novel small wind turbine generation system with synchronous reluctance generator," in *Electrical Machines and Systems (ICEMS), 2011 International Conference on*, pp. 1–6, IEEE, 2011.

[70] L. Yanjie and W. Jun, "A large time scale wind velocity simulation method," in *Computer Design and Applications (ICCDA), 2010 International Conference on*, vol. 4, pp. V4–282, IEEE, 2010.

[71] N. Stannard and J. Bumby, "Performance aspects of mains connected small-scale wind turbines," *IET generation, transmission & distribution*, vol. 1, no. 2, pp. 348–356, 2007.

[72] S. D. Umans, *Fitzgerald & Kingsley's Electric Machinery*. McGraw-Hill International, 2014.